Università degli Studi di Napoli Federico II

Dottorato di ricerca in Fisica
Ciclo XXXVI
Coordinatore: prof. Vincenzo Canale

Development of a new PMT readout and trigger system for the HEPD-02 calorimeter of the CSES-Limadou mission

Settore Scientifico Disciplinare: FIS/01

Dottorando
Marco Mese

Tutor
dr. Giuseppe Osteria
dr. Valentina Scotti

Anni 2020/2023

Abstract

This thesis describes the research activity I carried out as a PhD student, focused on the development and calibration of the PMT acquisition and trigger system for the High-Energy Particle Detector, which will be used onboard the second China Seismo-Electromagnetic Satellite for the CSES mission.

This mission arises from the collaboration between the Chinese Space Agency (CNSA) and the Italian Space Agency (ASI) and foresees the realization of a constellation of satellites which will monitor ionospheric parameters possibly related to earthquakes. The satellites will also monitor the solar activity and the interaction with the magnetosphere and will study the low-energy cosmic rays, extending data from PAMELA and AMS.

The CSES-02 satellite will be equipped with various instruments, among which the High Energy Particle Detector, a range calorimeter composed of plastic and inorganic scintillators coupled with PMTs, designed to measure the energy of charged particles in the range of 3 to 100 MeV for electrons, 30 to 200 MeV for protons and up to 200 MeV/amu for light nuclei.

Signals from the PMTs are acquired and digitized by an electronic board that also produces the trigger for the detector. This board represents an enhancement of the previous version used for HEPD-01, onboard the CSES-01 satellite. One of the improvements consists of the use of a new generation ASIC (CITIROC) for the amplification, shaping and memorization of signals from PMTs.

The new ASIC allows using the peak detection feature, optimizing the acquisition of signals with different temporal characteristics, such as those produced by plastic scintillators and LYSO.

Furthermore, new algorithms for trigger generation have been developed, providing the possibility to use trigger pre-scaling and concurrent trigger masks and allowing the detection of Gamma Ray Bursts.

By changing both the chosen concurrent triggers and the prescaling factors in different orbit zones, it is possible to control the bandwidth occupation between different physics channels and the acquisition of data in regions of the orbit, such as the poles and the South Atlantic Anomaly, where the particle rate significantly increases, especially for low energies, and can reach tens of megahertz.

The electronics of HEPD-02 were designed to work in a space environment and present various measures to cope with such a hostile environment. After the integration of the detector, different campaigns for space qualification have been conducted before shipping

to China.

This thesis is divided into five chapters:

- Chapter 1 describes the CSES-Limadou mission and gives some details on the physics of the seismo-ionospheric coupling. Some of the results from the first satellite will be presented as well.
- Chapter 2 focuses on the HEPD-02 detector and its subsystems.
- Chapter 3 gives a detailed description of the PMT acquisition and trigger system and the firmware specifically developed for it.
- Chapter 4 describes tests and measurements carried out to qualify and characterize the PMT acquisition and trigger system.
- Chapter 5 shows the qualification and acceptance tests made on the HEPD-02 detector.

Contents

1
The CSES-Limadou mission

The CSES (China Seismo-Electromagnetic Satellite) mission arises from the collaboration between the China National Space Administration (CNSA) and the Italian Space Agency (ASI) with the contribution of Italian universities and research centres.

The program is dedicated to the study of the coupling between seismic events and ionospheric disturbances that may affect the flux of particles precipitating from Van Allen belts, the components of the electric and magnetic field of the Earth, the plasma frequency and the composition of the ionosphere. A constellation of satellites, equipped with various detectors, will be realized for this purpose. The first satellite (CSES-01) was launched on 2nd of February 2018 and it's still operative.

Some of the first results from CSES-01 include the detection of the G3 geomagnetic storm of 26th of August 2018 and the observations of the Bayan earthquake on the 5th of August 2018. Data collected also have been used for the retrospective analysis of high-magnitude seismic events, such as the Palu earthquake on 28th of September 2018 ($M_W = 7.5$) and the Papua New Guinea earthquake on 14th of May 2019 ($M_W = 7.6$). These analyses found several ionospheric anomalies that could be related to the preparation phase of these seisms [1].

The second satellite (CSES-02) will be launched in 2024 and will be placed on an orbit with a phase shift of 180° with respect to CSES-01 to increase temporal resolution. While CSES-01 is operative only for latitude between ±65° and outside the South Atlantic Anomaly (SAA), the CSES-02 will operate also in polar regions and the SAA. All the instruments, with which the satellite will be equipped, are described in section 1.3.

The Italian collaboration developed the High-Energy Particle Detector (HEPD-02) and the Electric Field Detector (EFD-02). The HEPD-02 will measure the flux of particles and their energies, while the EFD-02 will measure the components of the electric field of the Earth.

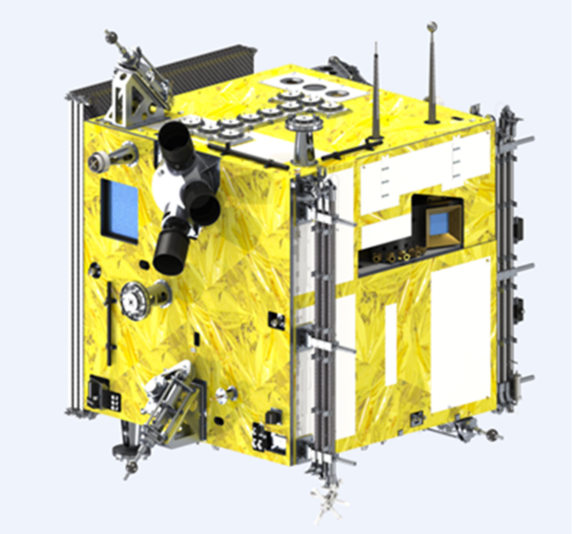

Figure 1.1: Rendering of the CSES-02 satellite [1]

1.1 Theoretical foundations

The coupling between seismic events and the perturbations that affect the ionosphere and the magnetosphere is a topic still under study but supported by experimental data from various experiments. The DEMETER mission was the first specifically devoted to exploring the electromagnetic disturbances correlated to earthquakes [2].

Various models have been developed to understand the underlying mechanisms involved in these phenomena and can be divided into co-seismic models and pre-seismic models. Co-seismic models are based on the ionospheric plasma perturbations caused by Acoustic Gravity Waves produced during an earthquake. Pre-seismic models are intended to search correlations with disturbances that happen *before* the occurrence of the seismic event and take into account the emission of Radon gas from microfractures that originate hours before the earthquake.

In the next sections, a brief description of the Earth's ionosphere and magnetosphere is given and then the most promising coupling models are shown.

1.1.1 Ionosphere

The ionosphere is the region of the atmosphere consisting of partially ionized gases that extend from about 50 to 1000 km above the Earth's surface, including the upper part of the stratosphere and the mesosphere. The ionized component of the gases, which constitutes plasma, is responsible for the reflection and consequent long-distance propagation of radio waves [3][4][5][6][7][8].

One of the most important parameters for studying the reflection of electromagnetic waves on ionospheric plasma is the plasma frequency, whose expression follows:

$$\nu_p = \frac{1}{2\pi}\sqrt{\frac{e^2}{m_e \varepsilon_0} n_e} \tag{1.1}$$

Where m_e is the rest mass of the electron and n_e is the electron density in the material under consideration (which in the case of plasma is the plasma density).

By substituting numerical values into this expression and measuring the frequency in Hertz, we obtain:

$$\nu_p = 8.98\sqrt{n_e} \quad \text{(Hz)} \tag{1.2}$$

An electromagnetic wave with a frequency lower than the plasma frequency will be reflected, while waves with higher frequencies can propagate inside the plasma. This means that the limiting frequency beyond which reflection is not possible depends on n_e. This, in turn, depends on the intensity of solar radiation that strikes the plasma.

Figure 1.2 shows the detailed profile of the plasma density. As can be seen, three regions can be distinguished:

- Region D ranging from 50 to 90 km
- Region E from 90 to 150 km
- Region F from 150 to 500 km

D region

This region is characterized by a plasma density that ranges from approximately 10 to $10^4\ \mathrm{cm}^{-3}$ and is the one with the least degree of ionization.

It is mainly composed of neutral gases, but also contains $O_2{}^+$ and NO^+ ions. The ionization is caused by X-rays, cosmic rays, and photons with wavelengths $\lambda = 1216$ Å (Lyman-α), which are not absorbed by the higher layers of the atmosphere.

Electromagnetic wave reflection only affects those with frequencies within 30 to 900 kHz (VLF to MF waves).

Despite this, the propagation of high frequencies in the range from 3 to 30 MHz is still influenced by this layer due to the incident wave's frequency being close to the electron-ion collision frequency (which in this region is in the order of 1 MHz) which cause strong absorption.

E region

The altitudes at which region E is defined correspond to those where the thermosphere begins. At these altitudes, there are mostly $O_2{}^+$ and NO^+ ions and these heights are characterized by increased plasma density and a sharp increase in temperature.

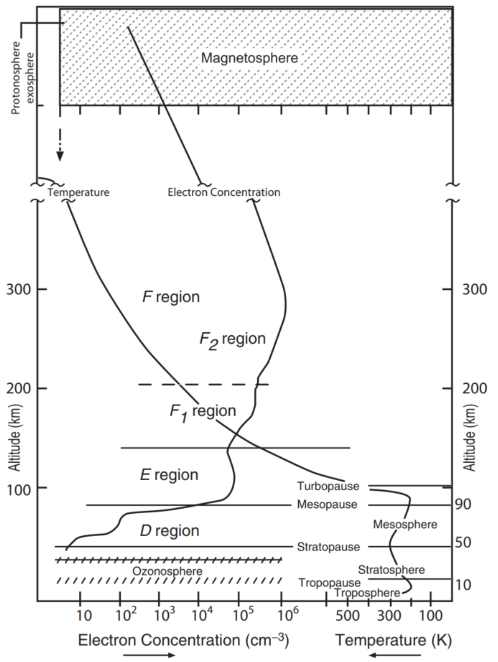

Figure 1.2: Ionospheric plasma density and temperature profile [4]

In particular, the plasma density is $n_p \simeq 10^5\ \mathrm{cm}^{-3}$, which results in a plasma frequency of approximately $\nu_{p_E} \simeq 2.8\ \mathrm{MHz}$.

In this region, plasma frequency is not the only limit for the reflection of incident electromagnetic waves. In fact, at these altitudes, the so-called sporadic E layer is formed, characterized by a higher plasma density and therefore allows the reflection of waves with frequencies up to 100 MHz.

F region

The F region can be further divided into two layers:

- F1 layer, which can only be observed during daylight hours and extends approximately from 150 to 200 km. Its chemical composition is characterized by a gradual decrease in $O_2{}^+$ and NO^+ ions and an increase in O^+ concentration. The plasma density varies from about $2 \cdot 10^5$ to $5 \cdot 10^5\ \mathrm{cm}^{-3}$

- F2 layer, which extends from 200 to 500 km. This is where the peak in plasma density occurs, and it links the plasma frequency of this region with the maximum frequency usable for communications via the reflection of electromagnetic waves on the ionosphere. The F2 layer is also the most important in the study of seismic precursors. One of the parameters that undergoes significant variations during the preparatory phases of an earthquake is the plasma frequency $\nu_{p_{F2}}$.

1.1.2 Magnetosphere

The Earth's magnetic field is generated by current established in the liquid part of the Earth's core due to convective motions. An approximate description of the mechanism that generates this field is given by the dynamo theory. Despite the complexity of the field that derives from this process, the components with order higher than the dipole term are negligible on the Earth's surface and it is therefore possible, as a first approximation, to consider a dipolar magnetic field [9].

Being the Earth immersed in the solar atmosphere, the magnetic field lines will deviate from those of a magnetic dipole. In fact, they are deformed not only by the solar magnetic field but also by the solar wind. The latter is a completely ionized plasma without collisions, consisting mainly of hydrogen ions, helium ions, and electrons, which, due to the high temperatures of the solar thermosphere, reach escape velocity and are expelled from the atmosphere of the Sun. Both high temperatures and radiation cause ionization.

The solar wind hits regions where the Earth's magnetic field is present and deforms its field lines. This deformation can be explained, as a first approximation, by considering only the interaction between the solar wind and the Earth's magnetic field.

As shown in 1.3a, solar wind particles directed towards the Earth undergo a deflection due to the Lorentz force: $F = Q\,\mathbf{v} \times \mathbf{B}$. Given the dependence on the charge of this force, positive particles (mainly hydrogen ions) and electrons will undergo opposite deflections and, since the abundance of positive particles is higher than electrons, the flux of cosmic rays coming from the west is higher than from the east (the so-called East-West effect).

The dipolar magnetic field follows a $1/r^3$ trend and most of the particles cannot approach below a certain distance from the Earth's surface. This led to the formation of a separation surface between the solar wind and the region of space, surrounding the Earth, in which the magnetic field has a sufficiently large module to deflect such particles.

The study of the shape of this surface and the analytical expression that follows is known as the Chapman-Ferraro problem. Given the complexity of the problem, this thesis will show the results in an exclusively qualitative manner.

On this surface, there is a current in the westward direction, called the Chapman-Ferraro current, which in turn produces a magnetic field. This field is antiparallel to the geomagnetic field in the zone facing the sun, while parallel in the opposite zone. This modifies the shape of the field lines and defines a surface (shown in 1.3b) called the magnetopause. The region inside the magnetopause, where the Earth's magnetic field is predominant, is called the magnetosphere.

Depending on their energy, some particles of the solar wind enter the magnetosphere and are trapped by the geomagnetic field, forming the Van Allen belts.

1.1.3 Van Allen Belts

The Van Allen belts are toroidal regions that surround the Earth, characterized by the presence of particles with energies ranging from hundreds of keV to hundreds of MeV. The particles contained in these regions are mainly protons and electrons that come from

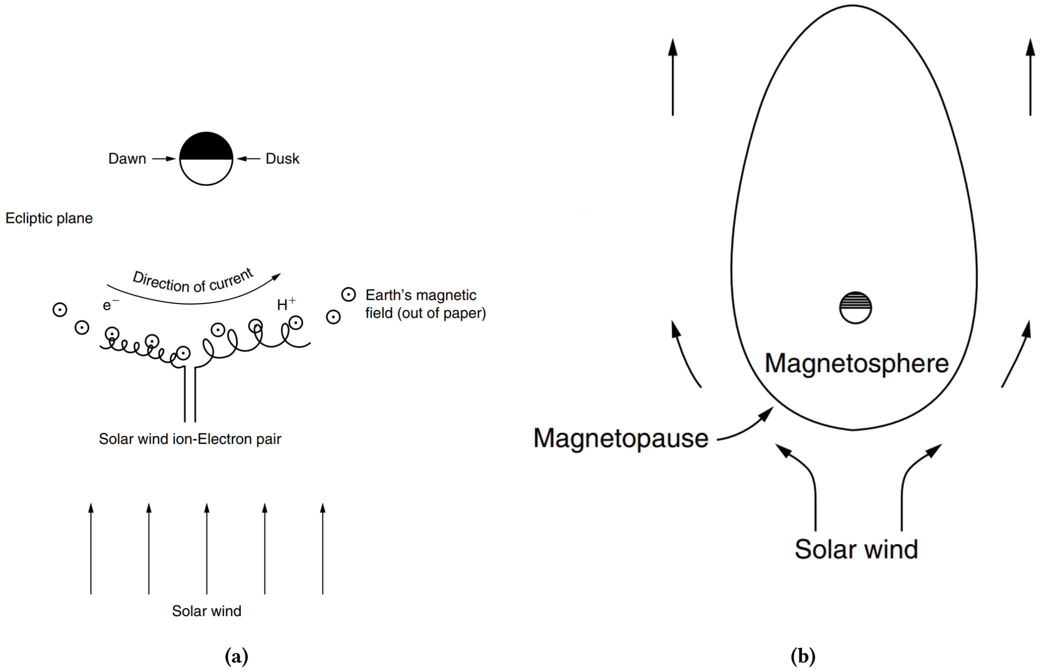

Figure 1.3: Description of the East-West effect: (a) and Earth's magnetosphere structure (b) [6]

the solar wind and cosmic rays and remain trapped in the geomagnetic field [10].

Two belts can be distinguished:

- An inner belt that extends between 1000 km and 6000 km of altitude and is mostly made up of highly energetic protons (with energies on the order of hundreds of MeV).
- An outer belt (between 10 000 km and 60 000 km) that is mainly composed of electrons with energies in the range of 0.1 to 10 MeV.

Figure 1.4a shows a representation of the two Van Allen belts while figure 1.4b shows the trajectory of a charged particle trapped in the Van Allen belts around the geomagnetic field lines. It is possible to see that the trajectory of the particles is determined by the following three motions:

- A helical motion around the magnetic field lines (indicated in the figure as **gyro motion**)
- A drift motion, dependent on the sign of the particle's charge (indicated in the figure as **drift motion**)
- An oscillatory motion between two points called mirror points (indicated in the figure as **bounce motion**)

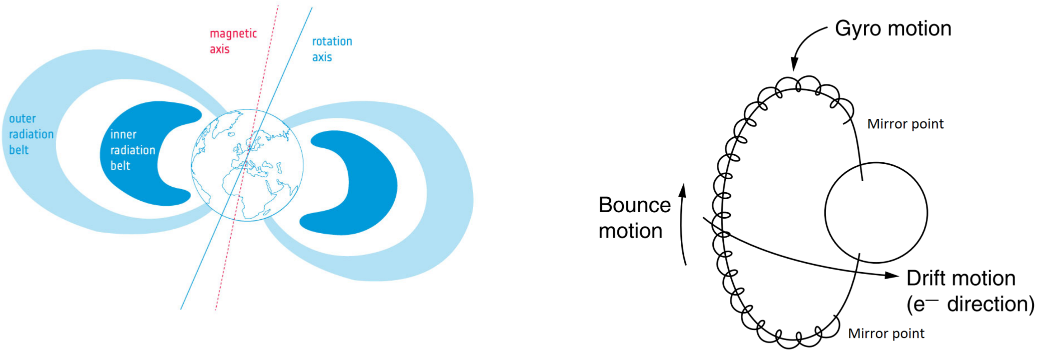

(a)

(b)

Figure 1.4: Description of Van Allen belts (a) and motion of trapped charged particles (b) [10]

The angle between the direction of the particle's velocity vector and the magnetic field line around which it moves is called 'pitch angle' (α).

Near the mirror points, this angle assumes a value of 90° and the particle retraces its path along the field line in the opposite direction until it reaches the other mirror point. In this way, the particles have no way of leaving these regions unless they undergo perturbations that cause a variation in the pitch angle. During the preparatory phases of an earthquake, electromagnetic waves are generated that can propagate to the Van Allen belts, varying the pitch angle and causing an increase in the flow of particles that precipitate towards the Earth's surface

The three motions that constitute the particle dynamics in the geomagnetic field are characterized by very different periods: the gyro motion period (τ_{gyro}) depends on the mass of particles and varies from 10^{-4} to 10^{-3} s for electrons and from 0.1 to 1 s for protons. The bounce motion period (τ_{bounce}) depends on the kinetic energy and for 1 keV electrons is $\sim$ 6 s while for protons is $\sim$ 10 minutes. The drift period (τ_{drift}) is in the order of hours. These wide temporal ranges allow us to obtain three adiabatic invariants from the action integral:

$$J = \oint d\mathbf{s} \cdot (\mathbf{p} + Q\mathbf{A}) \tag{1.3}$$

First adiabatic invariant

The integration of 1.3 over one gyration orbit gives the first adiabatic invariant. In this case the $d\mathbf{s}$ element is the infinitesimal path along the orbit and $\mathbf{p}_{\|} \cdot d\mathbf{s} = 0$, hence the integral becomes:

$$\begin{aligned} J &= \oint d\mathbf{s} \cdot (\mathbf{p} + Q\mathbf{A}) = \\ &= p_\perp 2\pi r + Q \oint_\Sigma d\sigma\, \hat{n} \cdot \nabla \times \mathbf{A} = \\ &= p_\perp 2\pi r + Q \oint_\Sigma d\sigma\, \hat{n} \cdot \mathbf{B} = \\ &= p_\perp 2\pi r - Q\pi r^2 B \end{aligned} \tag{1.4}$$

Where Stoke's theorem was applied to the second term and $p_\perp$ has been taken out from the integral since in a single gyration orbit B can be considered constant and uniform (being the bounce motion in different temporal scales). The negative sign of the magnetic flux comes from the fact that the surface defined by the particle motion has a normal opposite to **B**. Replacing 'r' with the gyroradius $r = \frac{p_\perp}{QB}$, the invariant can be written as:

$$J = \frac{\pi p_\perp^2}{QB} \tag{1.5}$$

Instead of using this expression, it is often used the magnetic moment since it differs from J only by constant factors:

$$\mu = \frac{p_\perp^2}{2mB} \tag{1.6}$$

This equation also means that $p_\perp^2/B = const$ and considering that $p_\perp = p\sin\alpha$, with α being the pitch angle, we get:

$$\frac{p^2 \sin^2\alpha}{B} = const \tag{1.7}$$

It is possible to observe that the perpendicular velocity of the particle must increase when it enters regions with a stronger magnetic field to maintain the magnetic moment constant. Since the particle is subject only to magnetic field, its kinetic energy is conserved and then also the linear moment 'p', therefore the increase in $p_\perp$ results in an increase of the pitch angle α (see figure 1.5).

When the pitch angle reaches 90°, the parallel moment vanishes ($p_{||} = p\cos\alpha$) and the particle is reflected, repeating the trajectory around the line field in the opposite direction.

From equation 1.7, it is possible to obtain a relation between the particle's parallel moment and the magnetic field:

$$\begin{aligned} &\frac{p^2 \sin^2\alpha}{B} = \frac{p^2 \sin^2 90^\circ}{B_m} \implies \\ &\implies \frac{B}{B_m} = \sin^2\alpha = 1 - \cos^2\alpha = 1 - \frac{p_{||}^2}{p^2} \implies \\ &\implies p_{||} = p\sqrt{1 - \frac{B}{B_m}} \end{aligned} \tag{1.8}$$

With B_m being the value of the magnetic field in the mirror points.

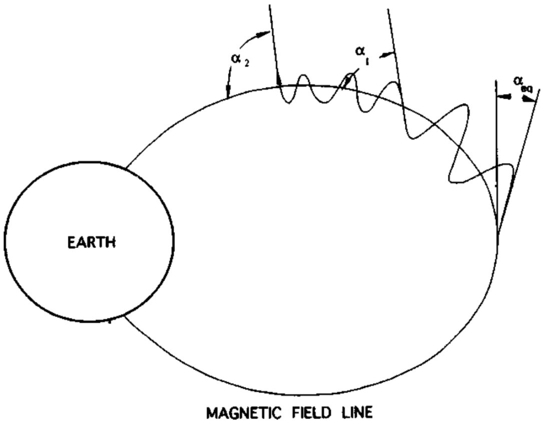

Figure 1.5: Increase of the pitch angle of particles entering regions with a stronger magnetic field [10]

Second adiabatic invariant

The integration of equation 1.3 over the bounce period and along the field lines, gives the second adiabatic invariant and equation 1.3 becomes:

$$J = \oint ds\, p_{\|} \tag{1.9}$$

Where the second term of 1.3 vanishes since the bounce path between the two mirror points encloses a null area and the magnetic flux is zero.

From equations 1.8 and 1.9, we obtain:

$$J = 2 \int_{s_m}^{s'_m} ds\, p \sqrt{1 - \frac{B(s)}{B_m}} \tag{1.10}$$

here s_m and s'_m are the positions along the field line of the two mirror points.

Instead of using 1.10 as the second invariant, it is better to use the quantity $I = J/2p$, which allows to write the invariant entirely in terms of the magnetic field:

$$I = \int_{s_m}^{s'_m} ds \sqrt{1 - \frac{B(s)}{B_m}} \tag{1.11}$$

This invariant ensures that, during the drift motion of the particle around the Earth, the particle will bounce along the same field lines, however distorted the field may be. After a period, will return to the same line from which it started (see figure 1.6).

Third adiabatic invariant

The third adiabatic invariant can be obtained by integrating 1.3 along the drift path.

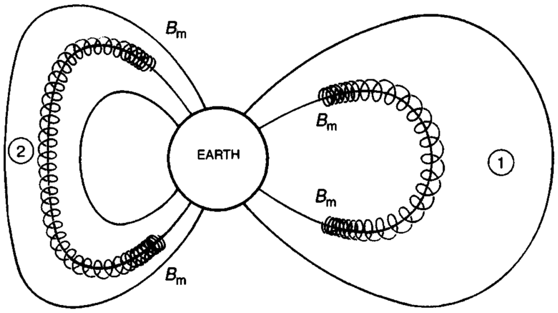

Figure 1.6: Drift path of a charged particle in the geomagnetic field: the conservation of the integral in equation 1.11, ensures that a particle on line 1 will drift to line 2 and after a period will return to 1 [10]

Considering that the average of **p** is very small along this path, the first term vanishes and the integral becomes:

$$J = Q \oint d\mathbf{s} \cdot \mathbf{A} = Q \oint_{\Sigma} d\sigma\, \hat{n} \cdot \nabla \times \mathbf{A} = Q \oint_{\Sigma} d\sigma\, \hat{n} \cdot \mathbf{B} = Q\phi(\mathbf{B}) \tag{1.12}$$

Where Stoke's theorem has been used, Σ is the surface enclosed by the drift path and $\phi(\mathbf{B})$ represents the flux of the magnetic field.

This invariant describes the variations in the drift paths when slow changes in the geomagnetic field occur: if **B** is compressed (for example by an increase of the solar wind strength), the drift path radius must decrease to keep the flux constant.

L-shell parameter

To study the dynamics of particles trapped in the Van Allen Belts, a coordinate system based on positions would be complicated due to the irregularity of the geomagnetic field.

A more suitable system is based on the adiabatic invariants and takes into account the value of the magnetic field B and a parameter called 'L-shell'. This is defined as the distance, in Earth's radii, from the centre of the Earth to the crossing point of the magnetic field and the equatorial plane.

Using the (B, L) coordinate system, the motion of a trapped particle can be uniquely determined, as well as the drift shell in which it moves with the vantage of B and L being directly measurable quantities.

1.1.4 MILC model

The MILC (Magnetosphere-Ionosphere-Lithosphere Coupling) is a mathematical co-seismic model that takes into account the Acoustic Gravity Waves (AGW) generated in the lower atmosphere by the ground motions that occur during an earthquake [11].

Figure 1.7 shows a schematic description of this mechanism:

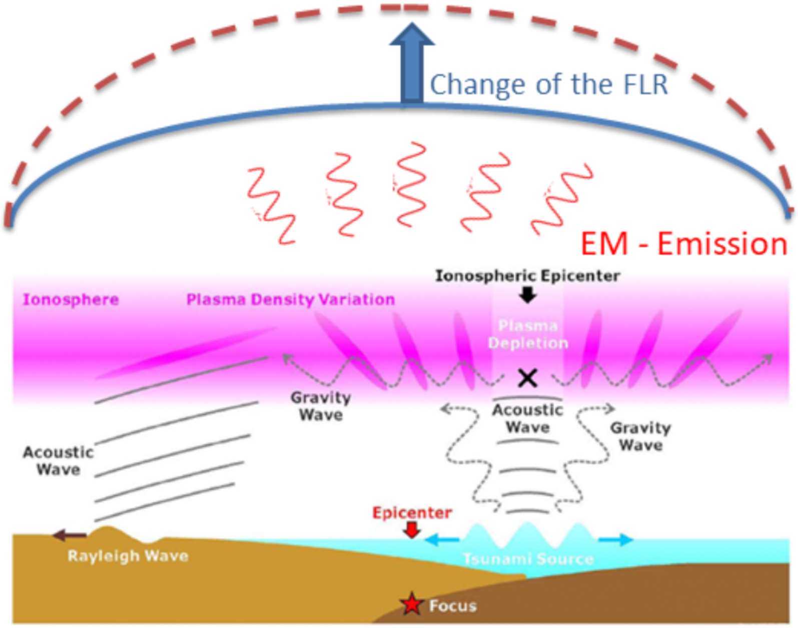

Figure 1.7: Description of the MILC model [11]

1. When an earthquake occurs, the ground motion produces acoustic gravity waves that propagate from the epicentre through the atmosphere and eventually reach the ionosphere
2. The disturbances in pressure and density of the ionosphere, caused by the AGW, give rise to displacement in the charges inside the ionospheric plasma and, subsequently, to electric currents that produce electromagnetic waves
3. These waves interact with the magnetosphere causing variations in the geomagnetic field line eigenfrequency

Thanks to the instruments onboard the CSES satellites, it is possible to measure the components of the electric and magnetic field to evaluate these disturbances and also the ionospheric plasma composition. Results from the CSES-01 satellite, related to some seismic events that occurred during its flight, will be presented in section 1.2.

1.1.5 LAIC model

The study of earthquake precursors is still an open topic and various models have been developed over the years. In this section, one of the first models is briefly presented without any claim to consider it conclusive.

The Lithosphere-Atmosphere-Ionosphere Coupling (LAIC) model takes into account the emanation of Radon gas from microfractures in the Earth's crust, which can originate hours or days before a seismic event [13][12][14][15].

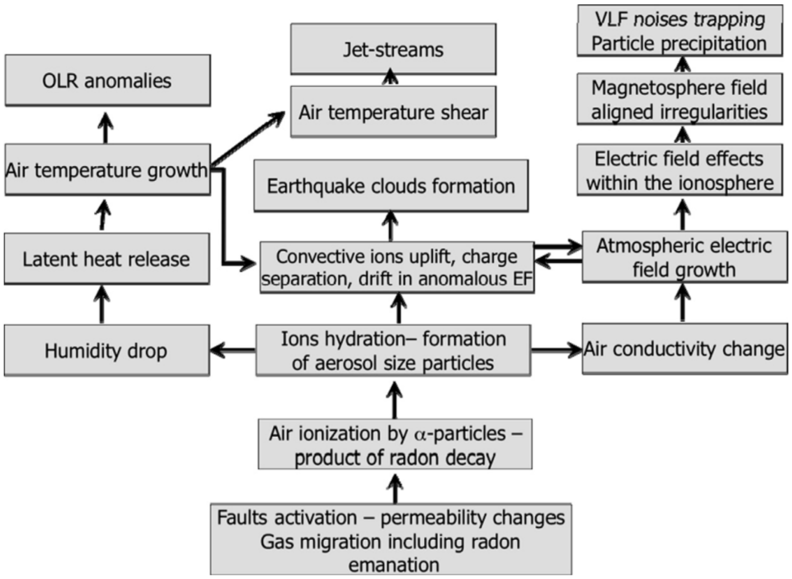

Figure 1.8: Schematic representation of the LAIC model [12]

Radon is highly radioactive ($30 \div 50\mathrm{Bq\,m^{-3}}$) and ionizes the lower layers of the atmosphere. Consequently, ion-molecule reactions occur on very short time scales (on the order of 10^{-7} s), leading to the production of the following chemical species: O^-, ${O_2}^-$, ${NO_2}^-$, ${NO_3}^-$, ${CO_3}^-$, ${O_2}^+$, NO^+, H_3O^+ (the concentration of electrons is negligible).

Water molecules present in the atmosphere, due to their high electric dipole moment, are attracted to these ions and prevent their recombination. This results in the formation of long-lived ion clusters, constituting the so-called near-ground plasma.

The atmospheric electric field causes ion separation, resulting in the so-called electrode effect: near the ground, there is an accumulation of positive ions, while negative ions are pushed upward. This generates an electric field, known as the anomalous electric field, which superimposes the atmospheric electric field.

This field is intensified by the simultaneous decrease in air conductivity caused by the release of aerosols from the Earth's crust. Another phenomenon originating near the Earth's surface is the emission of ULF, ELF, and VLF electromagnetic waves. The physical reasons for such emissions are not yet fully understood, but a possible explanation is related to the plasma frequency variation of the neutral cluster.

The anomalous electric field can propagate up to the E and F regions of the ionosphere, causing variations in electron concentration. Specifically, it is the component orthogonal to the geomagnetic field lines that penetrates these regions.

The change in electron concentration is the cause of the corresponding variation in the plasma frequency of the two regions. This alters the critical reflection frequency of electromagnetic waves, allowing them to propagate beyond the F2 layer.

Given the high conductivity of ionospheric plasma along the magnetic field lines, VLF waves can propagate without attenuation up to the Van Allen belts. The interaction of these waves with particles present in the belts leads to a variation in pitch angle and the

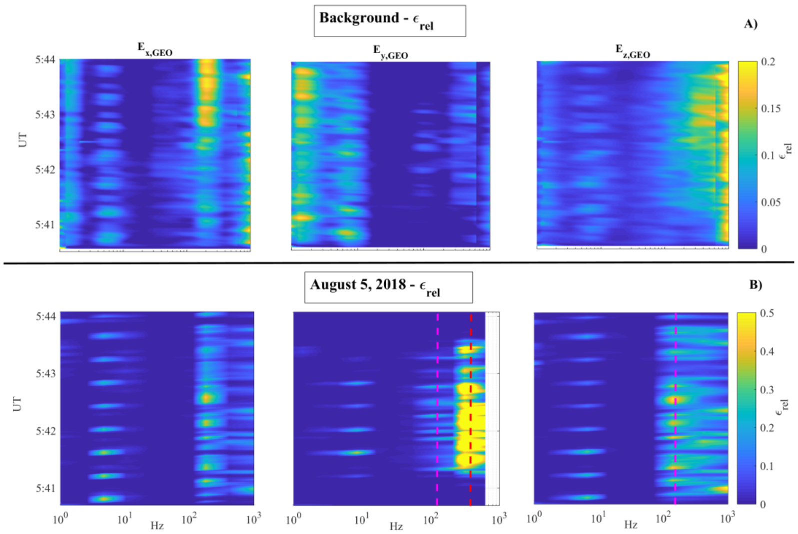

Figure 1.9: Relative energy spectrogram of the electric field components, obtained with data from EFD [11]

subsequent precipitation of these particles into the ionosphere.

Figure 1.8 shows a detailed schematic representation of the LAIC model, which includes other phenomena that, for simplicity, were not reported here.

1.2 Results from the CSES-01 satellite

This section will briefly present some of the results obtained from data acquired by the CSES-01 satellite during five years of flight. These results confirm the suitability of the CSES-01 satellite for the study of seismo-ionospheric coupling and space weather monitoring [16].

Bayan earthquake of the 5^{th} of August 2018

The CSES-01 satellite was able to detect some perturbances in the plasma density and the electric and magnetic fields ~ 6 hours before the $M_w = 6.9$ earthquake of the 5^{th} of August 2018 in Bayan (Indonesia). These perturbances were recorded by the Search-Coil Magnetometer (SCM), the Electric Field Detector (EFD) and the Langmuir Probe (LAP) present onboard.

Figure 1.9 and 1.10, show the spectrogram of the averaged relative energies ε_{rel} of the electric and magnetic fields components, measured with the EFD and SCM, during the CSES-01 flight over the earthquake region.

These relative energies are obtained by employing the Empirical Mode Decomposition (EMD), an analysis method based on the decomposition of a signal $s(t)$ into components, at different time scales, that are analyzed separately. These components are called Intrinsic Mode Functions (IMF) and are oscillating functions with variable frequencies. In this

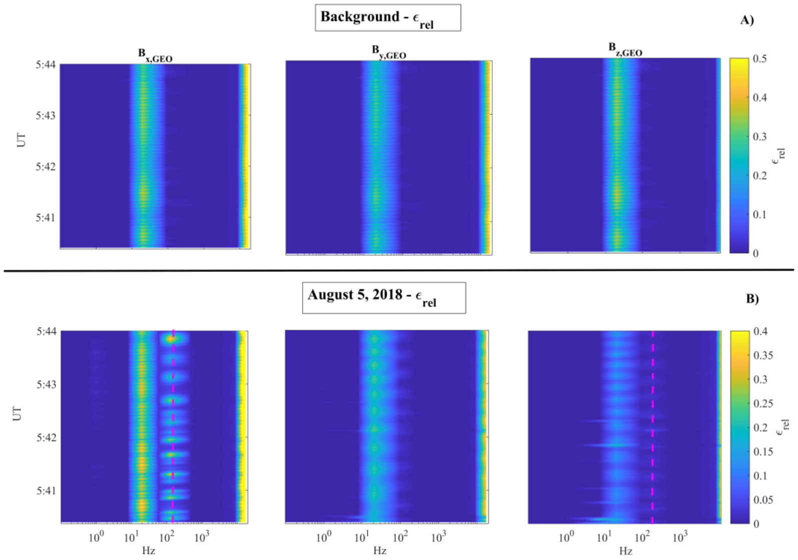

Figure 1.10: Relative energy spectrogram of the magnetic field components, obtained with data from SCM [11]

context, the signal can be written as $s(t) = \sum_{l=1}^{m} g_l(t) + r(t)$, where $g_l(t)$ is the IMF at scale l and $r(t)$ is the residue of the decomposition. The expression for the relative energy at scale l is:

$$\varepsilon_{rel}(l) = \frac{\int_l dt|g_l(t)|^2}{\int_l dt|s(t)|^2} \tag{1.13}$$

The relative energy $\varepsilon_{rel}(l)$ can be intuitively described as the measure of how “strong” the l component is in the signal. For more detail on the maths, please refer to [17] and [18].

Spectrograms on the first panel of figure 1.9, show the electric field background and it is possible to identify:

- resonance peaks at 2 Hz, caused by the motion of the satellite into the magnetic field
- the fundamental mode of the ionospheric Schumann's resonance at ∼ 7.9 Hz
- a portion of the whistler-mode chorus, generated around $L_{shell} = 5$ and propagating into the plasmasphere, at 270 Hz (visible in E_x component)
- the signature of the ionospheric hiss at ∼ 1 kHz, in E_x and E_z components

The same spectrograms, evaluated for 5 August 2018, are shown in the second panel of figure 1.9 and anomalous peaks are visible at ∼ 180 Hz for E_y and E_z. Another anomalous peak is present at ∼ 630 Hz for E_z.

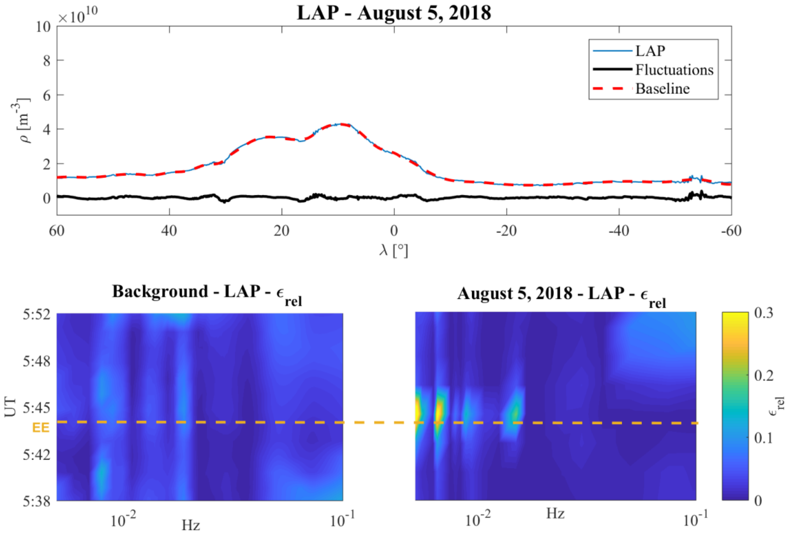

Figure 1.11: Relative energy spectrogram of the plasma density fluctuations, obtained with data from LAP [11]

The same analysis has been made for the magnetic field: in the first panel of figure 1.10, the background components show the third-order Schumann's resonance at 20 Hz and a peak at 12 kHz, related to the lower-hybrid resonance of the ionospheric F2 layer. The spectrograms in the second panel show anomalous peaks at $\sim$ 180 Hz for B_x and B_z. The comparison between these peaks with that of EFD shows that the components are orthogonal and thus it is an electromagnetic wave. From additional analysis of the Poynting flux, it has been obtained that this EM wave propagates upward.

In addition to these data, figure 1.11 shows the plasma density measurements acquired by LAP. The first plot shows the plasma density as a function of the latitude of the satellite and the black line represents the fluctuation over the baseline (in red). The EMD analysis has been made on this signal obtaining the two spectrograms of the background (on the left) and of the data acquired on **5th** of August.

This latter plot shows two anomalous densities with periods $T_1 = 67 \pm 1$ s and $T_2 = 111 \pm 1$ s just as the satellite flew over the earthquake's epicentre (the orange line).

The anomalies detected by EFD, SCM and LAP instruments can be explained by the MILC model presented in section 1.1.4, a mathematical description of the phenomena involved in this model is given in [11].

The geomagnetic storm of the 26th of August 2018

The HEPD-01 detected a strong geomagnetic storm that reached Earth on **26th** of August 2018. Figure 1.12 shows the particle rate measured for different energy thresholds, selected with three different trigger configurations that used an increasing number of calorimeter scintillators (similar configurations are implemented also in HEPD-02 and are described in section 3.3).

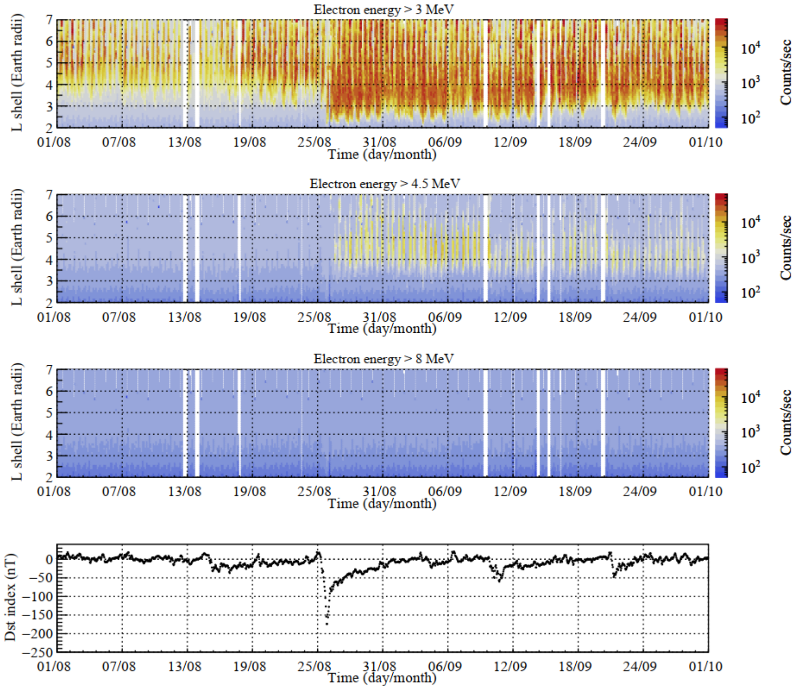

Figure 1.12: Particle rate acquired by HEPD-01 during the geomagnetic storm occurred on **26th** of August 2018 [19]

From these data, an increment in the electron rate is clearly visible in the first two plots for L-shells higher than 3. This increment is coincident with the lowering in the Dst (Disturbance storm time) index, which shows a weakening in the Earth's magnetic field caused by the storm. Further details are given in [19].

Galactic protons solar modulation

Data acquired by HEPD-01 from 6*th* of August 2018 to 5*th* of January 2020 allowed the study of galactic proton spectra with energies between 40 to 250 MeV.

Galactic protons in this energy range are strongly subjected to the effect of the solar wind, which can modify the flux of particles that reach the Earth (see [20] for more details).

The flight period of CSES-01 corresponded to the end of the 24*th* solar cycle and the beginning of the 25*th*, during which the solar activity was at the minimum and higher particle flux was expected.

Figure 1.13 shows proton fluxes as a function of the energy, in three different time periods. The comparison with predictions from the HelMod model, which takes into account solar modulation, and with data from SOHO/EPHIN spacecraft shows a good agreement for all three periods.

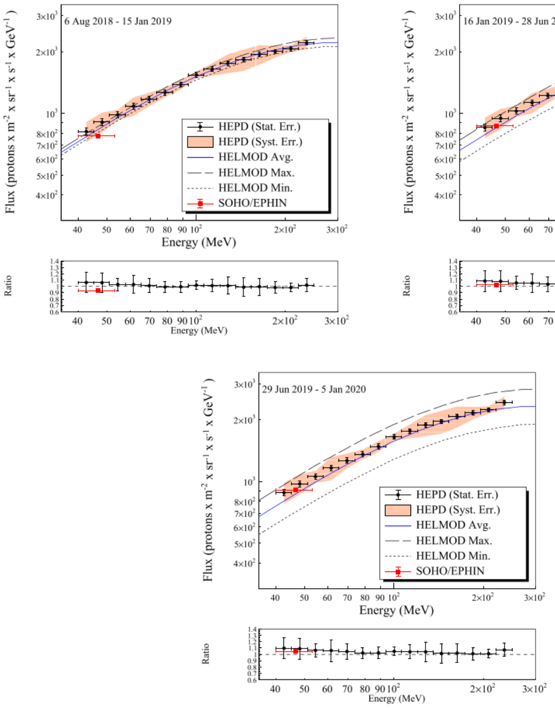

Figure 1.13: Galactic proton spectra as a function of energy measured by HEPD from 6^{th} of August 2018 to 5^{th} of January 2020 [20]

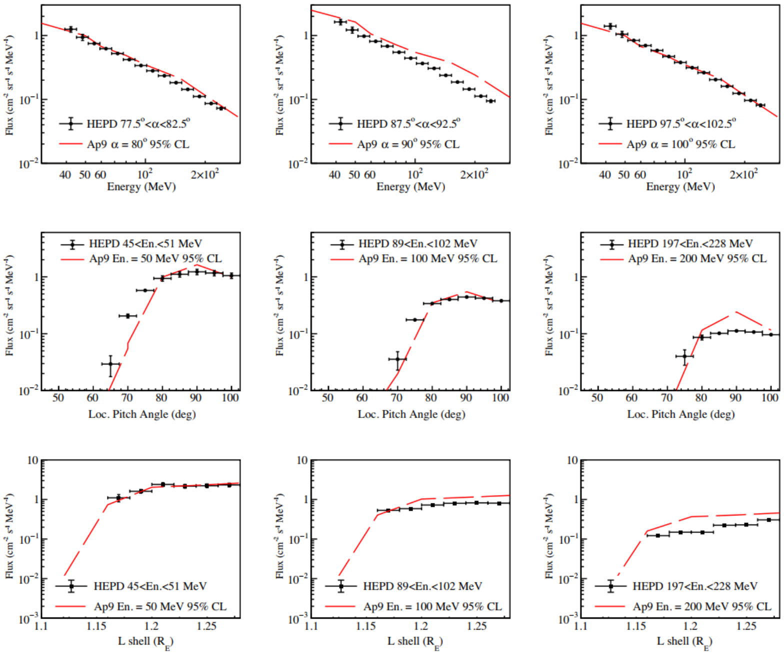

Figure 1.14: Proton fluxes in the SAA as a function of energy, local pitch angle and L-shell [21]

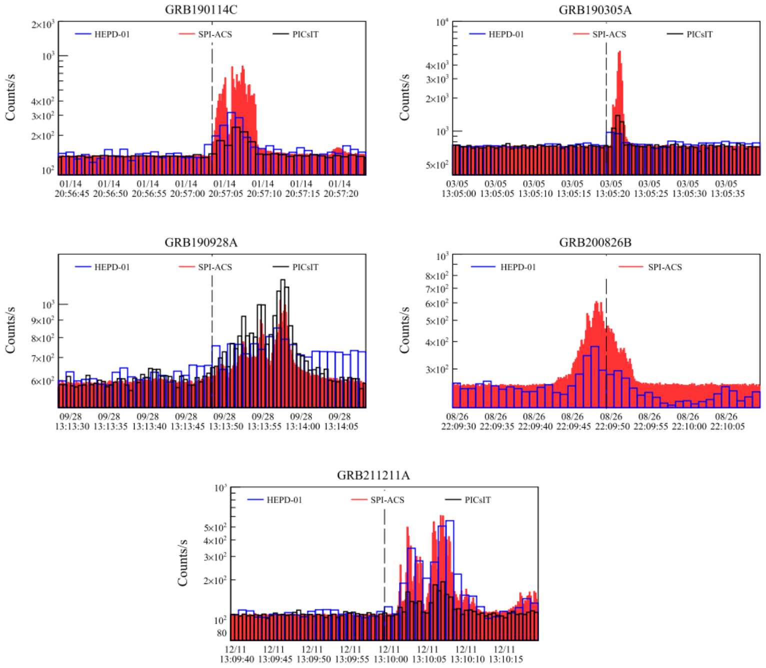

Figure 1.15: Time profiles of low-energy electrons detected by HEPD-01 and signals from SPI-ACS and PICsIT [23]

Trapped protons inside the SAA

HEPD-01 was also able to provide data for testing and validation of the AP9 model for protons trapped inside the SAA. These protons belong to the inner Van Allen belt and, for energies $\sim 10\,\mathrm{MeV}$, are produced by the decay of albedo neutrons originating from the interaction between Earth's atmosphere and cosmic rays, in a process called Cosmic Ray Albedo Neutron Decay (CRAND) [21][22].

An overall good agreement can be observed from plots in figure 1.14 that show proton fluxes as a function of the energy (on the first line), of the local pitch angle (second line) and the L-shell (third line). Some discrepancies are present for particles with higher energies where the model suffers from a reduced amount of data from experiments.

Gamma-Ray Burst Observations

An important result of HEPD-01 is the detection of five strong Gamma Ray Bursts (GRB) that opened the opportunity to provide the next calorimeter (HEPD-02) with new trigger configurations and algorithms dedicated to these phenomena.

Although HEPD-01 was not developed with GRB detection capabilities, the photon conversion inside elements like the tracker silicon planes and the aluminium structures of the mechanical frame made it possible thanks to the production of low-energy electrons, detected with the trigger configuration for the lowest energy.

Figure 1.15 shows the time profile of low-energy electrons compared with signals

Category	Payload name	Observation target
Particle energy	High-Energy Particle Detector (HEPD)	Electrons: 3 to 100 MeV Protons: 30 to 200 MeV
	Medium Energetic Electron Detector (MEED)	Electrons: 25 keV to 3.2 MeV
Electromagnetic field	Electric Field Detector (EFD)	Electric field: DC to 3.5 MHz
	High Precision Magnetometer (HPM)	Magnetic field: 10 Hz to 20 kHz
	Search Coil Magnetometer (SCM)	Magnetic field: 10 Hz to 20 kHz
In situ plasma	Plasma Analyzer Package (PAP)	Composition: H^+, He^+, O^+ N_i: $5 \cdot 10^2$ to $1 \cdot 10^7$ cm^{-3} T_i: 500 to 10 000 K
	Langmuir Probe (LP)	N_i: $5 \cdot 10^2$ to $1 \cdot 10^7$ cm^{-3} T_i: 500 to 10 000 K
Plasma profile construction	GNSS Occultation Receiver (GRO)	TEC by transmit VH/U/L signal
	Tri-Band Beacon (TBB)	TEC by transmit VH/U/L signal
	Ionospheric Photometer (IP)	O_2 135.6 nm and N_2 LBH airglow

Table 1.1: CSES-02 instruments and observation targets

from GRB-dedicated instruments (SPI-ACS and PICsIT).

The increments in electron rate measured by HEPD-01 are in good agreement with the shape and duration of the other signals [23]. Signals detected by HEPD-01 for GRBs 190305 and 190928 show a smaller increase in the particle rate, which can be explained by the fact that, during these GRBs, the satellite was close to polar regions where the background rate is higher.

1.3 The CSES-02 satellite

The CSES-02 satellite will be based on the CAST2000 platform and will be placed in a Sun-synchronous orbit with an inclination of 97°, a period of 94.6 min, and a revisiting period of 5 days. The second satellite will have a 180° phase shift with respect to CSES-01 in order to reduce the interval between the passage of the two satellites over the same region of the Earth.

Thanks to the improvement in the trigger system of the payloads, the satellite will be full-time operational along the whole orbit.

The instruments on board CSES-02 are listed in table 1.1 and can be divided into three main categories: particle detectors, electromagnetic field meters and ionosphere analyzers.

To the **particle detectors** category belongs the following instruments:

- **High-Energy Particle Detector (HEPD-02)**, described in detail in section 1.3
- **Medium Energetic Electron Detector (MEED)**, that measures electron energies in energetic ranges from 25 to 3200 keV and it is composed of two telescopes: the MEED-L for energies from 25 to 400 keV and the MEED-H for energies from 200 to 3200 keV. Its energetic range overlaps with HEPD-02 to validate results between the payloads

The **electromagnetic field meters** are:

- **Electric Field Detector (EFD)**, that measures the electric field from DC to 3.5 MHz. It is composed of 4 arms with voltage probes placed at their extremities. The electric field can be obtained, with a resolution of $1\,\mu\mathrm{V\,m^{-1}}$, using the relation $E_{ij} = \frac{V_i - V_j}{d_{ij}}$ where 'i' and 'j' are the probe indexes and d_{ij} is the distance between them

- **High Precision Magnetometer (HPM)**, for in-situ magnetic field measurements. It is composed of 2 vectorial and 2 scalar magnetometers and spans the frequency range from DC to 15 Hz

- **Search Coil Magnetometer (SCM)**, for measurements of magnetic field variations in frequencies from 10 Hz to 20 kHz.

The **ionosphere analyzers** are the following instruments:

- **Plasma Analyzer Package (PAP)**, that measures ionospheric plasma composition

- **Langmuir Probe (LP)**, used to measure ionospheric plasma parameters such as the electron density and the electric potential

- **GNSS Occultation Receiver (GRO)**, that uses signals from GNSS satellites to obtain information such as ionospheric TEC (Total Electron Content) and temperature profiles

- **Tri-Band Beacon (TBB)**, that measures ionospheric TEC

- **Ionospheric Photometer (IP)**, for measurements of the airglow from O_2 and N_2

2

The HEPD-02 detector

The HEPD-02 is designed to detect electrons, protons and light nuclei in energy ranges that go from 30 to 200 MeV for protons, from 3 to 100 MeV for electrons and up to 200 MeV per nucleon for heavier particles.

2.1 The detector structure

Figure 2.1a shows the rendering of HEPD-02: the left panel shows the assembled detector with the interface connectors on the top and the particle entrance window on the xy plane.

The right panel shows the internal structure of the detector with the stack of electronic boards on the left and the calorimeter on the right.

The structure of the detector can be schematized in four sections, which are depicted in figure 2.1b:

1. The direction detection
2. The trigger system
3. The calorimeter
4. The veto system

Different scintillators are used to convert the particle energy into light signals that are acquired by Photo Multiplier Tubes (PMTs). Each scintillator is coupled with two PMTs (Hamamatsu R9880-210) placed on opposite sides of each other, for a total of 64 PMTs [24].

A detailed description of the detector's sections follows [25][26].

The direction detection

The direction detection is designed to measure the entrance angle of the particles and it's composed of five turrets based on Monolithic Active Pixel Sensors (MAPS), based on those developed for the ALICE experiment at CERN and optimized for space applications

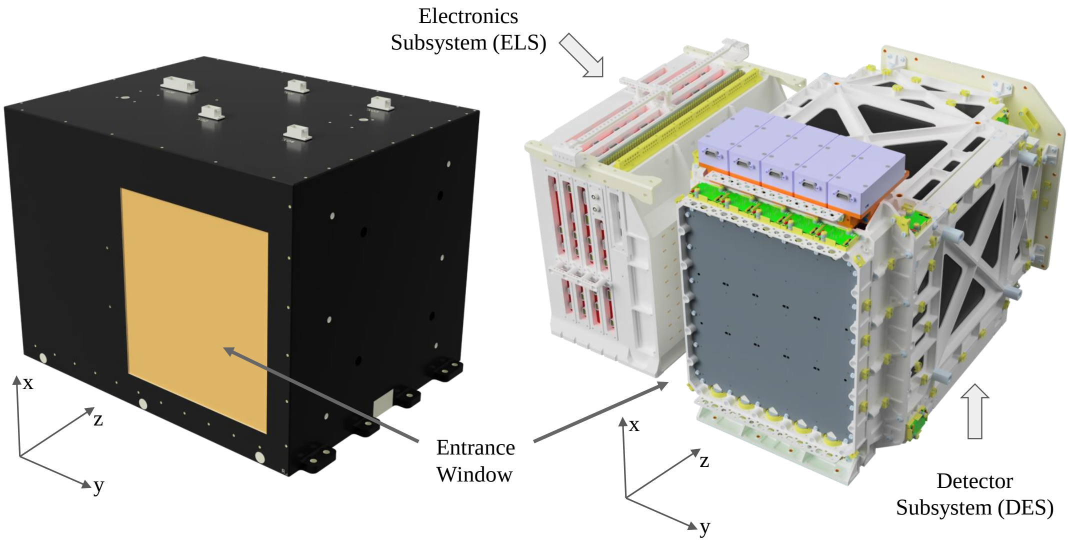

(a) HEPD-02 completely assembled (on the left) and its internal structure

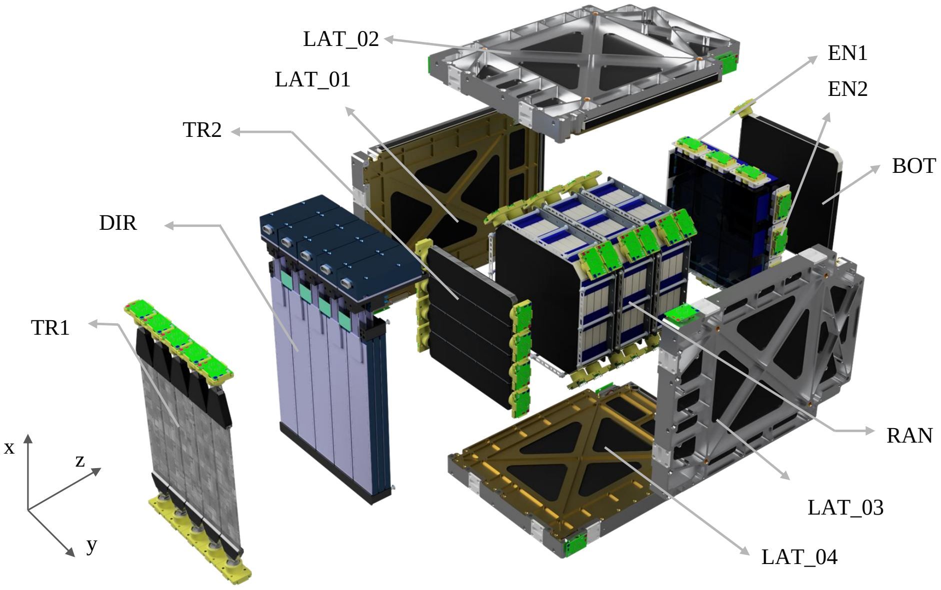

(b) Exploded view of the detector subsystem

Figure 2.1: HEPD-02 structure (courtesy of the CSES-Limadou collaboration)

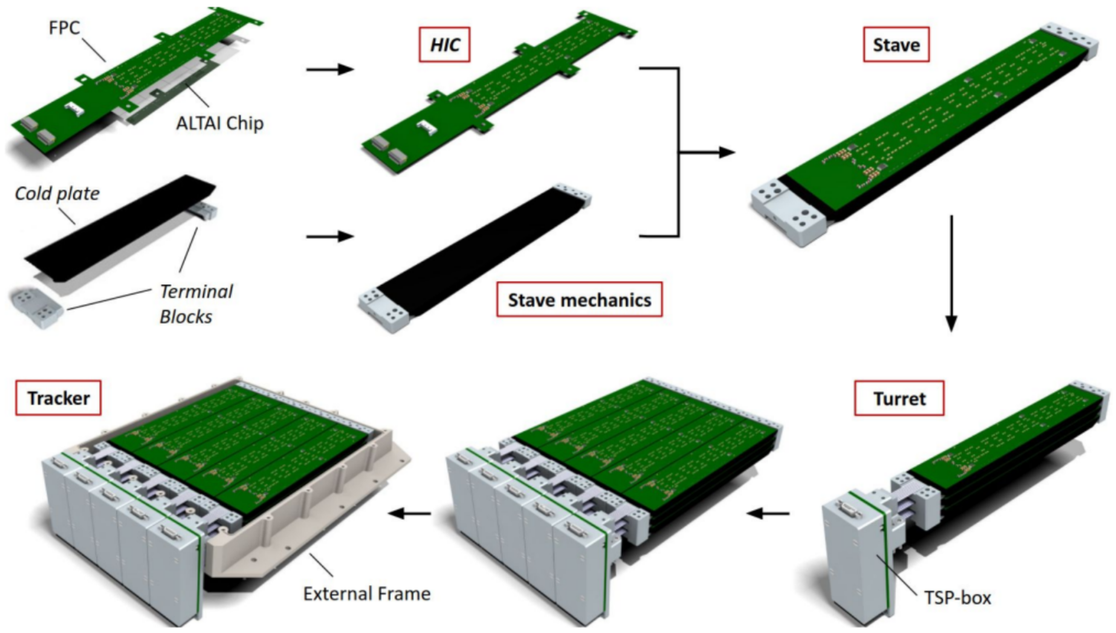

Figure 2.2: Detailed structure of the direction detector [27]

(ALTAI chips) [27][28][29][30]. Each turret is made of three sensitive planes that mount ten MAPS chips (see figure 2.2).

These chips are composed of 512×1024 pixels with a size of $28 \times 28\,\mu\text{m}^2$. The spatial resolution that can be obtained is approximately $4\,\mu\text{m}$.

HEPD-02 will be the first detector designed for space employing a pixel silicon tracker, which leads to an increased spatial resolution, better power consumption and low noise compared to the silicon microstrip tracker used in HEPD-01.

The segmentation of the direction detector allows to enable only the clock of the turret below the activated trigger segment and the adjacent ones, avoiding the readout of other turrets and lowering the power consumption. For this purpose, other measures were taken as well, such as the dynamic scaling of clock frequency, which allows for reducing the clock frequency when the satellite orbits in regions with lower trigger rates.

The turrets are managed by a dedicated electronic board called T-DAQ (Tracker Data Acquisition).

The trigger system

The trigger system is composed of two segmented planes of plastic scintillators (EJ-200) that surround the tracker. The segments of the two planes are placed orthogonally to each other.

The first plane, called TR1, allows the detection of particles with low energies thanks to its very low thickness, which also helps avoid multiple scattering. It is composed of 5 segments aligned with the turrets of the tracker ($154.6 \times 32.5 \times 2\,\text{mm}^3$). The two ends of

Characteristic	**EJ-200**	**LYSO**
Light yield (photons/1 MeV e^-)	10000	33200
Maximum emission (nm)	425	420
Light attenuation length (cm)	380	1.2
Rise time (ns)	0.9	0.2
Decay time (ns)	2.1	36
Density ($\mathrm{g\,cm^{-3}}$)	1.023	7.1

Table 2.1: HEPD-02 scintillators characteristics

these segments are coupled with trapezoidal light guides with different dimensions due to the geometry of the detector: one of the sides has a $25 \times 6\,\mathrm{mm}^2$ guide while the other is $46 \times 6\,\mathrm{mm}^2$.

The second plane, called TR2, is made of 4 segments ($150 \times 36 \times 8\,\mathrm{mm}^3$), placed orthogonally to TR1. This geometry allows us to have additional information on the trajectory of the entering particle and to activate only the necessary turrets of the direction detector readings.

The EJ-200 scintillator characteristics are described in table 2.1. The advantages of this material are the long optical attenuation length and the small decay time, which made it suitable for the HEPD-02 trigger purposes, reducing the dead time of the detector and avoiding signal pile-up.

The calorimeter

The calorimeter is made of twelve planes of plastic scintillators ($150 \times 150 \times 10\,\mathrm{mm}^3$), called RAN_1 to RAN_12, followed by two segmented planes of LYSO scintillators, which extend the energetic range of the detector thanks to their high density (see table 2.1).

The LYSO planes are called EN_1 and EN_2 and each one is divided into three bars ($150 \times 49 \times 25\,\mathrm{mm}^3$), displaced orthogonally to the ones of the other plane (see figure 2.1a).

The HEPD-02 will be the first space detector to use LYSO crystals of such a large size, their characteristics are described in table 2.1, while figure 2.3 shows the thickness of the HEPD-02 in terms of radiation length.

The important aspects of this material are the relatively fast decay time (compared with other inorganic scintillators), the high light yield and its high density. The LYSO crystals are used to extend the energetic range of the detector and are also the most suitable for detecting electromagnetic radiation, while the plastic scintillators are almost transparent to it. This also means that the threshold for photon detection is mainly dominated by the intrinsic radiation of the LYSO and any photon conversion in the plastic scintillators, preceding the LYSO layers, can be excluded. This allowed the implementation of the GRB detection algorithm (see section 3.7).

All the scintillators are wrapped in an aluminized Mylar tape that ensures proper light propagation and light-tightness. The LYSO are also covered with PVC black tape to avoid optical cross-talk that could arise given their high light yield.

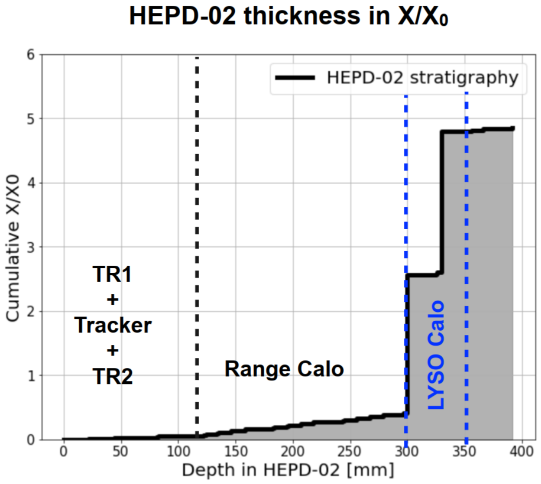

Figure 2.3: Radiation length of the HEPD-02 detector (courtesy of the CSES-Limadou collaboration)

The veto system

The calorimeter is surrounded by five planes of EJ-200 scintillators [31] that act as a veto system, and allow the identification of particles that are not contained inside the detector or enter from the side or the bottom of it.

The lateral planes are called LAT, while the bottom scintillator is called BOT.

Photomultiplier tubes

All the light pulses produced by the scintillators are collected by R9880-210 photomultiplier tubes (PMT) from Hamamatsu [32][33].

The advantages of these PMTs are the small dimensions (12 mm height and a diameter of 16 mm for an effective area of 50 mm^2), a wide operating temperature range and the efficiency spectrum peaked to 425 nm, that matches the emission peak of the scintillators.

Each scintillator is coupled with two PMTs, for a total of 64 PMTs, through EJ-560 silicon rubber optical pads, to ensure good optical contact. The signals from these photomultipliers are acquired by an electronic board called “PMT readout and trigger system” (referred to as PMT&T), which is described in chapter 3. The connection between PMTs and the board is made using RG178 coaxial cables, which ensure good noise immunity.

2.2 Electronics

The electronic subsystem of HEPD-02 is composed of:

- **HV-CTRL** (High Voltage Control), designed for the control of the High Voltages for the PMTs

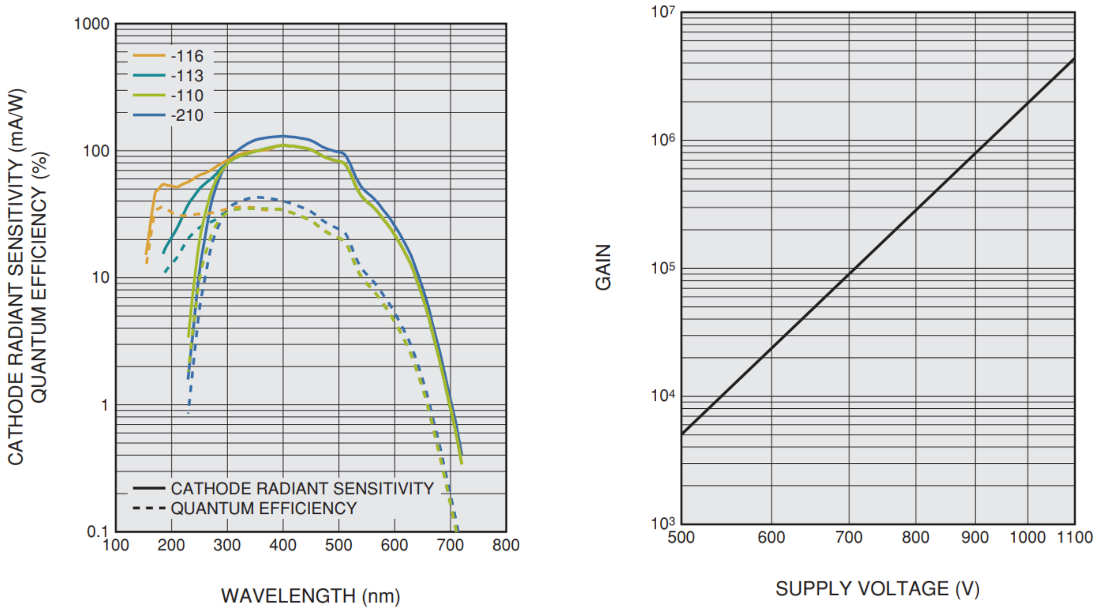

(a) Cathode sensitivity and quantum efficiency

(b) PMT gain versus applied voltage

Figure 2.4: Hamamatsu R9880-210 characteristics [32]

- **LV-CTRL** (Low Voltage Control), that controls the power of the other boards and the direction detector
- **T-DAQ** (Tracker Data Acquisition), used for the readout of the MAP sensors of the tracker
- **PMT&T** (PMT readout and Trigger), designed for the acquisition and digitization of the PMT signals and the generation of the trigger signal for the detector
- **DPCU** (Data Processing and Control Unit), that controls all the subsystems, stores their data and manages the communication towards the satellite

All the subsystems are designed with HOT/COLD redundancy and communicate with DPCU via SpaceWire Lite protocol.

A detailed description of these boards and their operation follows. The PMT&T board will be described in chapter 3.

HV-CTRL board

The High Voltage Control board allows the regulation of the bias for the 64 PMTs of the calorimeter.

It is based on Microsemi Proasic3E FPGA and uses 16 DC/DC step-up modules (Aerospazio HV3) to produce the High Voltage bias.

Figure 2.5a shows a schematic description of the board.

The PMTs are grouped into 16 groups to cope with the limited number of step-up modules. The HV bias can be regulated up to 1200 V with a 1/1024 resolution and can be monitored through dedicated V_{mon} lines digitized with AD7276 ADCs.

LV-CTRL board

The Low Voltage Control board manages the power for the detector's subsystems and is designed to convert the 29.5 V, from the satellite power bus to the 12 V required for the other boards. It includes various protection elements that prevent anomalous current consumption from the subsystems.

A schematic description of this board is shown in figure 2.5b.

T-DAQ board

The T-DAQ board is based on Xilinx XC7A100T FPGA and acquires data from the direction detector, performing the following operations:

- Configures the MAPS chips and manages the acquisition and their calibration
- Manages signals from and to the PMT&T board
- Pack the data and transfer it to the DPCU board

DPCU

The DPCU is based on Xilinx Zynq XC7Z7045 FPGA and its main functions are the following.

- Control of the other subsystems (T-DAQ, LV/HV-CTRL and PMT&T)
- Communication with the satellite platform with CAN BUS and RS422 protocols
- Control of HEPD-02 modes (stand-by, safe mode and nominal mode)
- Management of HEPD-02 calibration and acquisition
- Acquisition and packing of data from PMT&T and T-DAQ and transmission to the satellite
- Recovery procedure in case of system malfunctioning

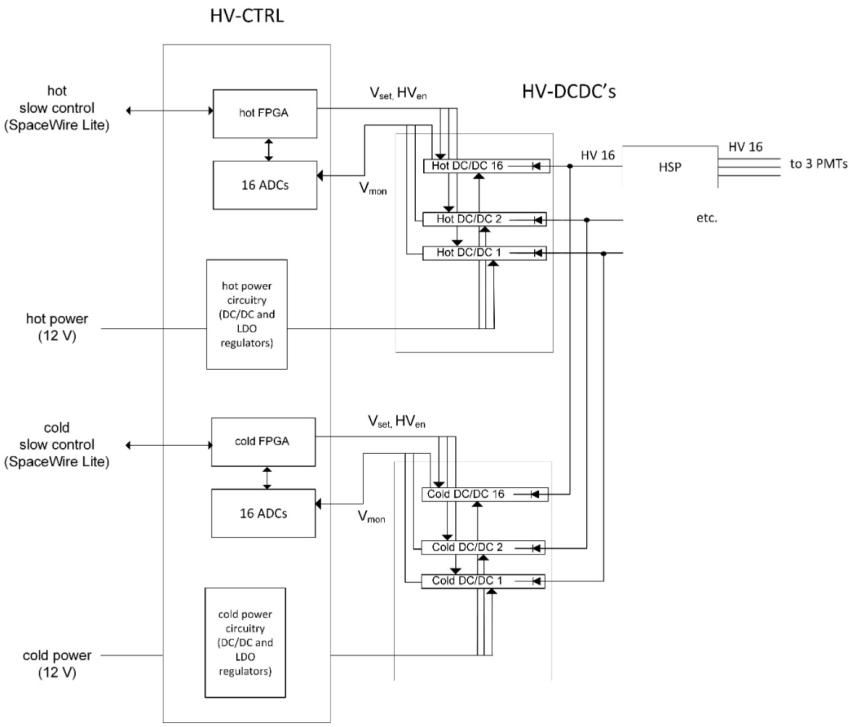

(a) HV-CTRL board schematics

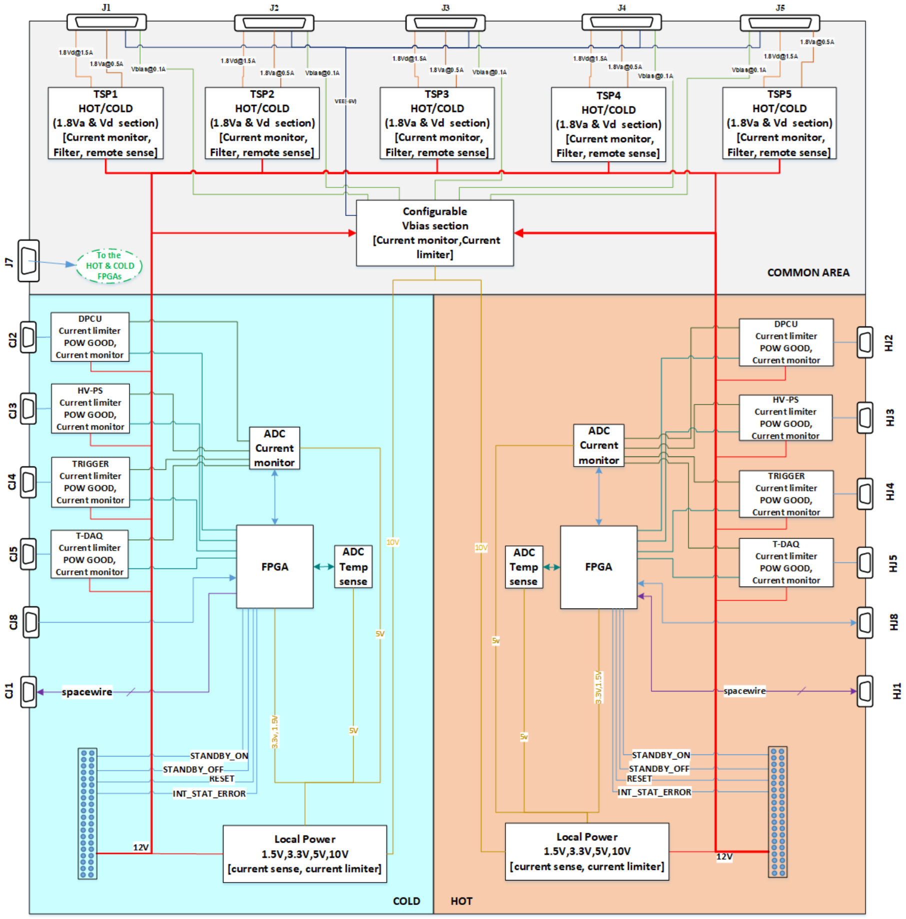

(b) LV-CTRL board schematics

Figure 2.5: Schematics of the LV and HV Control boards (courtesy of the CSES-Limadou collaboration)

3

The PMT readout and trigger system

All the signals coming from the PMTs coupled to HEPD-02 scintillators are acquired, sampled and digitized by an electronic board (the PMT&T board), based on CITIROCs readout chip (by Weeroc) and A3PE3000L FPGA (by Microsemi) [34].

My main activity as a PhD student was the development of the PMT&T system, including the writing of its firmware and the characterization of the CITIROCs response and linearity to the signal of interest for HEPD-02.

Since the detector will operate in space, three models of the board have been realized: an Engineering Model (EM), used for development and tests, a Qualification Model (QM) used for environmental and acceptance tests in the most stressful conditions, and a Flight Model (FM), intended for flight and identical to the QM but subjected to tests in less severe conditions.

The realization of the QM and FM boards has been committed to a company specialized in space electronics (the TSD-Space company) with whom I cooperated for the definition of implementation details and optimizations.

The main functions of the PMT&T board can be summarized as follows:

- Readout and digitization of the 64 PMTs' signals using CITIROCs

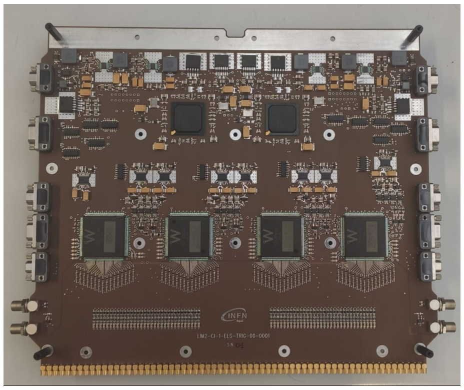

Figure 3.1: The PMT&T board

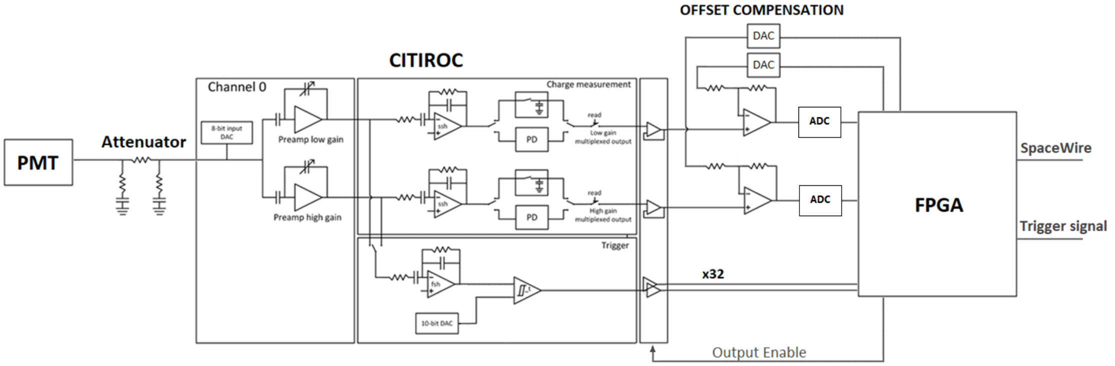

Figure 3.2: Schematic description of the PMT&T board

- Configuration of the CITIROCs' preamplifier's gain and the trigger threshold
- Selection of different trigger configurations (trigger masks) to optimize sensitivity for different orbital zones and different energy
- Measure of the particle rates by means of rate meters for each PMT and trigger configuration

Most of these functions are implemented through the FPGA. Figure 3.2 shows a schematic description of the board.

The PMT signals are collected from the last dynode and not from the anode because CITIROCs are designed for SiPMs, which have a positive polarity and would not work with the detector's PMTs that produce negative signals.

Since the last dynode produces positive-polarity signals, it is possible to adapt them to the CITIROCs' input range with "pi pad" resistive voltage dividers. This solution allows avoiding the use of inverters, keeping the board consumption low.

The attenuation factors are reported in table 4.2 and have been chosen considering that, to have a low energy threshold for the experiment, the T1 scintillators must be very thin and their outputs are pulses with small amplitude and width, compared with the other scintillators.

After these attenuators, the signals are acquired by CITIROCs that amplify, shape and memorize them and produce trigger signals for each channel. These triggers are then acquired by the FPGA which produces a global trigger if the selected trigger conditions are met. This global trigger enables the CITIROCs outputs and starts the ADC conversion.

The use of ASICs for the readout of PMTs allows for reduced power consumption (an essential requirement for space missions) and a high number of channels to acquire all the scintillator's signals. In particular, CITIROCs offer features such as configurable gain and shaping time that improve the flexibility of the detector and the peak detection circuit, used for acquiring signals spread in time.

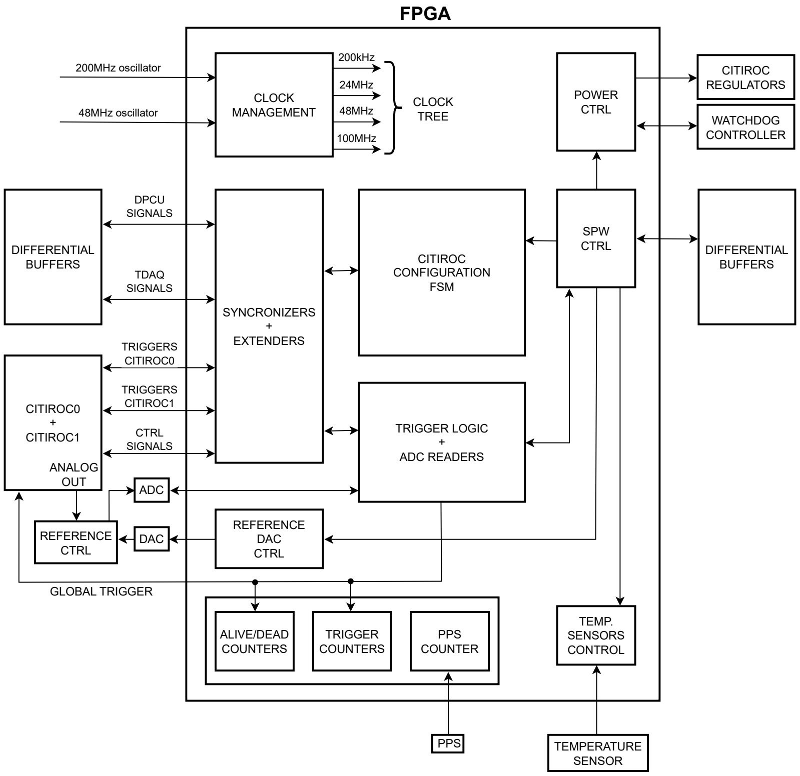

Figure 3.3: Schematic representation of the PMT&T board firmware

3.1 General architecture of the PMT&T FPGA's firmware

The general architecture of the firmware loaded on the PMT&T FPGA is schematized in figure 3.3 and can be divided into the following sections:

- Clock management
- Power and watchdog control
- Signal synchronizers and extenders
- SpaceWire controller
- CITIROCs offset compensation controller
- Counters
- Temperature sensors controller
- CITIROCs configuration FSM
- Trigger logic and ADC readers

The board mounts two crystal oscillators that produce a 48 MHz clock and a 200 MHz clock.

The **clock management** section provides a series of clock dividers that allow the generation of the following internal clocks:

- a 24 MHz clock, used for ADC readers
- a 48 MHz clock, used for almost all of the finite state machines of the board
- a 100 MHz clock, used for the trigger logic FSM
- a 200 kHz clock, used for CITIROC readout

Since the board had to meet the requirements for operation in space, it was not possible to use a PLL to produce all the clocks due to its radiation sensitivity, hence the use of the dividers and the two different oscillators.

When the PMT&T board turns on, the CITIROCs are not powered to avoid excessive absorption peaks during the start-up, when all the capacitors on the board charge.

The **power control** module allows to enable the regulators connected to the analogue and digital power sections of CITIROCs. Their power-on can be controlled by means of two bits of the `CMD_REG` SpaceWire register (see table 3.1). This section also provides an FSM that controls the watchdog timer reset signal.

External signals (such as triggers from CITIROCs or the BUSY from DPCU and TDAQ) are synchronized with the internal clock using a series of dual flip-flop synchronizers, instantiated in the **signal synchronizers and extenders** module. To ensure a correct sampling, these signals are also extended to 100 ns.

The communication with the other boards is made by a SpaceWire register-based protocol. The **SpaceWire controller** module is designed to decode the serial signals into a sequence of addresses and data. An FSM is used to store data in a series of 32-bit internal registers. A brief description of these registers is shown in table 3.1, some of them will be detailed in the next sections.

Various **counters** are implemented in the PMT&T board in order to have information on the trigger rate and the alive and dead time of the detector.

These counters will be described in the next sections. In addition to these, a PPS counter is used to synchronize data between the subsystems of HEPD-02.

The board mounts two AD7814 temperature sensors, placed in regions of the board that are supposed to be the hottest during the operation. The **temperature sensor controller** manages the communication with these two sensors and stores the two 16-bit values in the `BOARD_TEMP` register.

3.2 CITIROCs

The readout of PMTs is actually made using CITIROCs integrated circuits. The internal structure of these ASICs is schematized in figure 3.4 and described below [35].

Address	Name	Description
0x00	ID_REG	Board ID
0x01	STATUS_REG	Reports the status of the board
0x03	RST_REG	Used for software reset
0x04	CLK_REG	Clock counter (used for debug)
0x05	RW_REG	Read/Write register (used for debug)
0x08	CMD_REG	Used for sending commands to the PMT&T board
0x09 - 0x2C	CONFIG_CITIROC	Used for the configuration of CITIROCs
0x51	TRIGGER_MASK	Sets the trigger mask
0x52	GENERIC_TRIGGER_MASK	Sets the generic trigger mask
0x53	PMT_1_MASK	Masks a specific channel connected to CITIROC1
0x54	PMT_2_MASK	Masks a specific channel connected to CITIROC2
0x56	BOARD_TEMP	Reports the value of the temperature sensors
0x57 - 0x76	PMT_RATE	Stores the rate for each channel
0x77 - 0x7C	MASK_RATE	Stores the rate for each trigger mask
0x7F	TRG_COUNTER	Trigger counter
0x80	PPS_COUNTER	PPS counter
0x81	MASK_RATE_GRB	Stores the rate for the GRB trigger masks
0xA0	REF_DAC_1	Sets the pedestals (HG and LG) for CITIROC1
0xA1	REF_DAC_2	Sets the pedestals (HG and LG) for CITIROC2
0xB2	PCKTS_IN_FIFO	Counts packets present in the FIFO
0xB3	ACQDATALEN	Reports the length of the packet
0xB4 - 0xF1	ACQDATA	Trigger event data (240 bytes)
0xFD	PRESC_T3_T2	Sets the prescaler value for T2 and T3 triggers
0xFE	PRESC_T1_T0	Sets the prescaler value for T0 and T1 triggers

Table 3.1: SpaceWire 32-bits registers

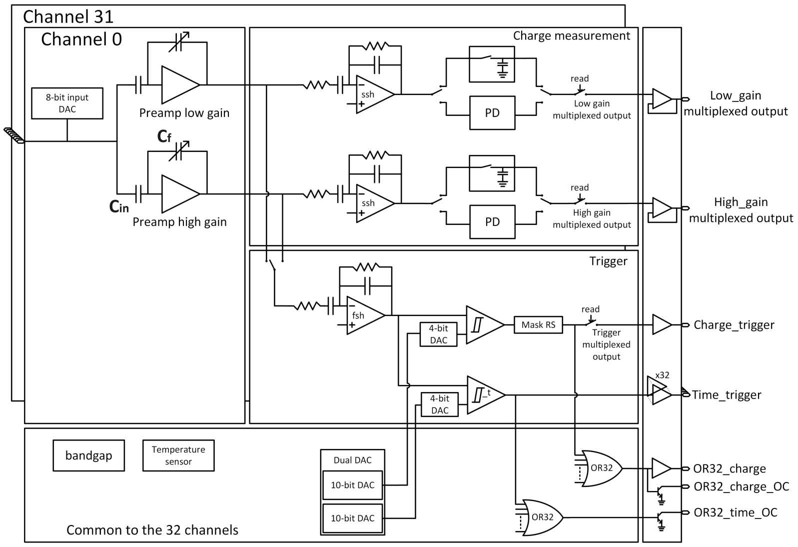

Figure 3.4: CITIROC internal structure [35]

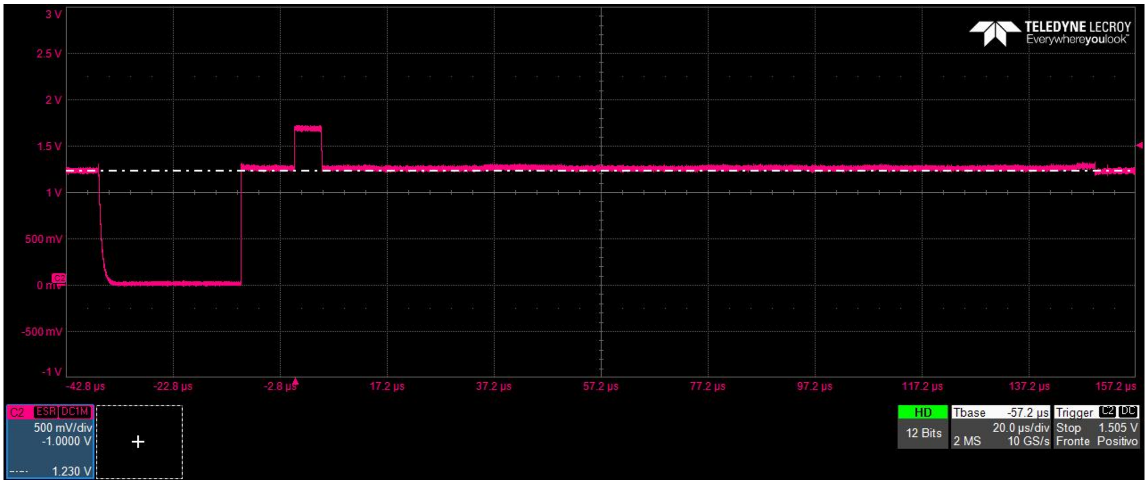

Figure 3.5: Analogue output of CITIROCs

For each channel of the CITIROC, a first amplification stage is present with two independent charge preamplifiers with different gain ranges:

- **High Gain** (HG) with gain from 10 to 600
- **Low Gain** (LG) with gain from 1 to 60

These are nominal values based on the following relation:

$$G = \frac{C_{in}}{C_f} \tag{3.1}$$

Where C_{in} is the capacitance of the input capacitor and C_f is the capacitance of the feedback one (see figure 3.4).

In section 4.3 it will be shown that, for high values, the actual gains differ from nominal ones.

The dual amplification structure allows for a wide dynamical range which is essential due to the wide energy range required for HEPD-02.

The two preamplifier outputs are connected with two shapers with a configurable shaping time that can be selected between 12.5 to 87.5 ns with 12.5 ns steps and the output signal can be stored in analogue memory circuits which can operate in the following modes:

- **Track&Hold**, in which the output of the shaper is sampled at a specific instant, determined by a hold signal
- **Peak Detection**, used to follow the shaper signal in a defined time window

In the case of HEPD-02, the Peak Detection mode is used, due to the different timing characteristics of the various scintillators and the presence of delay between channels. This mode will be described in the next section.

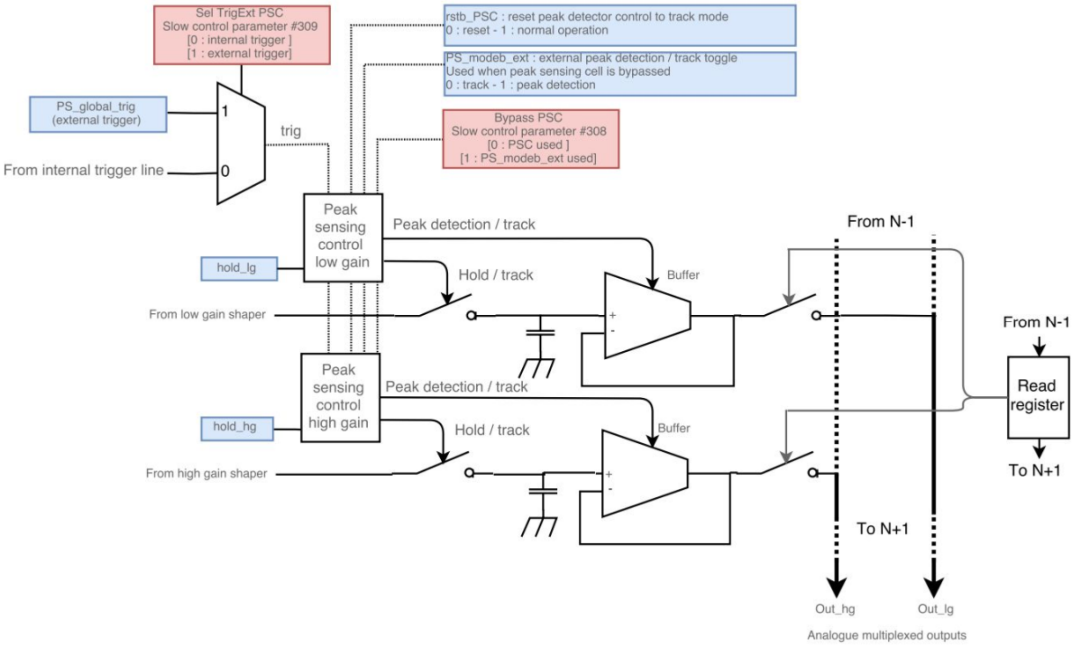

Figure 3.6: Block scheme of the peak detector [35]

For each channel of the CITIROC, a trigger signal is produced, referenced here as a "single-channel trigger" to avoid misunderstandings.

The single-channel triggers are produced by means of "fast shapers" with a fixed shaping time of 15 ns and Schmitt triggers whose threshold can be configured with a 10-bit DAC.

In figure 3.4 these single-channel triggers are called "Time_triggers", the multiplexed trigger (called "Charge_trigger") is not used.

The 64 single-channel triggers, produced by the two CITIROCs, are acquired by the FPGA that implements the trigger masks and produces a global trigger signal. The global trigger, in turn, enables the analogue output of the CITIROCs and starts the ADC conversions.

Figure 3.5 shows an example of the CITIROC analogue output when channel CH03 was pulsed. During the first 25 μs the output goes to a High-Z state, and then the voltages stored in the peak detection circuit capacitors are sequentially output over an offset of approximately 1.25 V.

Each channel output lasts 5 μs, compatibly with the 200 kHz clock used for CITIROC readout.

3.2.1 Peak Detector

The use of peak detection mode is one of the improvements made to HEPD-02: instead of sampling the shaper's signal at a given time (as in the Track&Hold mode) a window is defined, during which a capacitor is charged with the shaper's output.

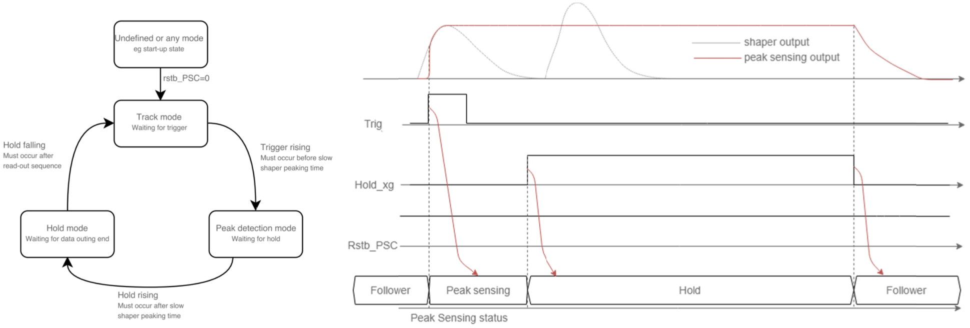

(a) **(b)**

Figure 3.7: Peak detector’s FSM description (a) and timing diagram (b) [35]

The schematics in figure 3.6 show the internal operation of the peak detection circuit. The “peak sensing control” (PSC) modules manage the connection of the slow shapers (High and Low Gain) with the capacitors that store the peak and with the output buffers.

When the external trigger is asserted, the PSC goes into the ‘’Track mode” (see figure 3.7a), during which the shapers are connected to the capacitors and the buffers’ outputs are disabled.

This state is maintained until the HOLD signal is asserted, which puts the state machine in the ”Hold mode” and disconnects the shapers. Specifically, the PMT&T board produces the HOLD signal 220 ns after the trigger validation. In section 4.4, the measurements made to verify this time window are shown.

At the falling edge of the HOLD signal, the output buffers are enabled and, using the “Read register”, it is possible to connect sequentially these buffers to the analogue outputs of CITIROCs, reading the capacitor values channel by channel.

3.2.2 CITIROC configuration FSM

The configuration of CITIROCs is managed by two identical finite-state machines implemented in the FPGA.

A simplified diagram of these FSMs is shown in figure 3.8.

The initial state is the `pwrOFF` that checks the power-on signal for the CITIROC. This signal is produced by writing `‘1’` in the 4th or 5th bit of the `CMD_REG` register, depending on which CITIROC must be powered (see table 3.2). These bits must be kept at `‘1’` to maintain the CITIROCs powered.

When the `pwrON` signal is asserted, the FSM waits for 500 ms to ensure that the power reaches the expected voltage and that all the internal capacitors of CITIROCs are charged. When this time elapses, a `pwrReady` signal is asserted and the FSM goes into the `CITrst` state where the internal CITIROC configuration registers are reset.

During the `CITcfg` state, the internal CITIROC’s registers are written with the configuration and then the FSM goes into the `idle` state.

In this state, the FSM waits for a `configure` command which starts a new configu-

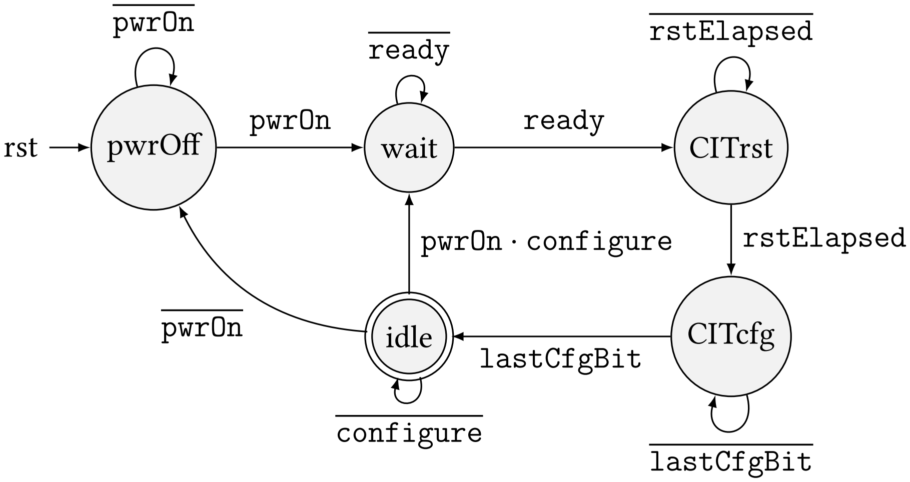

Figure 3.8: CITIROC configuration FSM diagram

	`CMD_REG` (0x08)															
Register bit	31-15	14	13	12	11	10	9	8	7	6	5	4	3	2	1	0
Description	Calibration period	Apply CIT offset	Unused	Stop Calib.	Start Calib.	Stop Acq.	Start Acq.	Apply PMT mask	Apply TRG mask	Debug trg	PwrOn CIT2	PwrOn CIT1	Unused	Enable Temp. sensors	Configure CIT2	Configure CIT1

Table 3.2: Command Register description

ration. This command can be produced using the first two bits in the `CMD_REG` register, depending on which CITIROC needs to be configured.

This FSM ensures that every time a CITIROC is powered on, a configuration with default values is always made, avoiding unpredictable start conditions.

The configuration parameters can be changed using the SpaceWire registers from address 0x09 to 0x2C.

3.2.3 CITIROCs offset compensation controller

As previously observed, the analogue output of the CITIROCs has an offset of 1.25 V (see figure 3.5). Converting this output without removing the offset would lead to a reduction of the dynamic range of the ADCs by half.

Since the analogue output of CITIROCs has a maximum value of 2.5V, a simple voltage subtraction would still result in half the ADCs' dynamic.

To avoid these problems, the "OFFSET COMPENSATION" circuit is used, shown in figure 3.2. A more detailed schematic is shown in figure 3.9.

In addition to removing the offset, it also amplifies the voltage to adapt it to the input dynamic range of the ADCs.

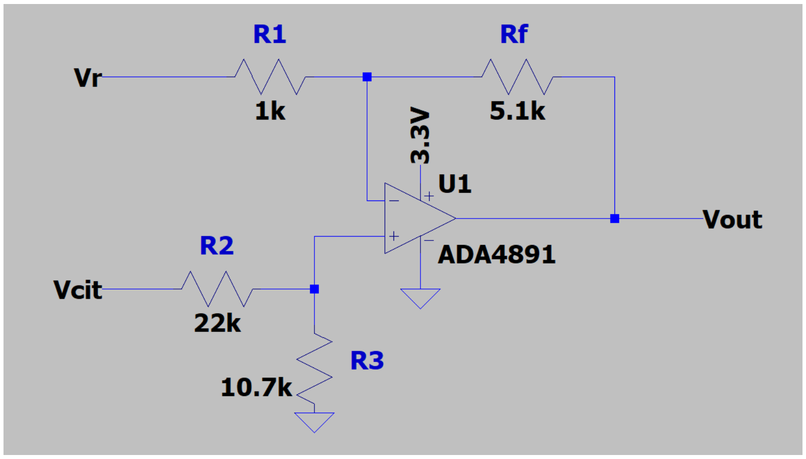

Figure 3.9: CITIROCs offset compensation circuit

`REF_DAC_1` (`0xA0`) and `REF_DAC_2` (`0xA1`)		
Register bit	`31-16`	`15 - 0`
Description	High Gain offset	Low Gain offset

Table 3.3: CITIROCs offset compensation registers description

The relationship between the input voltage and the output can be obtained by the following equation:

$$V_{out} = \frac{R_1 + R_f}{R_1} \cdot \frac{R_3}{R_2 + R_3} \cdot V_{cit} - \frac{R_f}{R_1} \cdot V_r \tag{3.2}$$

Where V_r is the voltage produced by the DAC and V_{cit} is the voltage produced by the analogue output of the CITIROC.

Using the actual values for the resistors, the equation 3.2 becomes:

$$V_{out} \simeq 2\, V_{cit} - 5\, V_r \tag{3.3}$$

The DACs present on the board can be configured using the `REF_DAC_1` and `REF_DAC_2` registers, as shown in table 3.3. This makes possible the fine-tuning of pedestals in charge distributions.

To obtain the variation in ADC counts, produced by variations in the value written in these registers, the following relation can be used.

$$\Delta P \simeq -0.31\, \Delta D \tag{3.4}$$

Where ΔP is the variation in the pedestal's ADC counts and ΔD is the variation in the `REF_DAC_1` or `REF_DAC_2` values.

This relation can be obtained considering that the V_{out} signal is converted by a 12-bit

D (hex)	D (dec)	P	σ_P
0x3200	12800	89.2	1.8
0x3264	12900	57.5	1.8
0x32C8	13000	27.2	1.7

Table 3.4: CITIROCs offset compensation calibration

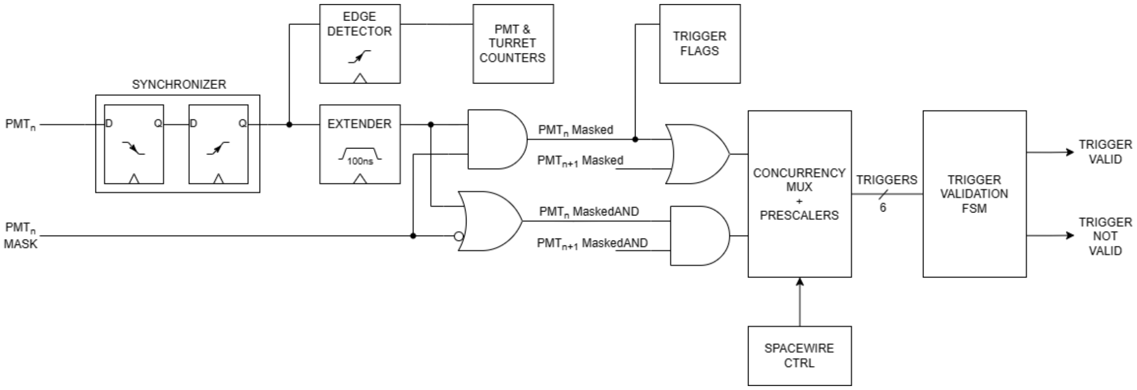

Figure 3.10: Block scheme of the trigger logic module

ADC (AD7274 by Analog Devices [36]), with a voltage reference of 2.5 V, that gives:

$$\frac{dP}{dV_{out}} = \frac{4095}{2500\,\text{mV}} = 1.638\,\frac{LSB}{\text{mV}} \tag{3.5}$$

While the DACs are 16-bit (AD5662 by Analog Devices [37]), with the same reference voltage of the ADCs:

$$\frac{dV_r}{dD} = \frac{2500\,\text{mV}}{65535} \simeq 0.038\,\frac{\text{mV}}{LSB} \tag{3.6}$$

Since equation 3.3 gives $\frac{dV_{out}}{dV_r} = -5$, then it is possible to obtain the 3.4:

$$\frac{dP}{dD} = \frac{dP}{dV_{out}} \cdot \frac{dV_{out}}{dV_r} \cdot \frac{dV_r}{dD} \simeq 1.638 \cdot (-5) \cdot 0.038 \simeq -0.31 \tag{3.7}$$

To verify this relation, a simple characterization has been done with three points. Table 3.4 reports the mean of the pedestal distributions for the High Gain preamplifier of channel CH00 of CITIROC0, varying the DAC digital value.

A linear fit for these values gives $P = -(0.310 \pm 0.004)D + (4057 \pm 52)$, compatibly with equation 3.4.

3.3 Trigger logic

One of the main components of the PMT&T board firmware is the module that manages the trigger logic and the acquisition of data from ADCs. In figure 3.10 a block scheme of this module is shown.

This module is developed to implement a highly flexible trigger system, which meets the following mission requirements: operation of the satellite along the whole orbit (including regions with high particle rates such as the SAA and the poles), the possibility to select more than one trigger in concurrence to study different physics cases and the control of the bandwidth sharing using trigger prescaling. These features extend the scientific reach of the mission, allowing for an in-depth study of particles in SAA and pole regions and adding sensitivity to Gamma Ray Bursts.

The first stage of the trigger logic synchronizes the 64 single-channel triggers, produced by the two CITIROCs, to the internal 100 MHz clock and extends their duration to 100 ns, to ensure the superposition of signals.

As mentioned before, every scintillator is coupled with two PMTs that are connected on the same channel of different CITIROCs. For example, the RAN_01 scintillator is coupled with the PMTs named RAN_01_B and RAN_01_D: the RAN_01_B PMT is connected to channel CH09 of CITIROC0, while RAN_01_D is connected to the same channel on CITIROC1.

To avoid spurious triggers, that can be produced by damaged PMTs, the extended signals can be masked by the `PMT_1_MASK` and `PMT_2_MASK` registers' bits (see table 3.5). Two independent circuits mask the signals, depending on which combination will be used in the trigger: if the OR of two PMTs is required, a simple AND between the PMT mask and the extended signal is used. Otherwise, if the AND of two PMTs is needed, the OR between the signal and the negated PMT mask bit is used (figure 3.11 shows an example with RAN_01_D and RAN_01_B extended signals and the ninth bit of the PMT_1,2_MASK registers).

This way, when the corresponding bit of the `PMT_1,2_MASK` is `'0'`, the result of the AND or the OR, will not depend on the masked single-channel trigger.

PMT_1_MASK (0x53) and PMT_2_MASK (0x54)																																
Register bit	31	30	29	28	27	26	25	24	23	22	21	20	19	18	17	16	15	14	13	12	11	10	9	8	7	6	5	4	3	2	1	0
Description	CH31 (LAT_04_x)	CH30 (LAT_03_x)	CH29 (LAT_02_x)	CH28 (LAT_01_x)	CH27 (BOT_x)	CH26 (EN2_03_x)	CH25 (EN2_02_x)	CH24 (EN2_01_x)	CH23 (EN1_03_x)	CH22 (EN1_02_x)	CH21 (EN1_01_x)	CH20 (RAN_12_x)	CH19 (RAN_11_x)	CH18 (RAN_10_x)	CH17 (RAN_09_x)	CH16 (RAN_08_x)	CH15 (RAN_07_x)	CH14 (RAN_06_x)	CH13 (RAN_05_x)	CH12 (RAN_04_x)	CH11 (RAN_03_x)	CH10 (RAN_02_x)	CH09 (RAN_01_x)	CH08 (TR2_04_x)	CH07 (TR2_03_x)	CH06 (TR2_02_x)	CH05 (TR2_01_x)	CH04 (TR1_05_x)	CH03 (TR1_04_x)	CH02 (TR1_03_x)	CH01 (TR1_02_x)	CH00 (TR1_01_x)

Table 3.5: PMT Mask register description

The signals produced by this logic are then fed into the "trigger selection module", which allows the selection of 6 trigger masks to work in concurrency to provide a global trigger.

Trigger masks and trigger selection module

Event acquisition for the detector is started only if specific conditions on the masked single-channel triggers are met, these conditions are called "trigger masks".

Three classes of trigger masks are implemented on the board:

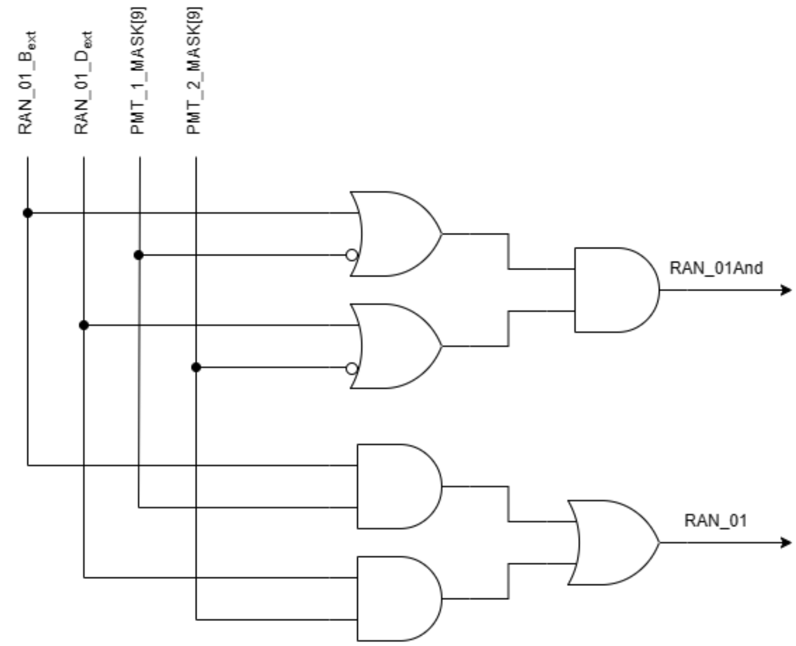

Figure 3.11: PMT mask logic diagram: the RAN_01_B,D$_{ext}$ signals are single-channel triggers, produced by the PMTs coupled with the first calorimeter plane, extended to 100 ns

1. **Event acquisition** masks: designed to validate events produced by particles entering the detector from the main window (the tracker side)
2. **Event monitor** masks: used for efficiency measurements and to provide information about particles not contained inside the calorimeter
3. **GRB detection** masks: implemented for detecting Gamma Ray Bursts in the 2 to 20 MeV energy range

To give a clear description of these masks, the following nomenclature will be used:

- when the name of a scintillator is used, it indicates the OR of the two PMTs connected to it (e.g. $RAN\_x = RAN\_x\_A + RAN\_x\_B$, where "A" and "B" indicates the two PMTs)
- if the name of a plane is followed by "And", it means that the AND of the two PMTs is computed. If the plane is composed of different segments, the ANDs of the segments are put in OR (e.g. $TR1And = (TR1\_1\_A \cdot TR1\_1\_B) + (TR1\_2\_A \cdot TR1\_2\_B) + ... + (TR1\_5\_A \cdot TR1\_5\_B)$)

The following masks belong to the **event acquisition masks**:

$$M_1 = TR1And \tag{3.8}$$

$$M_2 = TR1 \cdot TR2 \tag{3.9}$$

$$M_3 = TR1 \cdot TR2 \cdot RAN\_02 \tag{3.10}$$

These three masks are designed for particles with gradually increasing energies: M_1 will produce a trigger for particles that lose all their energy in the first trigger plane or, at most, inside the tracker. The other two masks allow the detection of particles that reach the TR2 scintillator (M_2) and the RAN_02 slab (M_3).

The **event monitor masks** are defined as follows:

$$M_4 = RAN\_01 \cdot RAN\_07 \cdot RAN\_12 \tag{3.11}$$

$$M_5 = TR2 \cdot BOT \tag{3.12}$$

$$M_6 = BOT \cdot EN1 \cdot EN2 \cdot \overline{TR1 + TR2 + LAT} \tag{3.13}$$

$$\begin{aligned} M_7 = {} & (RAN\_05And + RAN\_06And + RAN\_07And + RAN\_08And) \cdot \\ & (\overline{RAN\_04 + RAN\_09}) \end{aligned} \tag{3.14}$$

Mask 4 is used for efficiency measurements if compared with the event acquisition masks.

Masks 5, 6 and 7 are designed respectively for particles passing through the whole detector and not fully contained, particles entering from the bottom of the detector and particles entering from the sides.

To **detect GRBs** the PMT&T board implements two masks:

$$M_8 = (EN1And + EN2And) \cdot (\overline{RAN\_12 + LAT + BOT}) \tag{3.15}$$

$$\begin{aligned} M_9 = {} & (RAN\_05And + RAN\_06And + RAN\_07And + RAN\_08And) \cdot \\ & (\overline{RAN\_04 + RAN\_09 + LAT}) \end{aligned} \tag{3.16}$$

Mask 8 exploits the high density of the LYSO crystals to detect GRB photons via Compton scattering, mask 9 is designed for photons with very low energies.

Another trigger mask, defined as “generic trigger mask”, can be configured to compute the AND of any scintillator planes:

$$\begin{aligned} M_{generic} = {} & (\Sigma_{i=0}^{20} G[i]) \cdot \\ & [(TR1 + \overline{G[0]}) \cdot (TR2 + \overline{G[1]}) \cdot \\ & (RAN\_01 + \overline{G[2]}) \cdot \ldots \cdot (RAN\_12 + \overline{G[13]}) \cdot \\ & (EN1 + \overline{G[14]}) \cdot (EN2 + \overline{G[15]}) \cdot \\ & (LAT\_01 + \overline{G[16]}) \cdot \ldots \cdot (LAT\_01 + \overline{G[19]}) \cdot (BOT + \overline{G[20]})] \end{aligned} \tag{3.17}$$

	`GENERIC_TRIGGER_MASK` (0x52)																					
Register bit	31–21	20	19	18	17	16	15	14	13	12	11	10	9	8	7	6	5	4	3	2	1	0
Description	Unused	G[20] (BOT)	G[19] (LAT_04)	G[18] (LAT_03)	G[17] (LAT_02)	G[16] (LAT_01)	G[15] (EN2)	G[14] (EN1)	G[13] (RAN_12)	G[12] (RAN_11)	G[11] (RAN_10)	G[10] (RAN_09)	G[9] (RAN_08)	G[8] (RAN_07)	G[7] (RAN_06)	G[6] (RAN_05)	G[5] (RAN_04)	G[4] (RAN_03)	G[3] (RAN_02)	G[2] (RAN_01)	G[1] (TR2)	G[0] (TR1)

Table 3.6: Generic trigger mask register description

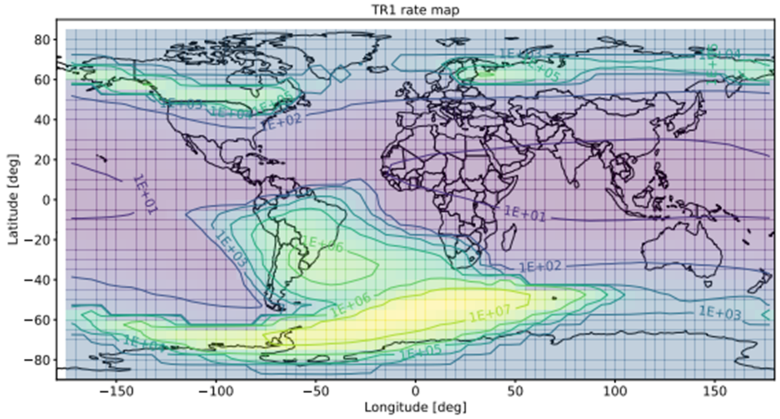

Figure 3.12: Particle rate for low energy particles (courtesy of the CSES-Limadou collaboration)

Where **G** is the vector of bits from `GENERIC_TRIGGER_MASK` register (see table 3.6). The first summation is needed to have $M_{generic} = 0$ when the generic mask is not set ($\mathbf{G} = \mathbf{0}$).

HEPD-02 will be able to select six of these trigger masks to operate in **concurrency** and four of them can be **prescaled** independently. These functionalities represent an innovation for the mission and will increase its scientific significance, allowing the study of different physics cases at the same time by selecting trigger masks that work in parallel.

This solution also prevents the occurrence of situations in which a trigger mask with very high rates can occupy the entire available bandwidth for the different physics channels, as could happen in regions of the orbit such as the poles or the SAA in which the particle rate, especially for low energies, significantly increases up to hundreds of megahertz (see figure 3.12).

To achieve these functionalities, the output of the 10 trigger masks (M_1 to M_9 and $M_{generic}$) are connected to 6 multiplexers producing the six concurrent triggers (T_0 to T_5). Using the `TRIGGER_MASK` register, described in table 3.7, it is possible to select the trigger mask associated with each concurrent trigger.

The selection is made by writing the index of the desired mask in each of the six locations (from bits 23 to 0) of `TRIGGER_MASK` register. To select the generic trigger mask, `0x0A` must be written.

Bits from 26 to 24 are used to enable the external trigger input or to use signals from

TRIGGER_MASK (0x51)										
Register bit	31–27	26	25	24	23–20	19–16	15–12	11–8	7–4	3–0
Description	Unused	Enable external trigger	BOT as veto	LAT as veto	Selected mask for T5	Selected mask for T4	Selected mask for T3 (prescaled)	Selected mask for T2 (prescaled)	Selected mask for T1 (prescaled)	Selected mask for T0 (prescaled)

Table 3.7: Trigger mask register description

PRESC_T3_T2 (0xFD)		
Register bit	31–16	15–0
Description	Prescaling factor for T3	Prescaling factor for T2

Table 3.8: Prescaling factors register for T3 and T2 triggers

the BOT scintillator, LAT scintillators or both to inhibit the trigger.

Prescalers

The first four triggers (T_0 to T_3) are connected to counters which allow to ignore a configurable number of triggers (see figure 3.13), effectively reducing the trigger rate and realizing the prescaling.

The registers `PRESC_T3_T2` and `PRESC_T1_T0` allow to configure the prescaling factors and are described in tables 3.9 and 3.8.

Given the high particle rate in SAA, a 16-bit prescaling factor would not be enough for detector purposes. For this reason, the `PRESC_T1_T0` register is not symmetrical and for the T1 trigger it is possible to select an 18-bit value (and a 14-bit value for T2).

The prescalers' internal operation is described in figure 3.14. The counter is incremented at each trigger signal and the counter output is compared with the prescaling factor reduced by one. When these two values are equal the two AND gates become "transparent" and, as soon as another trigger occurs, the two flip-flops registers it.

This solution allows the production of the prescaled trigger within a single clock cycle, necessary for the FF2 flip-flop to register the signal, and to have the counter cleared the next clock cycle thanks to FF1.

PRESC_T1_T0 (0xFE)		
Register bit	31–18	17–0
Description	Prescaling factor for T1	Prescaling factor for T0

Table 3.9: Prescaling factors register for T1 and T0 triggers

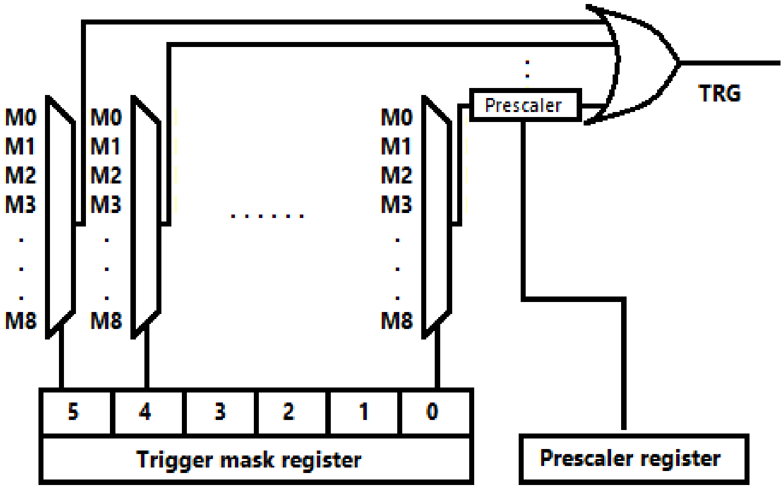

Figure 3.13: Schematic of the prescaled concurent trigger masks

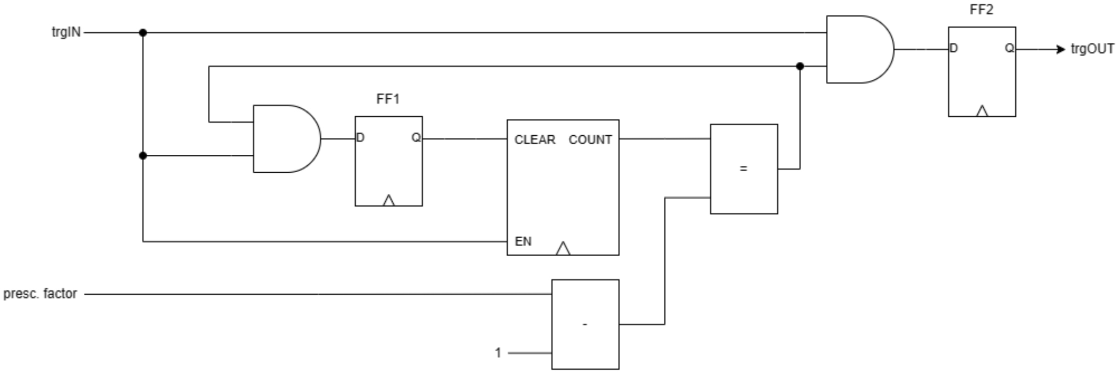

Figure 3.14: Schematic of the prescalers

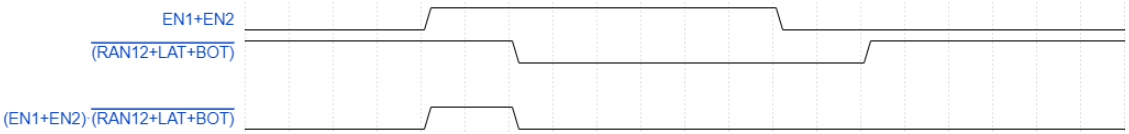

Figure 3.15: Spurious trigger produced by the GRB LYSO mask, caused by the delay between $EN1 + EN2$ and $\overline{(RAN12 + LAT + BOT)}$

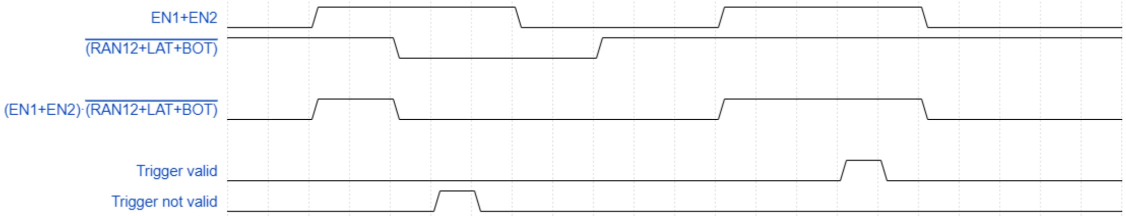

Figure 3.16: The second level trigger samples logic conditions 30 ns after the first trigger, producing “trigger valid” and “trigger not valid” signals

Otherwise, comparing the counted value with the prescaling factor directly, two clock cycles would have been necessary to produce the trigger, being the counter a synchronized element too.

First and second level triggers

The timing of some trigger masks, such as the GRB masks, must take into account that anti-coincidences may cause spurious triggers if signals are spread in time.

To avoid situations like these (depicted in figure 3.15), a second-level trigger system has been developed, to sample signals sometime after the logical condition assertion, assuring that the overlap of signals is long enough to exclude spurious triggers.

In figure 3.16 the operation of the second level trigger is depicted. Two different signals are produced to indicate whether a valid or invalid trigger has been produced.

The CITIROC’s Peak Detection circuit requires to be armed before the peak of the shaper that is set to 50 ns of shaping time.

Given that the “trigger valid” takes 100 ns to be produced, it’s not possible to use it, instead the Peak Detection circuit is armed by the first level trigger and if the “trigger valid” signal is asserted, the FPGA starts the acquisition and the ADC conversion.

If the “trigger not valid” signal is asserted, the CITIROCs analogue memories are cleared and the Peak Detection circuit reset.

The FSM managing the first and second-level triggers is described in figure 3.17. It starts in the `idle` state and goes into the `waitNClks` state, when any of the six concurrent triggers is asserted (condition expressed by the `mskTrg` signal) or when the external trigger input is pulsed (the `extTrg` signal).

In the `waitNClks` state the FSM waits for 3 clock cycles and then goes into the `checkMasks` state where the six concurrent triggers are sampled again. If all of them are equal to `‘0’`, the FSM reaches the `trgInvalid` state and the “trigger not valid” signal

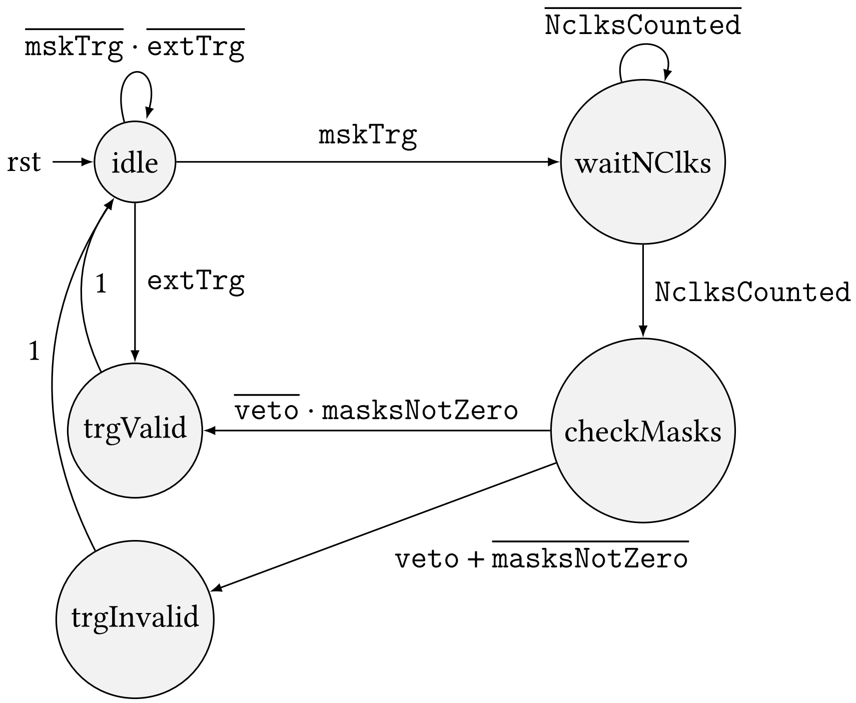

Figure 3.17: Second-level trigger FSM diagram

is produced, otherwise it goes into the `trgValid` state and the "trigger valid" signal is produced.

Global trigger

The global trigger is the signal sent to the DPCU and TDAQ to start data acquisition. The FSM producing it is described by the diagram shown in figure 3.18.

The transition between the `idle` state and `trg` state is conditioned by the signal `sendTrg`, defined by the expression:

$$\texttt{sendTrg} = \overline{\texttt{trgInhibit}} \cdot (\texttt{debugTrg} + \texttt{calib} \cdot \overline{\texttt{validTrg}} + \texttt{acq} \cdot \texttt{validTrg}) \tag{3.18}$$

The `trgInhibit` signal is, the result of the following boolean condition:

$$\texttt{trgInhibit} = \overline{\texttt{DPCU\_TRGHOLD}} + \overline{\texttt{DPCU\_BUSY}} + \texttt{FIFO\_AFULL} + \texttt{TRG\_BUSY} \tag{3.19}$$

The `DPCU_TRGHOLD` and `DPCU_BUSY` are active-low signals, coming from the DPCU board, and are used to stop the acquisition when the DPCU is reading the PMT&T SpaceWire registers or when its internal buffer is full. The `FIFO_AFULL` signal is produced by the PMT&T internal FIFO when there is room for one packet only. Finally the `TRG_BUSY` signal is produced during the writing of data in the FIFO.

The terms in parenthesis of equation 3.18 come from the following sources:

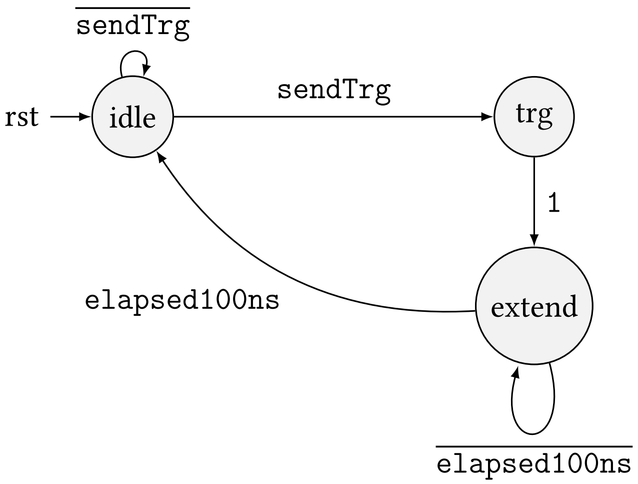

Figure 3.18: Global trigger FSM diagram

- `debugTrg` is produced by an edge detector connected to bit 6 of `CMD_REG` register. It allows the production of a fake trigger via SpaceWire commands for debug purposes

- `calib` is a signal produced by a configurable counter which allows the production of fake triggers used for calibrating PMTs. The period of fake triggers can be configured using bits from 31 to 15 of `CMD_REG` register (5 µs/LSB), and the calibration state can be controlled using bits 11 and 12

- `acq` indicates if the board is in the acquisition state or not and can be controlled by bits 9 and 10 of `CMD_REG` register.

- `validTrg` is produced by the second-level trigger logic

When the `sendTrg` signal is asserted the FSM goes into the `trg` state for a single clock cycle and produces the trigger signal. Then it reaches the `extend` state that lasts 100 ns and avoids repeated triggers that could be caused by the extended width of single-channel triggers.

After the `extend` state, the FSM returns to `idle` state.

3.4 Digitization of PMT signals

When the “trigger valid” signal is produced, the readout from CITIROC starts. Two FSMs are designed for this purpose: one controls the CITIROCs analogue output and another manages the ADC conversion.

The first FSM is described in figure 3.19: the “trigger valid” signal causes the transition to the “hold” state where the HOLD signal is produced (the same already described in section 3.2.1).

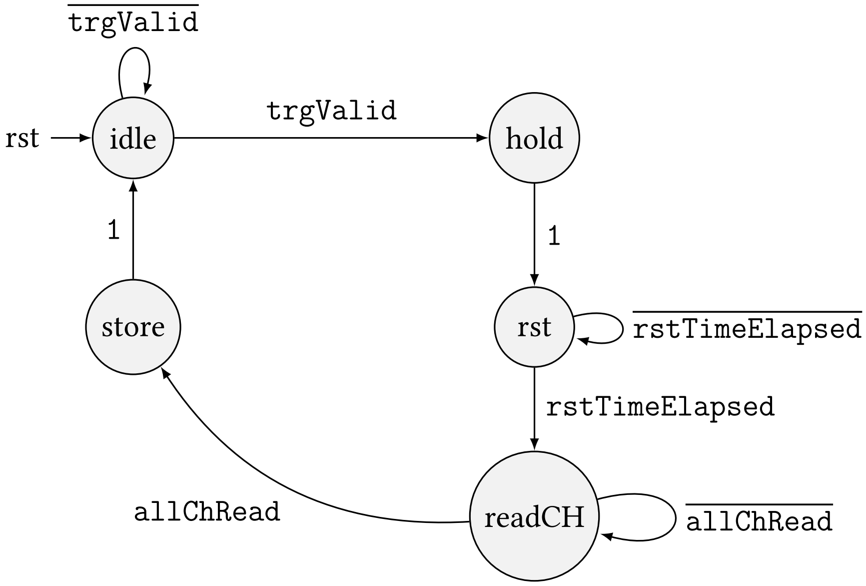

Figure 3.19: Diagram describing the FSM designed to read the CITIROCs analogue output

Then the FSM goes in the "rst" state for 80 ns, to ensure that CITIROC's internal registers are cleared, and after that the sequential readout of the channels starts enabling a SCLK signal with a frequency of 200 kHz.

When all the channels are converted by the ADCs, the values are stored in an internal memory.

The ADC conversion is managed by the FSM described by the diagram in figure 3.20, which sequentially reads the 14 bits from the ADCs and signals the end of the conversion to the CITIROCs analogue readout FSM.

3.5 Rate meters and counters

The PMT&T board implements three classes of rate meters:

- **PMT rate meters**, used to check the correct functioning of each PMT
- **Mask rate meters**, designed to measure the particle rate of all the 10 trigger masks, even those that are not selected for triggering
- **GRB rate meters**, specifically designed for the GRB detection algorithm

A large part of the detector's data analysis is based on particle rate. As already shown in section 1.2, important results such as the detection of GRBs have been made by studying trigger mask rates.

The "PMT rate meters" are 64 counters that reset every second, allowing the measurement of the rate of single-channel triggers with a resolution of 1 Hz. These rate meters are 16-bit wide and can measure a maximum frequency of $\sim$ 65.5 kHz.

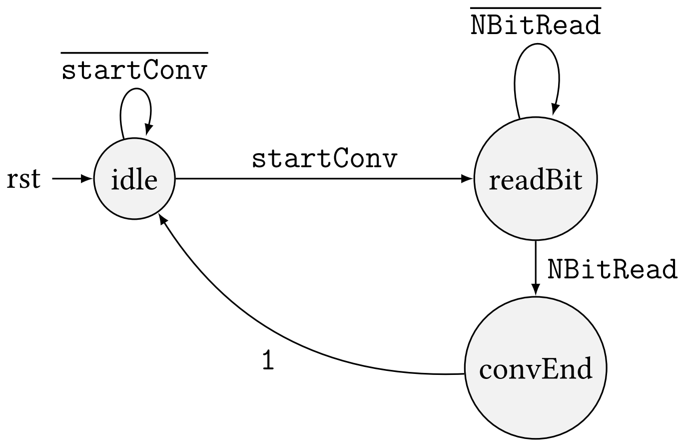

Figure 3.20: Diagram describing the FSM for ADC readout

The “Mask rate meters” are implemented differently depending on the trigger mask, but all have a resolution of 1 Hz: the M_0 mask, which is supposed to have the highest rate, is a 32-bit counter for a maximum frequency of $\sim$ 4294 MHz, all other masks are implemented with 16-bit counters reaching $\sim$ 65.5 kHz.

The “GRB rate meters” are two additional rate meters that measure the frequency of the M_8 and M_9 masks. These counters are 16-bit wide and reset every 5 ms, corresponding to a frequency resolution of 200 Hz and a maximum frequency of $\sim$ 13.1 MHz. The GRB detection algorithm, described in section 3.7, is based on them.

Various counters are also implemented to obtain information on the acquisition: a 32-bit counter, enabled by the global trigger signal, counts the number of events from the last reset and is named “trigger counter”.

Two 32-bit counters are designed to measure the alive and dead time of the detector with a resolution of 5 µs: the alive time counter is enabled by the $\overline{\texttt{BUSY}}$ internal signal while the dead time counter is enabled by `BUSY`.

The valid triggers that happen during the dead time are counted by a dedicated 16-bit counter.

Five additional 16-bit counters, enabled by signals from the T1 segments, count the particles that pass through a specific turret of the direction detector.

3.6 SpaceWire communication

The PMT readout and trigger board communicates with the DPCU and TDAQ boards using a register-based SpaceWire protocol.

The figure 3.21 describes this protocol:

1. When a **trigger** occurs, the data produced by the trigger board are **stored in a FIFO**. The trigger signal is also sent to the TDAQ to start its acquisition

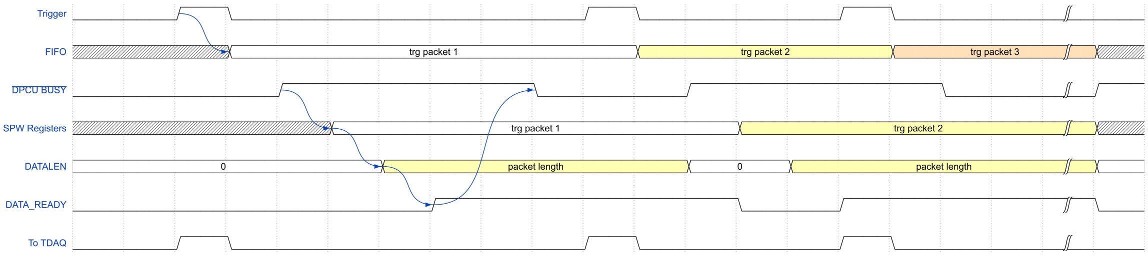

Figure 3.21: Timing diagram describing boards interwork

Name	Length (bytes)	Description
Header	2	Indicates the beginning of the packet
Trigger counter	4	Number of events acquired
Timestamp	4	Time from the power-on (16 µs resolution)
Trigger ID	1	Identification number for the trigger configuration
ADC data	192	ADC conversion of the two CITIROC's output
Lost trigger	2	Triggers counted during dead time
Alive time	4	Alive time counter (5 µs resolution)
Dead time	4	Dead time counter (5 µs resolution)
Trigger flags	8	Flags indicating over-the-threshold channels
Turret flags	1	Flags indicating which tracker turret has been hit
Turret counters	20	Signals counted for each turret
Trailer	2	Indicates the end of the packet
Total	244	

Table 3.10: Data packet description

2. If the **BUSY** signal from the DPCU is **not asserted**, the first packet in the FIFO is written in a series of **SpaceWire registers**
3. The **total length** of the data itself is stored in a separate register
4. A **DATA_READY** signal is asserted by the trigger board
5. When the DATA_READY is asserted, the DPCU **reads the DATALEN** register and starts the reading of all the data registers

3.6.1 Scientific data

For each trigger generated, 244 bytes of data are produced (see table 3.10).

The data contains:

- **Trigger counter**: the total number of triggers produced
- **Timestamp**: a 16 µs resolution timestamp

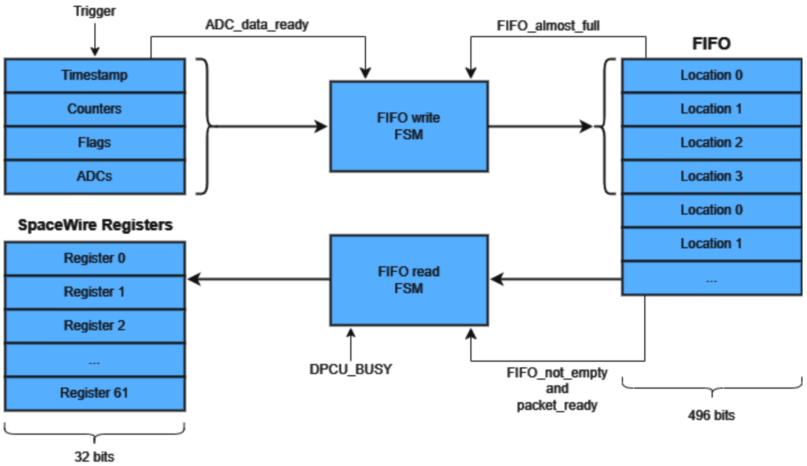

Figure 3.22: Data packet finite state machines

- **The trigger ID**: an identification number indicating which of the 6 concurrent trigger masks produced the event trigger
- **ADC data**: the ADC conversions of the 64 channels for both the High Gain and Low Gain preamplifiers
- **Lost trigger**: the number of triggers counted during dead time
- **Alive and Dead time**: counters for alive and dead time of the detector (5 µs resolution)
- **Trigger and turret flags**: Flags indicating which channels and tracker's turrets are over the threshold
- **Turret counters**: counters for each tracker's turret

Alive and dead time counters can be used to obtain the acquisition frequency of the detector. The prescalers' tests described in section 4.7 are an example of this and use the relation $\nu = 1/(T_{live} + T_{dead})$ to check that the trigger rate was correctly scaled. In HEPD-01 they were also used to obtain particle flux, as described in [20].

The data packet is stored in a 62×40 bytes FIFO, which can account for 10 packets.

Two independent Finite State Machines (FSM) are designed to pack the data in 4 locations of the FIFO and to unpack them into 62 SpaceWire registers (see figure 3.22).

3.7 GRB detection algorithm

The algorithm for GRB detection has been developed by the analysis team of the collaboration and it's implemented on the DPCU board [39].

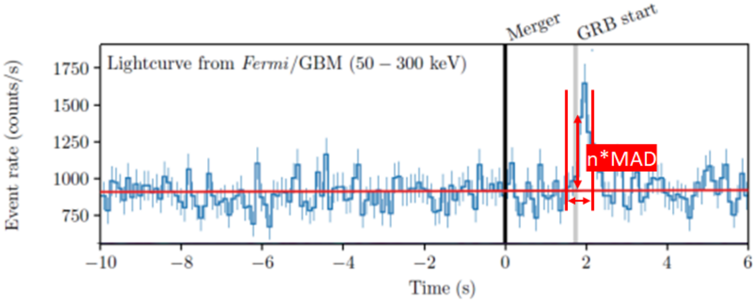

Figure 3.23: GRB detection algorithm [38]

It is based on the counts of GRB rate meters from which the following values are calculated:

- the moving average (**MAV**) in 10 s, obtained by the equation

$$MAV_j = \frac{1}{N}\sum_{i=j-N}^{j-1} x_i$$

  where 'j' is an index over data

- the mean absolute difference (**MAD**), obtained by

$$MAD_j = \frac{1}{N}\sum_{i=j-N}^{j-1} |x_i - MAV_j|$$

- the rate in 10 ms (**SUM01**)
- the sum of rates in 40 ms (**SUM04**)
- the sum of rates in 160 ms (**SUM16**)
- the sum of rates in 360 ms (**SUM36**)

Using these quantities, the **GRB trigger condition** is defined as:

$$\begin{aligned} TRIGGER \; = & (MAV < SAT\_THR) \cdot \\ & [(SUM01 - MAV > TH01 \cdot MAD) + \\ & (SUM04 - 4 \cdot MAV > TH04 \cdot 2 \cdot MAD) + \\ & (SUM16 - 16 \cdot MAV > TH16 \cdot 4 \cdot MAD) + \\ & (SUM36 - 36 \cdot MAV > TH36 \cdot 6 \cdot MAD)] \end{aligned} \tag{3.20}$$

where SAT_THR is a value used to avoid triggers given by counters saturation and TH04, TH16 and TH36 are threshold values depending on the specific GRB masks.

When the GRB trigger condition occurs, and only if the satellite is outside of the SAA or the poles, the DPCU stores the rate meter values of the last 10 s.

If the GRB trigger condition returns to the baseline and then rises again before a configurable T_{cool} time, the acquisition is extended.

4

Measurements and tests on the PMT&T board

The PMT&T board has been completely characterized to define operative parameters that will optimize the acquisition of signals produced by HEPD-02 scintillators and additional measurements were taken to verify the compatibility of the board with the satellite power requirements.

The characterization included:

- Power consumption measurements, which ensure the compliance of the board with the assigned power budget
- Optimization of the input signal conditioning circuit, to select the proper resistors for the input attenuators
- Calibration of the CITIROC's preamplifiers and shapers, which will allow the management of CITIROC's parameters during the flight
- Peak detector time window calibration, for obtaining information on the acquisition timing
- Signal-to-noise ratio measurements
- Threshold calibration, which gives the relation between the threshold DAC value for CITIROCs and the input signal

For these measurements, Python scripts have been developed to automatize the configuration of the board, the data acquisition and analysis.

This chapter is dedicated to the description and the discussion of all the characterization tests.

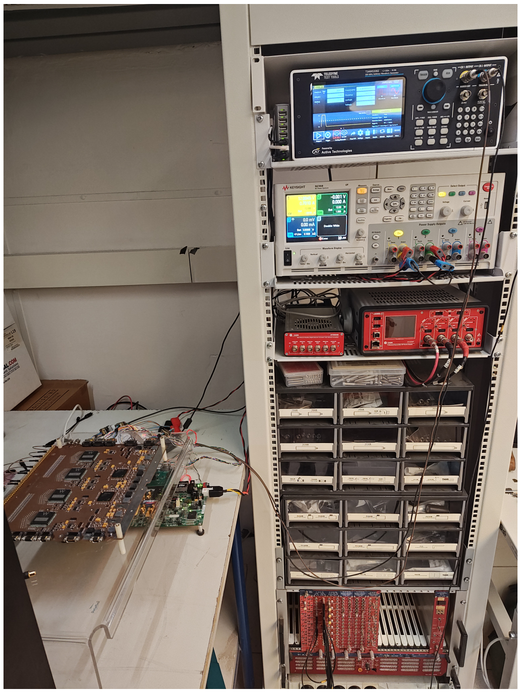

(a) The experimental setup used for the power consumption measurements: the instrument at the top of the rack is the pulse generator, followed by the power analyzer. At the bottom, the NIM crate hosts the linear fan-in/fan-out. On the left, it is possible to see the PMT&T board and, below, the DPCU emulator

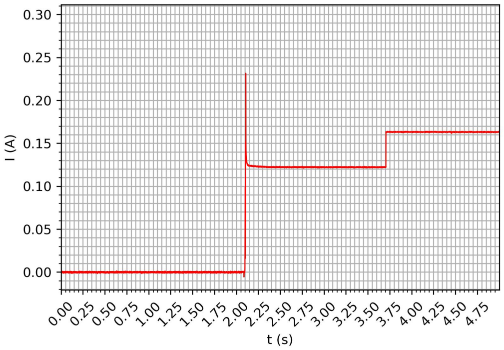

(b) Consumption during the first 5 seconds from the power up

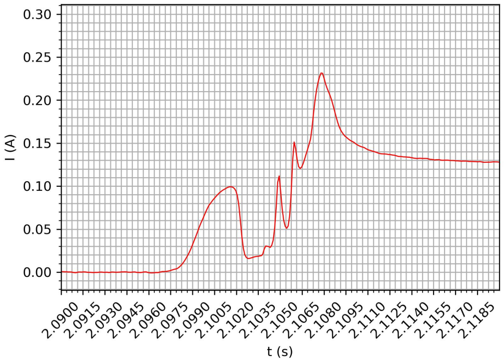

(c) Detail of the absorption peak

Figure 4.1: Experimental setup and startup power consumption

4.1 Power consumption

The power consumption of the board may vary based on the number of CITIROC's channels that produce triggers and on their frequency. In any case, the consumption of the board must not exceed the maximum power of 4 W assigned to the PMT&T subsystem, to avoid power failures that could affect the whole detector.

For this measurement, a Keysight N6705B [40] power analyzer has been used and a Teledyne T3AWG3352 [41] waveform generator produced the pulses for the board.

The experimental setup used is shown in figure 4.1a, since the pulse generator has only 2 outputs, a linear fan-in/fan-out (CAEN N401 [42]) allowed increasing the number of pulsed channels. The measurement lasted 90 s and included the power-up of the board and the two CITIROCs, the configuration of the working parameters and a 30 s signal acquisition.

4.1.1 Startup sequence

In figure 4.1b the power consumption at the power on of the board is shown.

During the first 1.6 s (approximately) from the power on, the watchdog circuit present

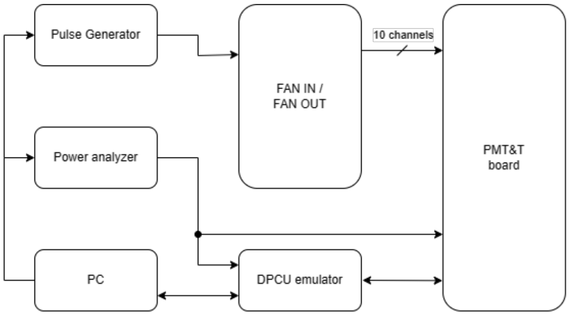

Figure 4.2: Schematic description of the experimental setup used for power measurements

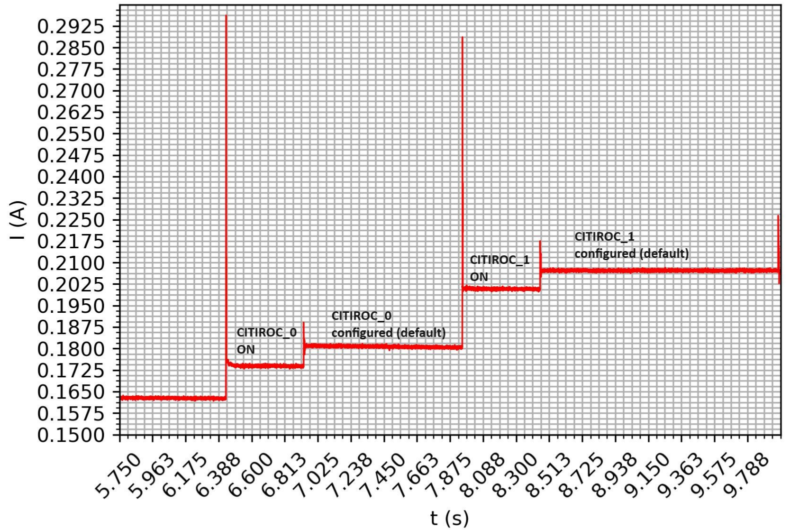

Figure 4.3: CITIROCs power-on sequence

on the board[1] keeps the reset signal asserted and the current absorption is of 120 mA with a peak of 230 mA that lasts about 20 ms.

This peak is caused by the inrush current due to the first charging of all the capacitors on the board. After this, the reset is deasserted and the consumption rises to 160 mA (see figure 4.1b and 4.1c).

When the startup sequence is over, the two CITIROCs are powered on. This is shown in figure 4.3 where the CITIROC's inrush current peaks are visible.

After each CITIROC has been powered on, a first configuration with safe default values starts and after that, the current consumption rises by about 7 mA.

The final current absorption is approximately of 210 mA which corresponds to a power consumption of 2.5 W.

---

[1] The board mounts an ADM8316WDZ30 [43] by Analog Devices. The second 'D' in the serial number means that the reset active timeout period is of 1600 ms (typical values), compatible with the measured duration.

N_{ch}	I (mA)	σ_I (mA)
2	219.1	0.5
4	222.3	0.4
6	222.7	0.5
8	223.6	0.5
10	224.4	0.5

Table 4.1: Power consumption of the PMT&T board at different number of pulsed channels

4.1.2 Multiple channel consumption

A first test has been made using from 2 to 10 channels of the board and stimulating them with square signals of 10 ns and 3 V with a frequency of 8 MHz.

The $T1 \cdot T2$ trigger mask was used and it has been prescaled to 8000 to simulate the worst-case situation of a very high particle rate that triggers various channels of the CITIROCs, requiring limiting the detector trigger rate.

Figure 4.4 depicts the current absorption of the board when a different number of channels (N_{ch}) are stimulated. The first rise in the current corresponds to the enabling of the pulse generator output that produces the CITIROC's single channel triggers. The second increment is related to the start of the acquisition that produces the global trigger.

The peak around 80 s corresponds to the configuration of the CITIROCs' parameters, which happens just before the start acquisition and after enabling the pulse generator. The small variations after the last step are due to the transfer of data and signals between the PMT&T and the DPCU boards.

The values of the current absorption are reported in table 4.1.

It is possible to fit these values to obtain the relationship between the current absorption and the number of pulsed channels:

$$I(N_{ch}) = 0.6 \cdot N_{ch} + 219 \quad \text{(mA)} \tag{4.1}$$

This expression brings to a maximum current absorption (when 64 channels are producing single-channel trigger signals) of 260 mA that corresponds to the maximum power consumption of 3.12 W, still within the design limits.

Considering that the board is powered by 12 V and that the absorbption increment, in plots 4.4, is caused only by CITIROCs, it is possible to obtain a power consumption per channel of $0.6\,\text{mA/ch} \cdot 12\,\text{V} = 7.2\,\text{mW/ch}$, compatibly with the consumption declared on the CITIROC's datasheet.

4.2 Optimization of the input signal conditioning circuit

The signals produced by PMTs can reach $\sim\ 6 \div 8\,\text{V}$, while the CITIROCs' inputs are limited by internal protection diodes. A series of measurements were performed to find

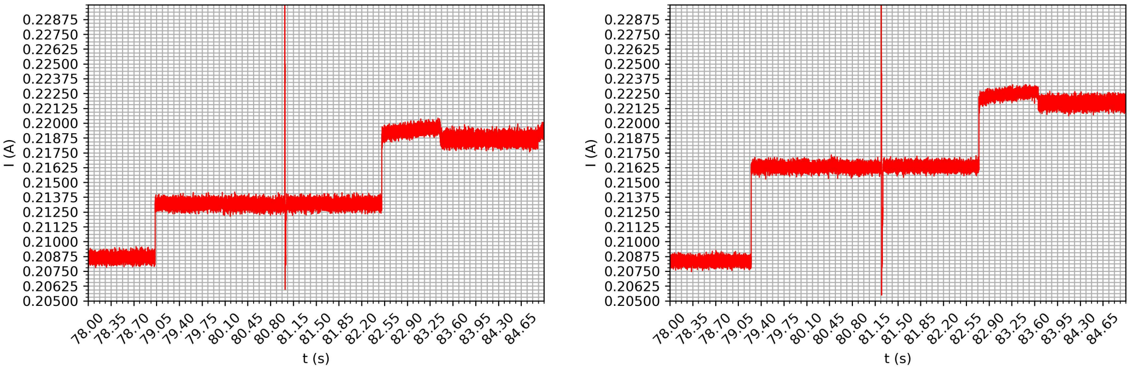

(a) N_{ch} = 2 **(b)** N_{ch} = 4

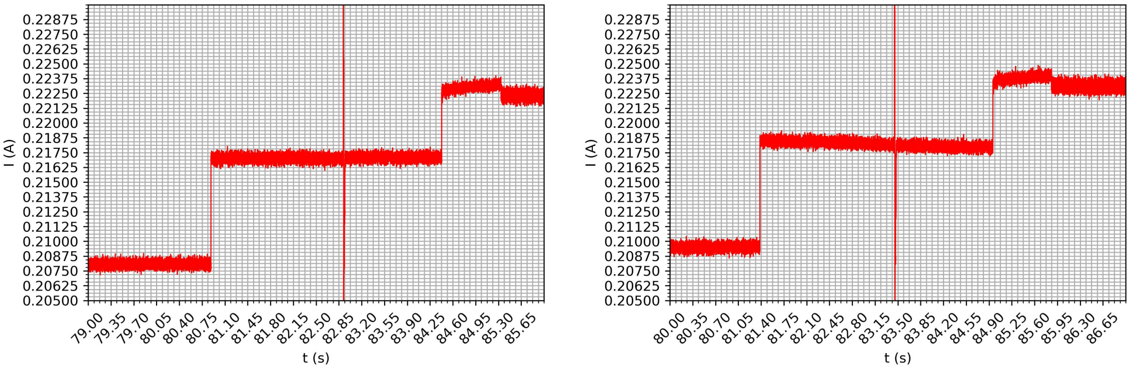

(c) N_{ch} = 6 **(d)** N_{ch} = 8

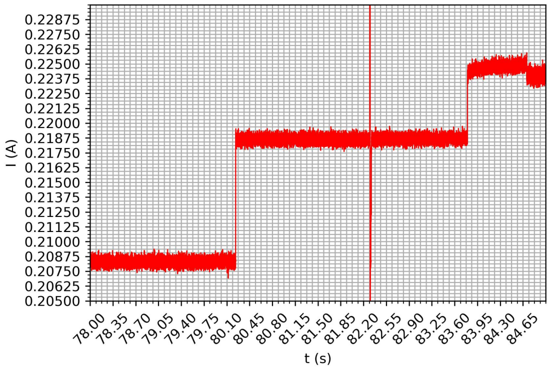

(e) N_{ch} = 10

Figure 4.4: Power consumption of the PMT&T board at different number of pulsed channels

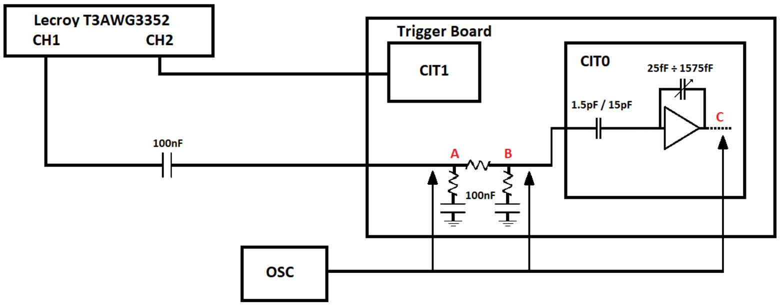

Figure 4.5: Scheme of the experimental setup used for input attenuators' optimization

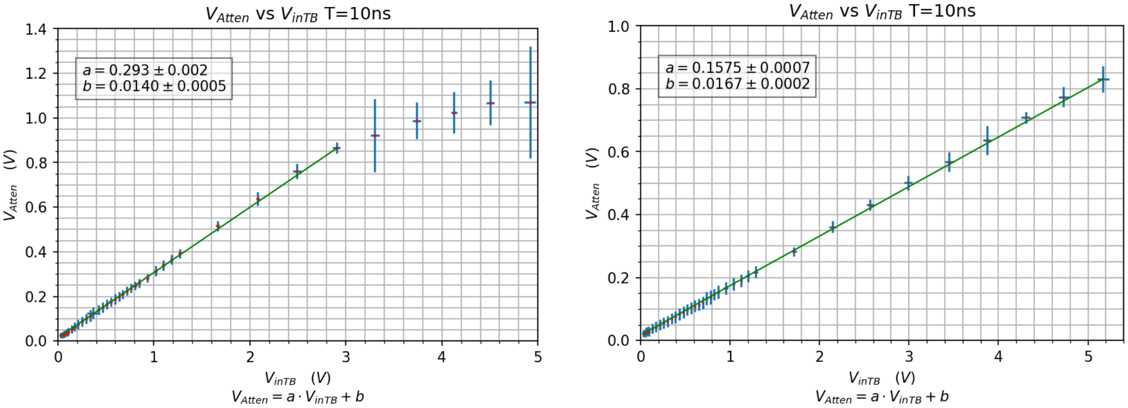

(a) Output of the 3x attenuator (V_{Atten}) vs the amplitude of the signal injected in the board channel (V_{inTB})

(b) Output of the 6x attenuator (V_{Atten}) vs the amplitude of the signal injected in the board channel (V_{inTB})

Figure 4.6: Attenuated signals vs input signals curves

the minimum value of the input signal attenuation that ensures a good input dynamic range for the CITIROCs.

Since changing the attenuation requires soldering work on the board, the tests have been conducted on the engineering model of the PMT&T board first, and then the results of these measurements have been used to realize the qualification and flight models.

The experimental setup used for these measurements is schematized in figure 4.5

For this test, two channels with attenuations of 3 and 6 were used and were connected to a pulse generator producing pulses with different amplitudes and a duration of 10 ns.

Using an oscilloscope (a Keysight DSO9254A [44][45]) three points along the PMT acquisition chain were probed: the input of the attenuation circuit (point 'A' in figure 4.5) and the output (point 'B').

In figure 4.6a it is possible to see that, with a 3x attenuation, a compression for signals greater than 3 V is present. This compression is caused by the protection diode inside the CITIROC's inputs and would reduce the available input dynamic range, given the extension of PMTs' signals. The channel with the 6x attenuation, instead, shows good linearity over the input amplitude range.

From these considerations a good value for the attenuators would be 6x, but from the calibration curves that will be presented in section 4.3.1, it has been observed that doubling the attenuation and using higher gains for the preamplifiers, allows the CITIROCs to work in a more linear region.

For these reasons, the final values of the attenuations have been chosen considering an attenuation of 12x for signals produced by almost all the scintillators except for those of T1. These scintillators, being thinner than all the others, produce smaller signals that would be wiped by the 12x attenuation and therefore the value 6x is used instead.

Table 4.2 shows the attenuation values for all the PMT&T channels.

4.3 Calibration of the CITIROC's preamplifiers and shapers

This section will describe the measurements made to characterize the CITIROCs' preamplifiers and to select suitable gains for in-flight operation.

All the acquisitions have been made by injecting a charge in the PMT&T channels, equivalent to that produced by the PMTs coupled with the different scintillators.

Given their different characteristics, the signals were divided into three categories:

- T1-like signals, that are produced by the thin segments of T1 and have a small duration ($FWHM \sim 5$ ns)
- CALO-like signals, produced by all the other plastic scintillators, with $FWHM \sim 10$ ns
- LYSO-like signals, typical of LYSO crystals and have the longest duration ($FWHM \sim 50$ ns)

4.3.1 Preamplifiers calibration

Using the same setup described in figure 4.5, the output of the CITIROC's preamplifier (point 'C') has been characterized.

Figure 4.7 shows the High Gain (HG) and Low Gain (LG) preamplifiers' output ($V_{paHG/LG}$), as a function of the attenuated signal amplitude (V_{Atten}), using the lowest amplification factor (9.75 for the HG and 0.975 for the LG).

From a linear fit, it can be seen that the amplification differs from the nominal values, obtained by the ratio between the input capacity of the preamplifier and the feedback capacity. In the HG preamplifier, the saturation starts at $V_{Atten} = 120$ mV while the LG retains its linearity. For low voltage values, the curves of both the HG and LG are not linear for the signals used in these tests.

A series of measurements has been made varying the gain of the preamplifiers and using square pulses as input signals. The duration of these pulses has been chosen considering the FWHM of the typical signal produced by the PMTs for different types of scintillators: 5 ns for T1 scintillators, 10 ns for the calorimeter and 50 ns for the LYSO crystals.

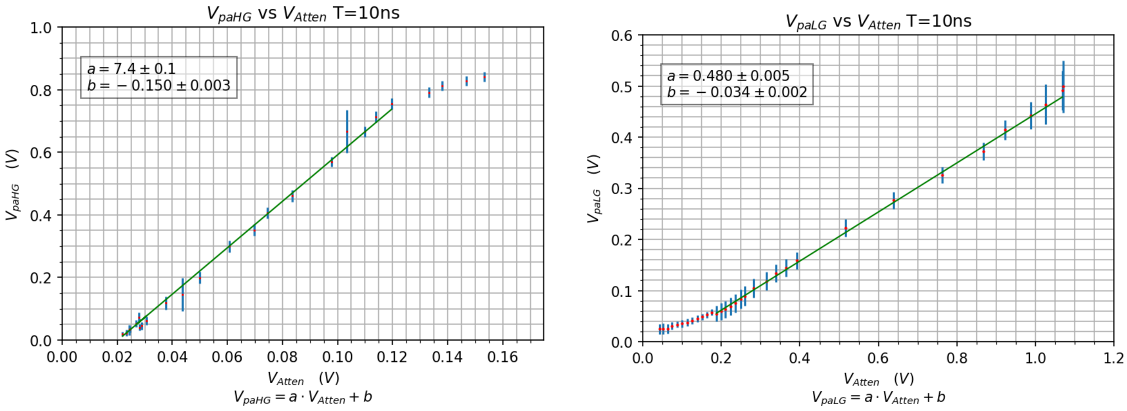

(a) Output of the High Gain preamplifier vs the attenuator output signal

(b) Output of the Low Gain preamplifier vs the attenuator output signal

Figure 4.7: Output of High and Low Gain preamplifiers using the lowest amplifications (HG=9.75 and LG=0.975)

Board channels	Scintillators	Attenuation	HG	LG
0 - 4, 32 - 36	T1	6	20	2
5 - 20, 27 - 31, 37 - 52, 59 - 63	T2, RAN BOT, LAT	12	20	2
21 - 26, 53 - 58	EN	12	10	1.5

Table 4.2: Gains and attenuation factors for PMT readout and trigger board

The shaping time was set to 50 ns and, for the channels related to T1 and the calorimeter scintillators, an amplification of 75 for the High Gain and 7.5 for LG was used. For the LYSO channels, lower gains were chosen (10 for HG and 1.5 for LG) given the larger width of these signals.

From these measurements, it can be observed that the CITIROCs work very well for signals with a duration higher than 10 ns. The final results of this work are shown in figure 4.8, where the ADC counts versus the signal amplitude is plotted.

After the detector integration, crosstalk between channels was observed with particles producing high-amplitude signals in a large number of scintillators. This effect was not present in laboratory measurement on the board and led to a change in the selected gain for the T1 and calorimeter preamplifiers.

The final values for preamplifiers' gains are shown in table 4.2 and the related calibration curves are shown in figure 4.9.

4.3.2 Slow Shapers calibration

The experimental setup used to calibrate the CITIROC's slow shapers is shown in figure 4.10. The first channel of the pulse generator has been connected to the "External trigger"

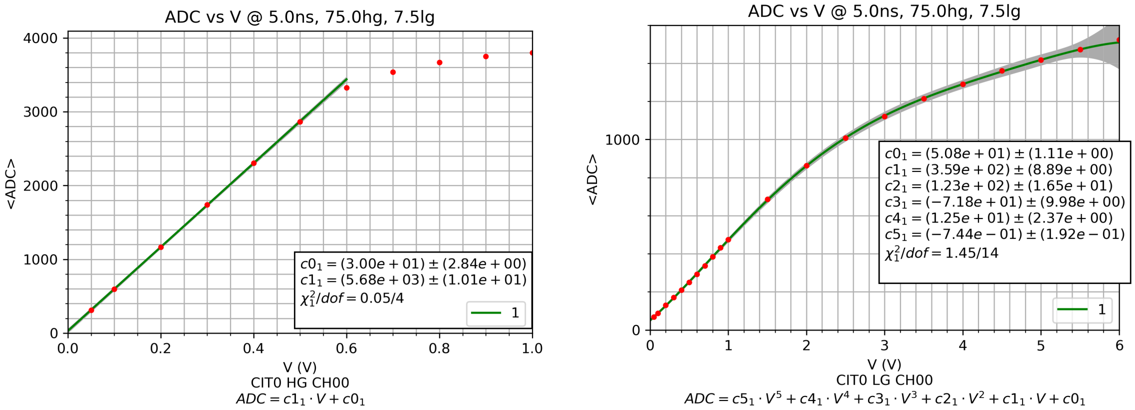

(a) ADC vs V for T1-like signals (High Gain = 75)

(b) ADC vs V for T1-like signals (Low Gain = 7.5)

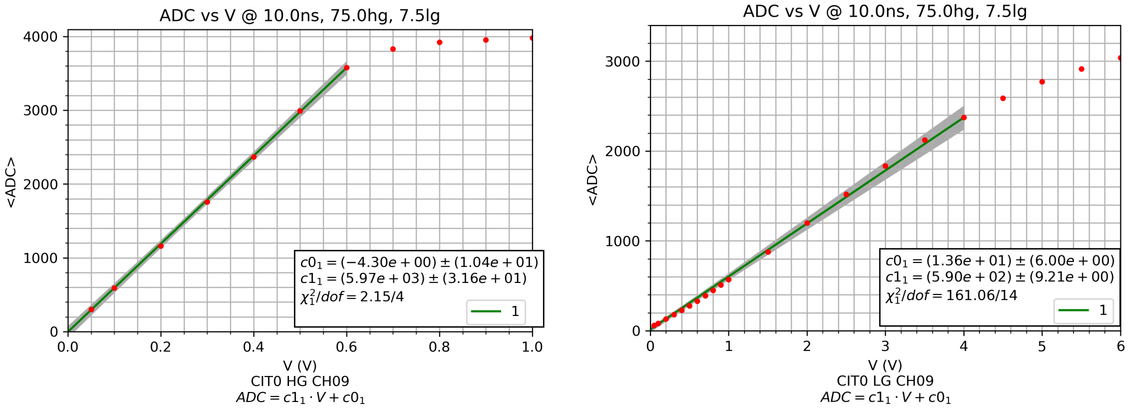

(c) ADC vs V for CALO-like signals (High Gain = 75)

(d) ADC vs V for CALO-like signals (Low Gain = 7.5)

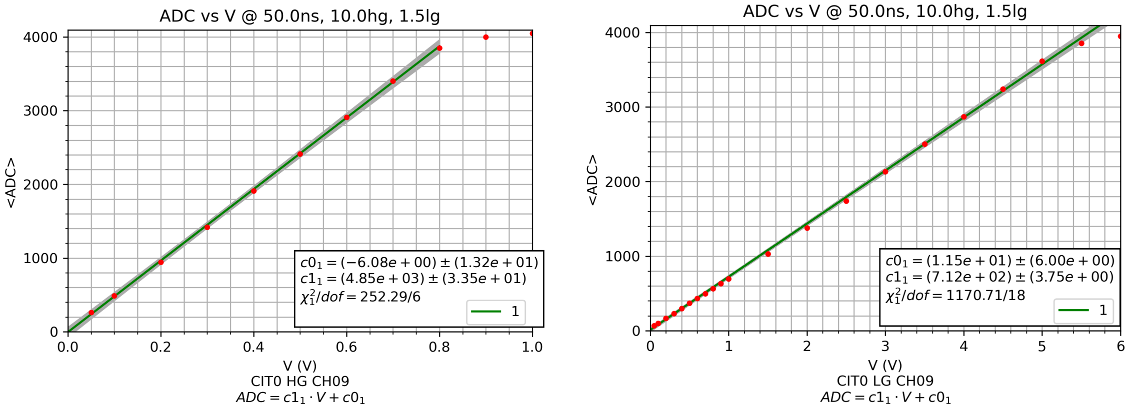

(e) ADC vs V for LYSO-like signals (High Gain = 10)

(f) ADC vs V for LYSO-like signals (Low Gain = 1.5)

Figure 4.8: ADC counts vs input signal's amplitude

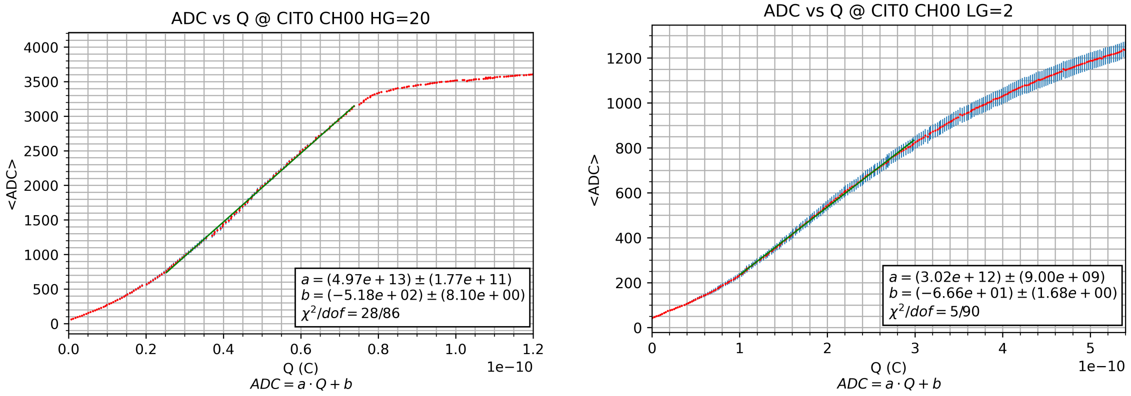

(a) ADC vs V for T1-like signals (High Gain = 20)

(b) ADC vs V for T1-like signals (Low Gain = 2)

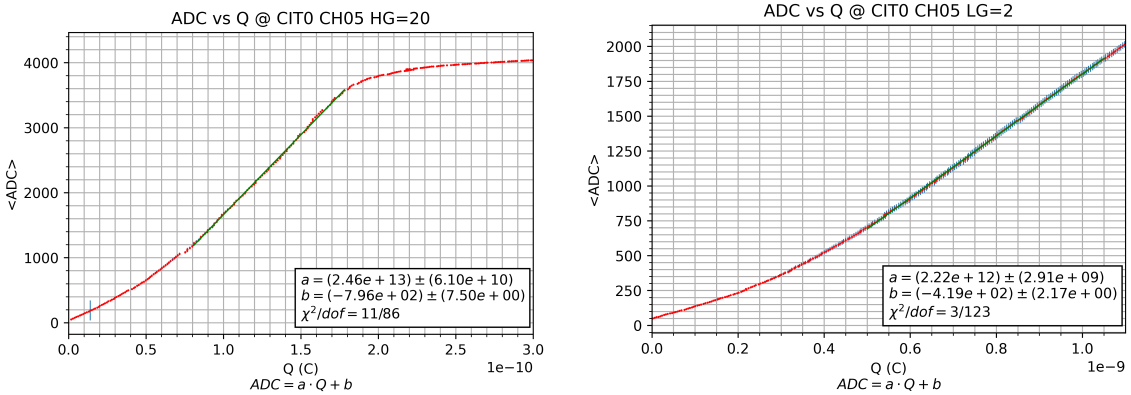

(c) ADC vs V for CALO-like signals (High Gain = 20)

(d) ADC vs V for CALO-like signals (Low Gain = 2)

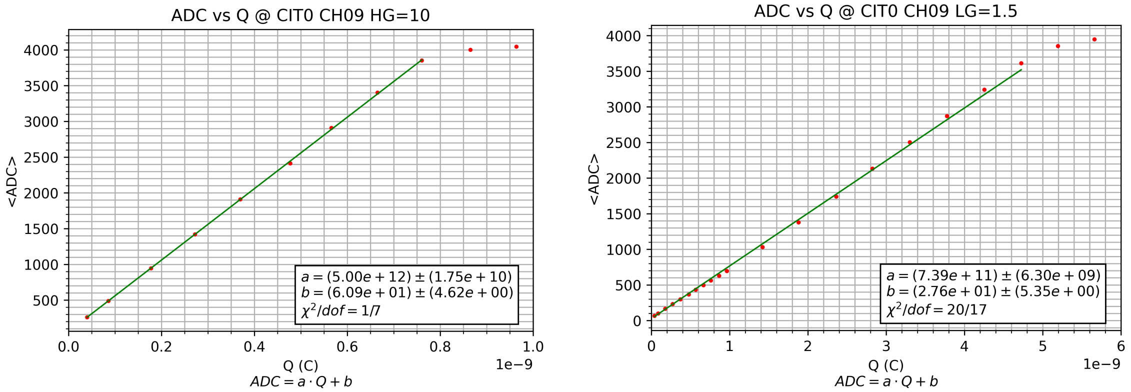

(e) ADC vs V for LYSO-like signals (High Gain = 10)

(f) ADC vs V for LYSO-like signals (Low Gain = 1.5)

Figure 4.9: ADC counts vs input signal's charge

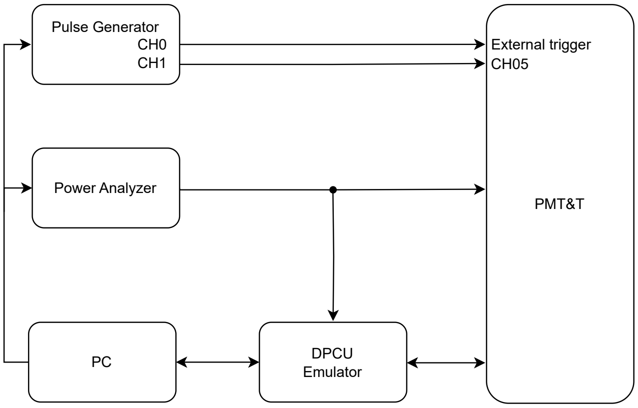

Figure 4.10: Experimental setup used for slow shapers calibration

$T_{nominal}$ (ns)	T_{extr} (ns)	
	HG	LG
25	30	30
50	50	65
62.5	60	75
87.5	80	90

Table 4.3: Nominal and extrapolated shaping times

input of the board and the second channel to CH05 (with attenuation equal to 12).

The same measurement has been repeated for different preamplifiers' gains but, in this section, only the plots obtained with the previously selected gains of 20 for HG and 2 for LG will be reported.

Square signals of 50 mV were used, with increasing duration (T) and different values for the shaping time (T_{shap}). This way it was possible to study the shaper's behaviour when the width of an input signal approaches the selected T_{shap}.

In figures 4.11 and 4.12 the ADC vs T plots are shown for T_{shap} equal to 25 ns, 50 ns, 62 ns and 87 ns.

These plots show that the shapers work linearly until the widths of the input signals are comparable with the shaping time.

Figures 4.13 and 4.14 show the relative differences between the ADC distribution's MPVs and the values predicted from the linear regression. Considering signal widths that ensure residuals below 5%, it is possible to see that the extrapolated values are close to the nominal ones.

A shaping time of 50 ns was chosen as the default configuration during the normal detector operation. With this shaping time, calibration curves at different gains have been obtained and are shown in figure 4.15.

From these plots, it is possible to see that the preamplifiers' behaviour is not linear

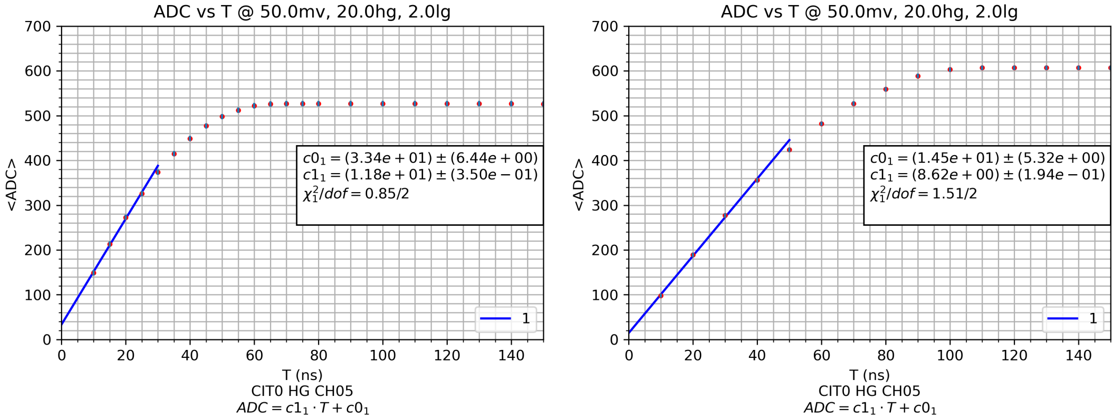

(a) Shaping time = 25 ns

(b) Shaping time = 50 ns

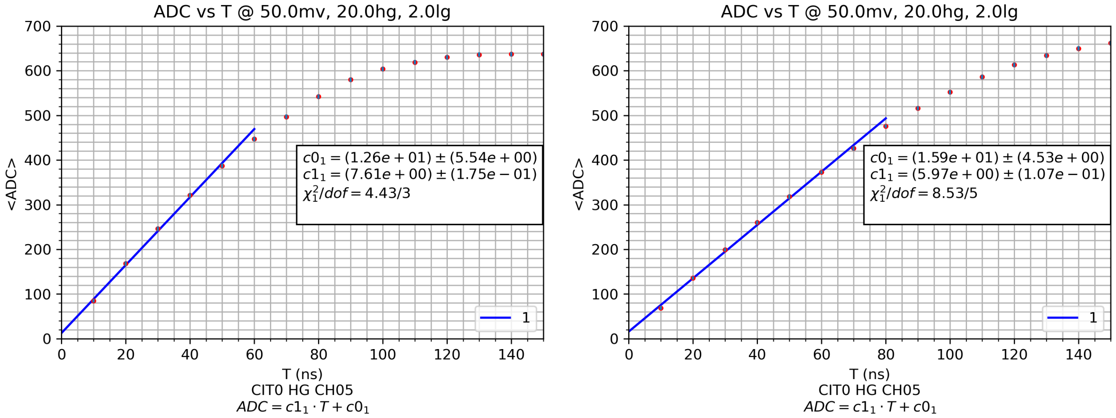

(c) Shaping time = 62 ns

(d) Shaping time = 87 ns

Figure 4.11: High Gain shapers calibration

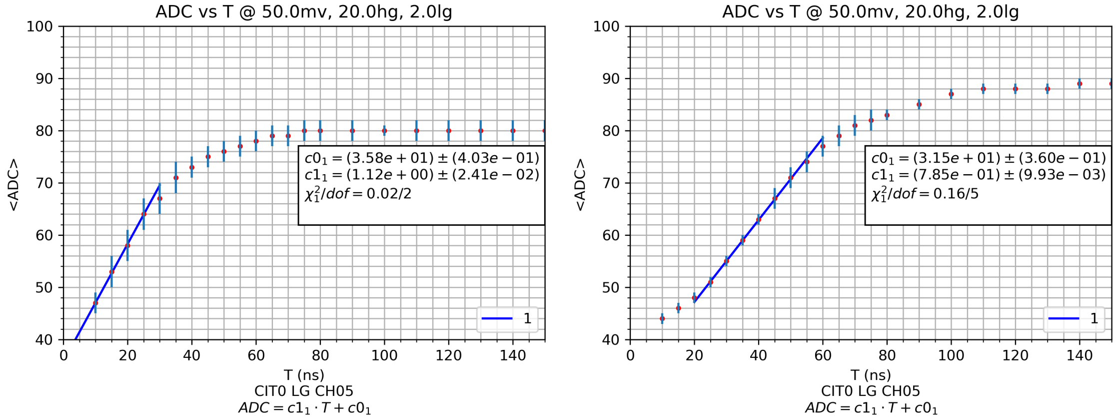

(a) Shaping time = 25 ns

(b) Shaping time = 50 ns

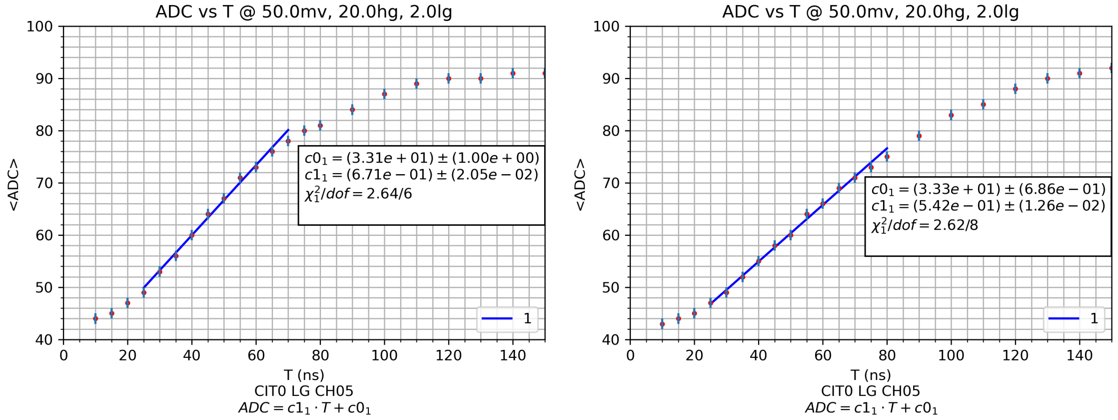

(c) Shaping time = 62 ns

(d) Shaping time = 87 ns

Figure 4.12: Low Gain shapers calibration

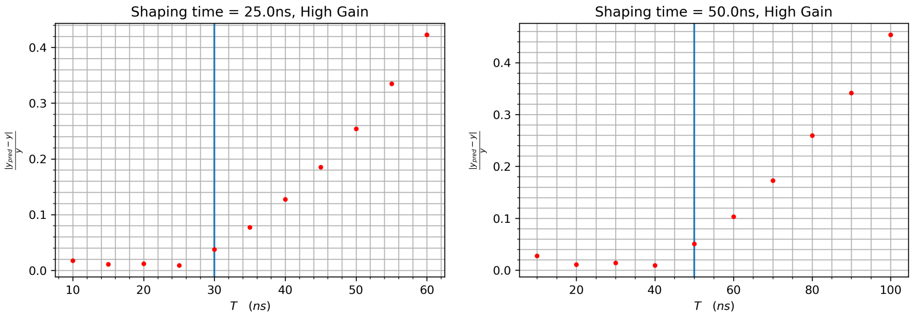

(a) Shaping time = 25 ns

(b) Shaping time = 50 ns

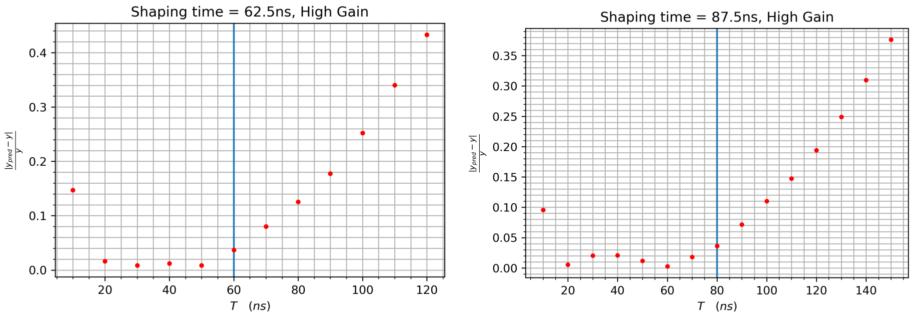

(c) Shaping time = 62 ns

(d) Shaping time = 87 ns

Figure 4.13: High Gain shapers relative residuals

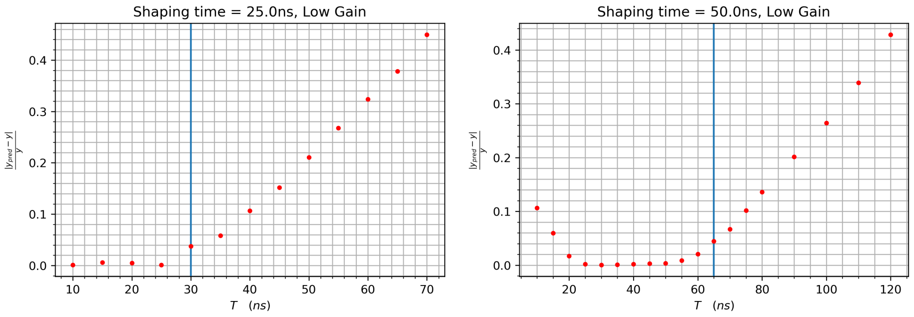

(a) Shaping time = 25 ns

(b) Shaping time = 50 ns

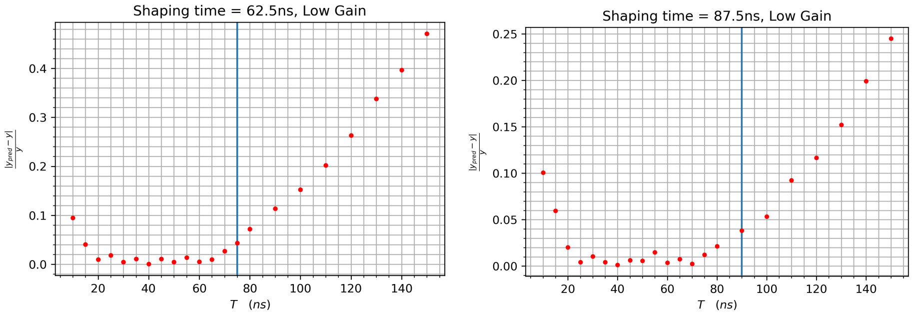

(c) Shaping time = 62 ns

(d) Shaping time = 87 ns

Figure 4.14: Low Gain shapers relative residuals

through the range of the gain values. This can be attributed to differences in the nominal capacitance and the actual one.

These calibration curves will allow to change the parameters of the CITIROCs during the flight, according to the data collected in the commissioning phase

4.4 Peak detection time window

Using the peak detection circuit provided by CITIROCs, it will be possible to correctly sample the peaks of the shapers' signal even when they are spread in time, which happens for HEPD-02 due to the different scintillators' timing characteristics.

This sampling mode requires the use of a HOLD signal that disconnects the analogue memory circuit from the output of the slow shaper and allows it to be stored in a capacitor. The functioning of the peak detector circuit has been described in section 3.2.1 and its scheme is shown in figure 3.6.

The HOLD signal must be delayed to allow the correct functioning of the peak detector and also to ensure that all the scintillators' signals can be sampled when a trigger occurs. This delay is produced through a flip-flops chain that produces 160 ns of delay.

To this delay, 40 ns must be added for the trigger signal to be produced, 10 ns to be expanded and other 10 ns to produce the HOLD signal, since it came from a synchronous finite state machine. This brings to a time window of 220 ns during which the peak detector memorizes the slow shaper peak.

To validate this time window, the same experimental setup of the slow shaper calibration (figure 4.10) was used, with pulses of 200 mV, a duration of 10 ns, a frequency of 20 Hz and adding a delay between the PMT&T external trigger input and the CH05 channel.

Figure 4.16 shows the ADC counts as a function of the delay between the external trigger signal and the CH05 signal. It is possible to see that the ADC counts stay constant up to $\Delta T = 220$ ns and then decrease. The decrease is caused by the slow shaper signal gradually exiting from the peak detector window.

For negative ΔT (i.e. when the signal on CH05 anticipates the external trigger signal), ADC counts below the pedestal can be observed. This effect can be attributed to the undershoot of the slow shaper signal[2], which causes a slight discharge of the analogue memory capacitor. If a second signal is sampled during this undershoot, its peak value could be underestimated.

From this consideration, it is possible to observe that two consecutive signals, on the same channel of the board, can be considered independent if they are delayed at least by 500 ns.

---

[2] CITIROC's slow shapers are CR-RC^2 filters without any pole-zero cancellation circuit. This leads to output signals with an undershoot when the inputs are exponentially decaying signals [46][47]

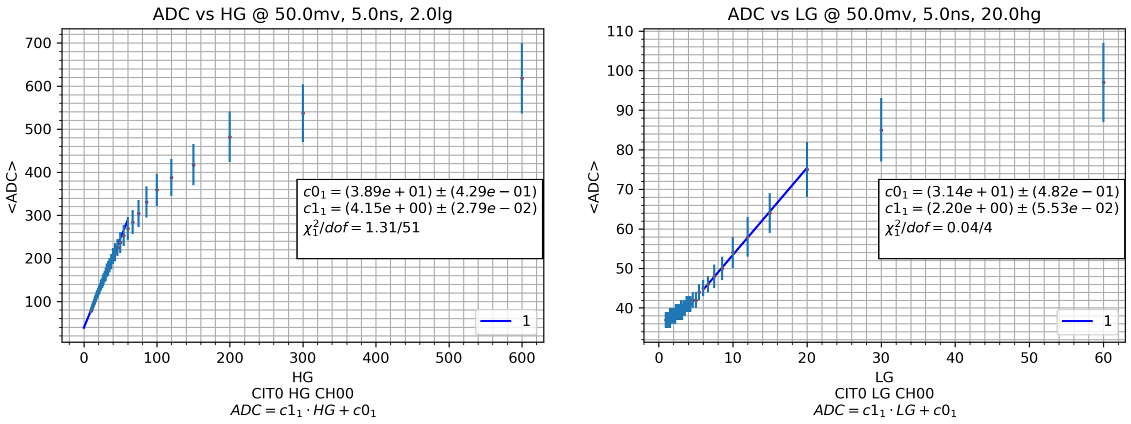

(a) T1-like signals, High Gain

(b) T1-like signals, Low Gain

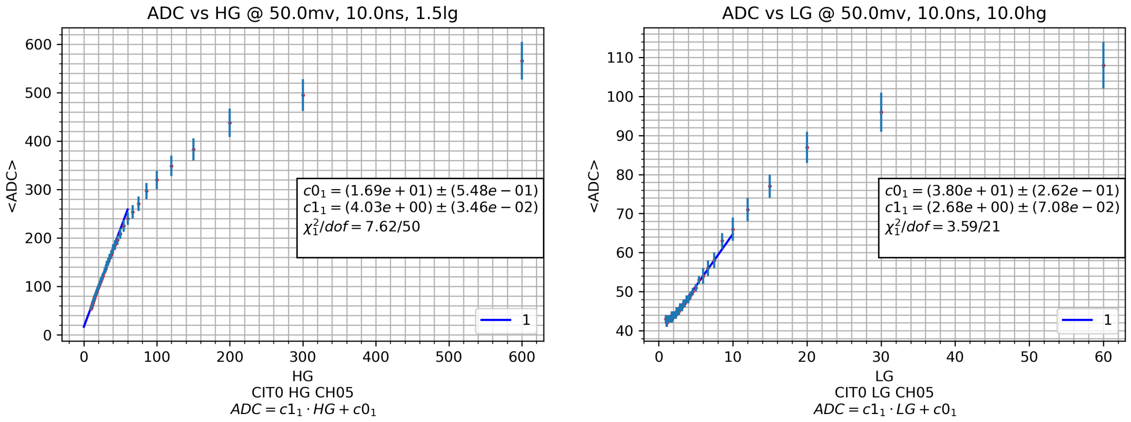

(c) CALO-like signals, High Gain

(d) CALO-like signals, Low Gain

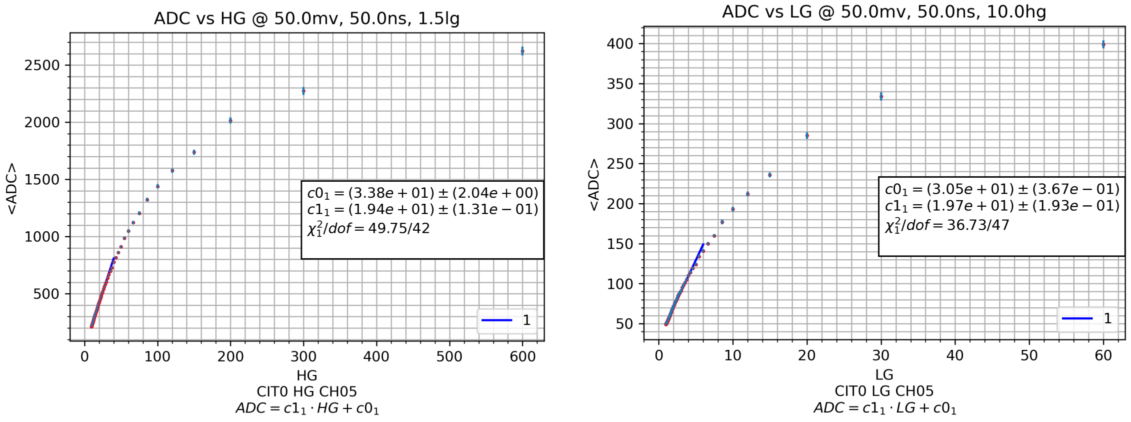

(e) LYSO-like signals, High Gain

(f) LYSO-like signals, Low Gain

Figure 4.15: Preamplifiers gain calibration curves

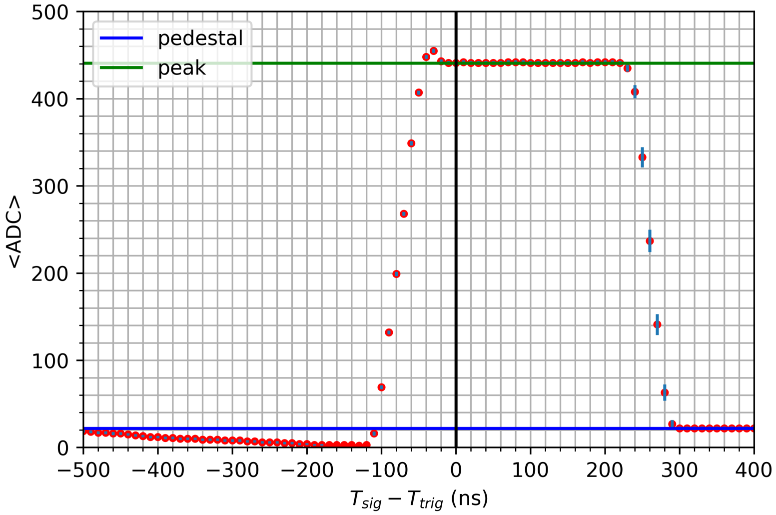

Figure 4.16: Validation of the peak detection time window

Scintillator	FWHM (ns)	MPV		3 percentile			
		MIP	MIP/3	MIP		MIP/3	
		V (mV)	V (mV)	V (mV)	SNR	V (mV)	SNR
T1	5	88	29	51	14.5 ± 0.4	17	1.9 ± 0.1
Calorimeter	10	120	40	81	30.9 ± 0.4	27	7.5 ± 0.1
LYSO	50	216	72	114	167 ± 5	38	51 ± 1

Table 4.4: Scintillator's typical MIP and MIP/3 signals with measured SNR

4.5 Signal to noise ratio measurements

Once the gain and shaping time had been chosen, thanks to the previous set of measurements, the characterization of the board response was completed by measuring the signal-to-noise ratio.

For this measurement, the distribution of signals produced by cosmic muons on different scintillators has been considered. In table 4.4 the amplitude of MIP and 1/3 MIP is reported and also the values of the 3 percentile of the distributions.

Using the setup in figure 4.10, the external trigger was pulsed at twice the frequency of channels CH00 and CH05 (with attenuation 6 and 12 respectively). These channels were pulsed with signals whose amplitudes corresponded to the 3% of the distribution for 1/3 MIP.

In figure 4.17 the ADC counts distribution is shown for the three types of signals and in table 4.4 the SNR, obtained with the expression 4.2, are reported.

$$SNR = \frac{\mu_{sig} - \mu_{pdst}}{\sigma_{pdst}} \tag{4.2}$$

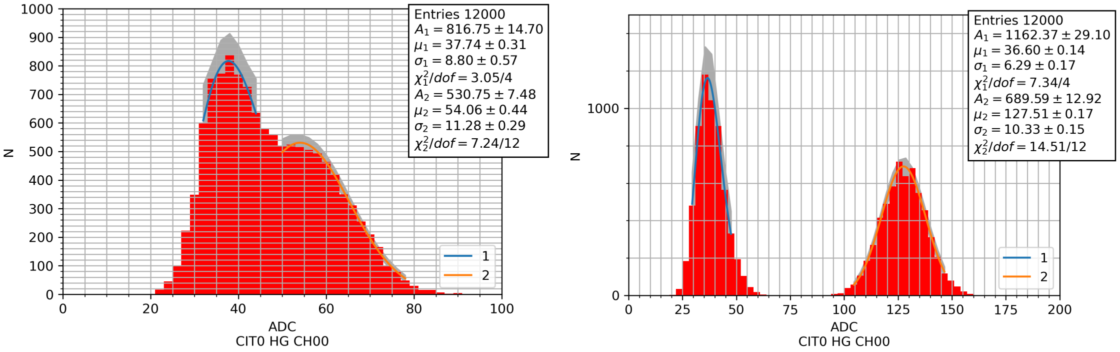

(a) T1-like signals: 1/3 MIP HG = 20, Attenuation = 6

(b) T1-like signals: 1 MIP HG = 20, Attenuation = 6

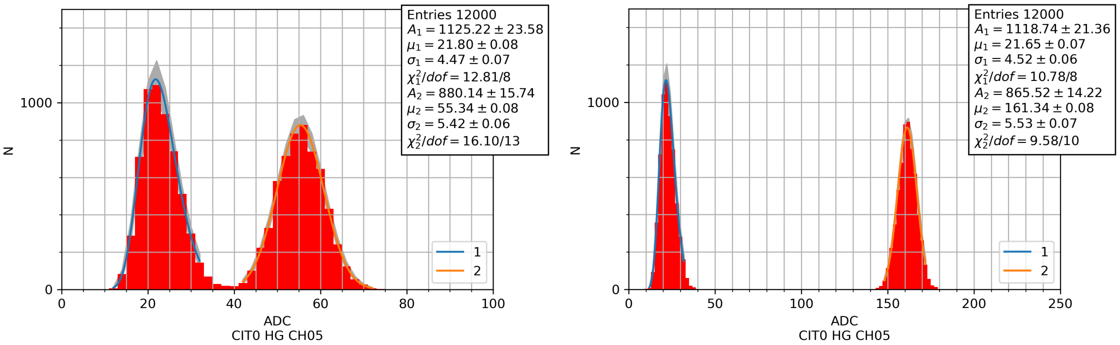

(c) CALO-like signals: 1/3 MIP HG = 20, Attenuation = 12

(d) CALO-like signals: 1 MIP HG = 20, Attenuation = 12

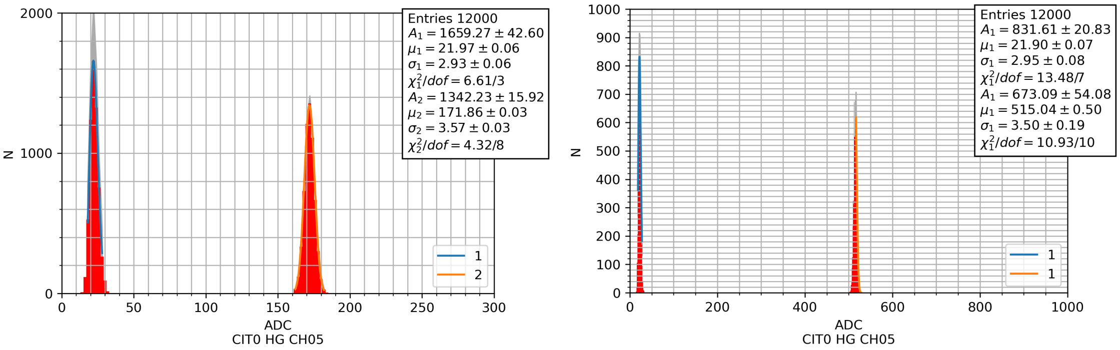

(e) LYSO-like signals: 1/3 MIP HG = 10, Attenuation = 12

(f) LYSO-like signals: 1 MIP HG = 10, Attenuation = 12

Figure 4.17: Distributions for 3 percentile of signals equivalent to 1/3 MIP and 1 MIP

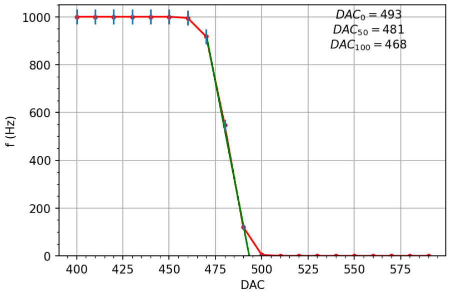

Figure 4.18: S-curve acquired with a signal of 40 mV, 50 ns at 1 kHz

4.6 Threshold calibration

As already mentioned in section 3.2, the single-channel triggers are produced by a discriminator with a configurable threshold that must be selected considering that the three classes of signals (from T1, the calorimeter and the LYSO crystals) undergo different attenuations and amplifications: a threshold optimal for T1 could be too high for LYSO signals.

A threshold scan was performed at different amplitudes of the input signal to find a match between the threshold value and the minimum signal that produces a trigger. This allows obtaining a calibration curve that can guide the selection of the threshold during flight.

Figure 4.18 shows an example of an S-curve obtained using pulses of 40 mV and 50 ns and a frequency of 1 kHz and increasing the threshold's DAC value. As can be seen from the plot, the trigger efficiency decreases with the increase of the DAC value set on the CITIROC's discriminator.

Repeating this measurement for the three different types of signals (T1-like, calorimeter-like and LYSO-like) and different amplitudes, the plots in figure 4.19a, 4.19b and 4.19c have been obtained, using the DAC values that reduce the trigger efficiency to 50%.

4.7 Prescalers test

The introduction of prescaled triggers added complexity to the trigger logic and a dedicated series of measurements was conducted to ensure the correct functioning of the PMT&T board after the implementation of this functionality.

To test the prescalers, square pulses with fixed frequency were used and the board was configured with various prescaling factors to ensure that the output trigger frequency was correctly reduced.

After this first test, a series of measurements with frequencies in the order of MHz were made to obtain the maximum frequency that can be prescaled. To evaluate the output

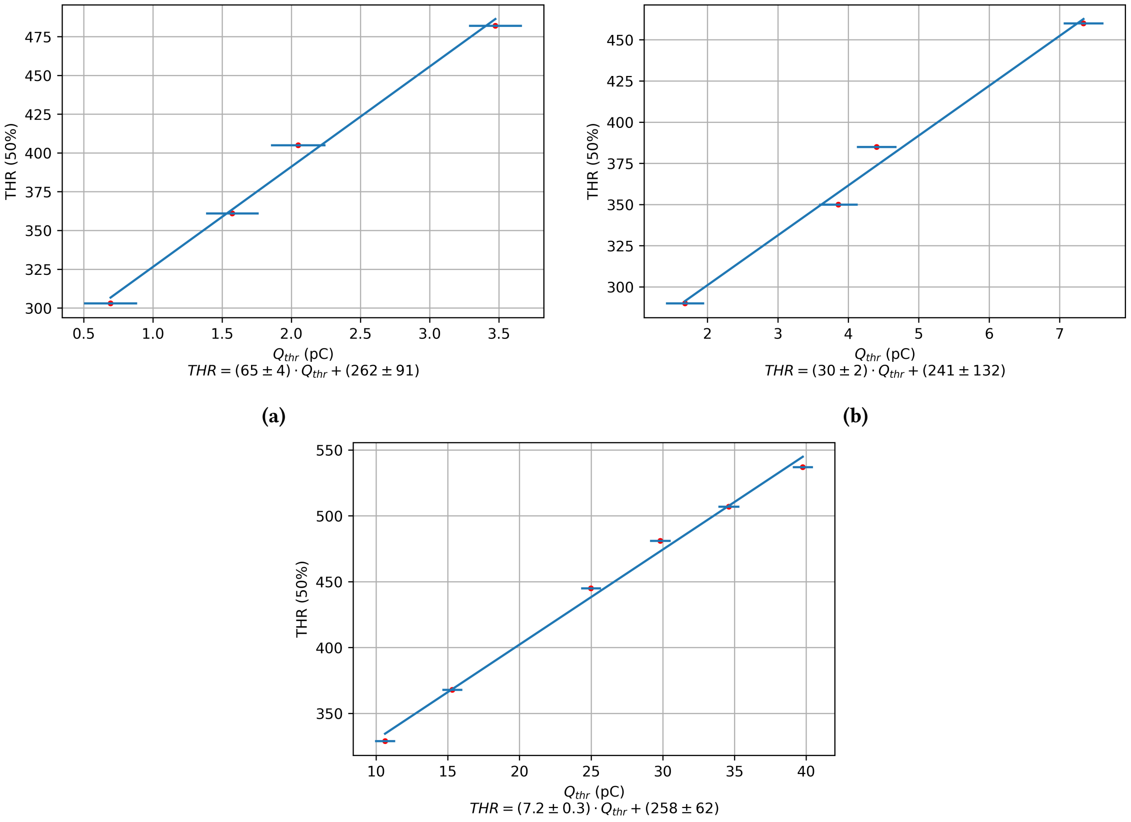

(a)

(b)

(c)

Figure 4.19: Threshold DAC values (THR) as a function of the input charge (Q_{thr}): (a) for T1-like signals, (b) for CALO-like signals (c) for LYSO-like signals

Prescaling factor ($\times 10^3$)	ν_{pulse} (MHz)	$\nu_{expected}$ (kHz)	$\nu_{measured}$ (kHz)
2	2	1	1
10	5	0.5	0.5
20	5	0.25	0.25
50	5	0.1	0.1
40	8	0.2	0.2
80	8	0.1	0.1
20	9	0.45	0.297
90	9	0.1	0.663
5	10	2	0.992
10	10	1	0.5
20	10	0.5	0.25

Table 4.5: Output trigger frequencies measured during the prescalers test

trigger frequency (ν) the alive and dead counters have been used, using the relation:

$$\nu = \frac{1}{T_{live} + T_{dead}} \tag{4.3}$$

Results of these tests are reported in table 4.5 that shows how, for pulse frequencies of 9 MHz, the prescaler begins to lose some pulses (and to reduce the output trigger frequency) and for 10 MHz the output frequency is half that expected.

This behaviour is not caused by a limitation of the prescaler modules but it is compatible with the operation of the FSM that produces the global trigger which takes 100 ns to produce the “trigger valid” signal, losing the additional pulses arriving during this period.

4.8 Boards integration and first acquisitions

After the development of the firmware, a campaign of interwork tests was conducted to check the correct operation of the boards and the communication between them.

This activity took place at Tor Vergata University, lasted about six months and involved me, the TDAQ team from the University of Trento and the company that developed the DPCU board (N.E.A.T. Srl).

At first, simple communication tests between the DPCU and the two other boards were made, ensuring that the SpaceWire protocol worked as expected.

Then the external trigger input of the PMT&T board was stimulated with a pulse generator to produce data and trigger signals and the data integrity after the transfer to the DPCU and the overall performances in terms of dead time of the system were checked.

In these conditions, the dead time was 200 µs and included the memorization of ADC counts in the PMT&T’s FIFO, the transfer of data to the DPCU and the acquisition of TDAQ data.

This work led to the integration of the boards with the calorimeter and the first acquisitions of cosmic muons using the $M_2 = TR1 \cdot TR2$ trigger mask.

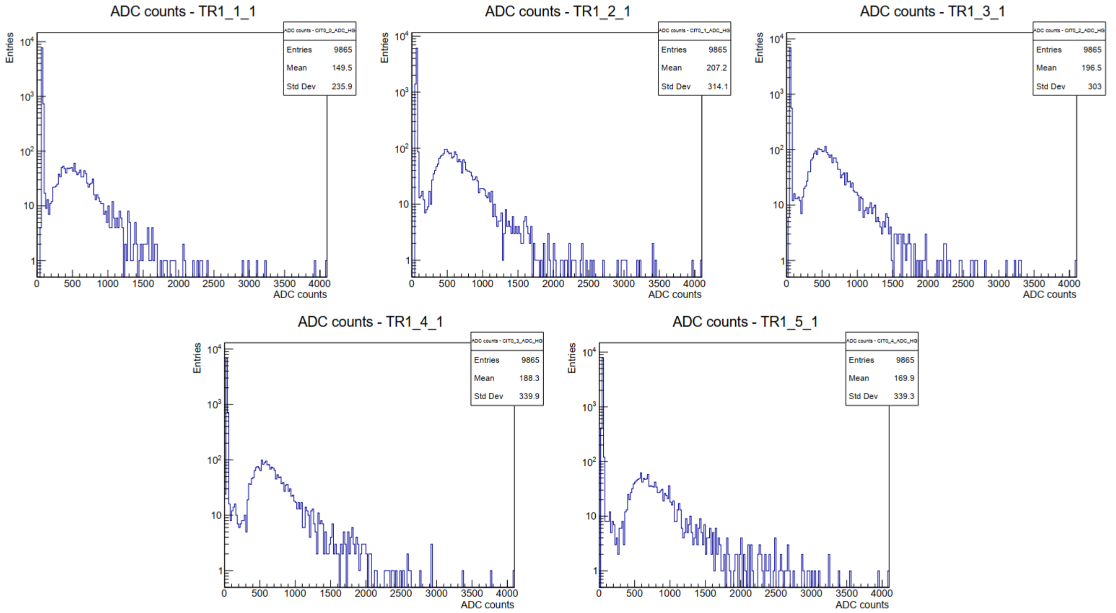

(a) TR1 scintillators

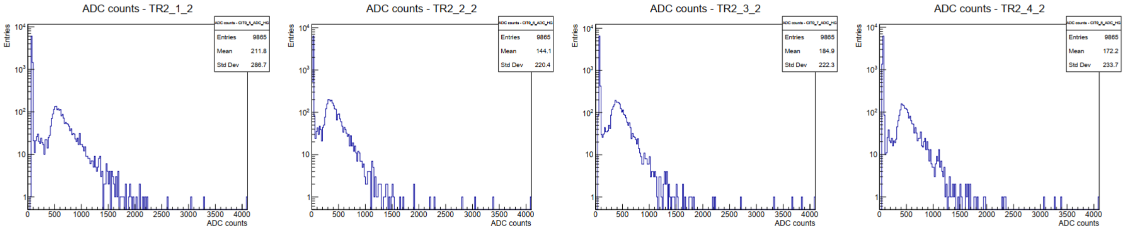

(b) TR2 scintillators

Figure 4.20: ADC distributions of TR1 and TR2 for cosmic muons acquisition (courtesy of the CSES-Limadou collaboration): the peaks have been equalized by changing the bias voltages of PMTs. The TR1 distributions are wider due to the lower attenuation factors to that of TR2 scintillators

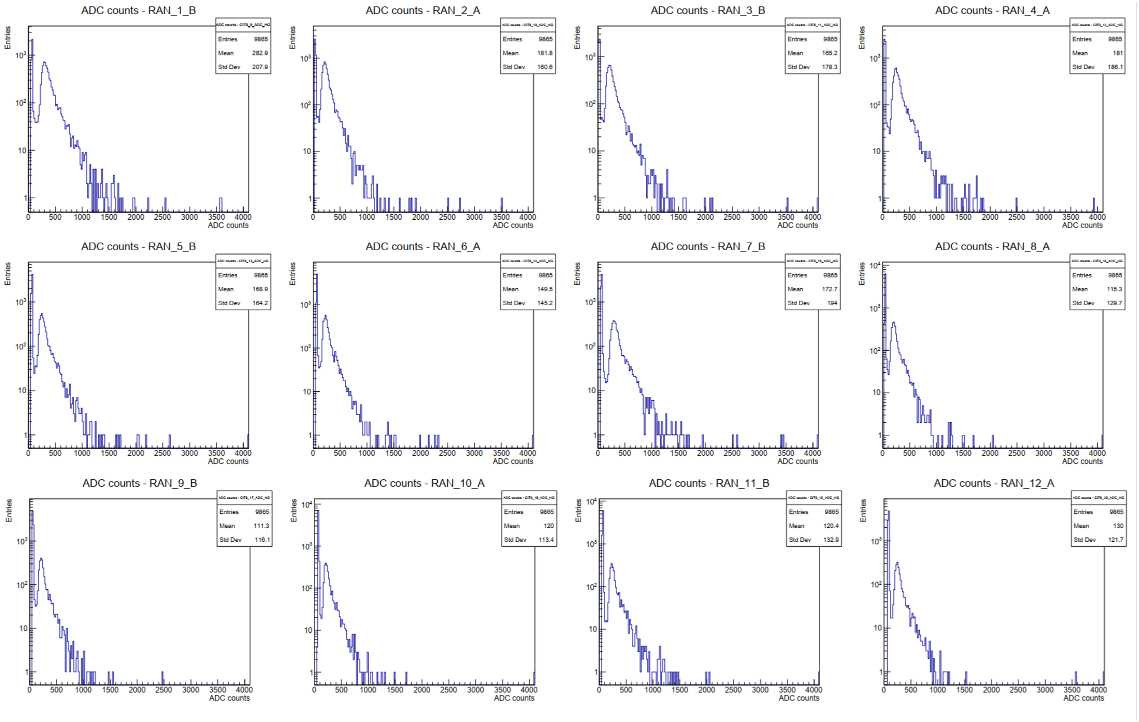

Figure 4.21: ADC distributions of RAN scintillators for cosmic muons acquisition (courtesy of the CSES-Limadou collaboration): these distributions are similar to that of TR2 being the attenuation and preamplifiers' gain factors the same

In figure 4.20, 4.21 and 4.22, the High Gain ADC count distributions of one of these acquisitions are reported as an example. In this acquisition, the PMT voltages were tuned to equalize the MPV of the distributions.

From these plots, it is possible to see how the cosmic muons pass throughout the detector as expected. The wider distribution of LATs should be attributed to the larger size of lateral scintillators.

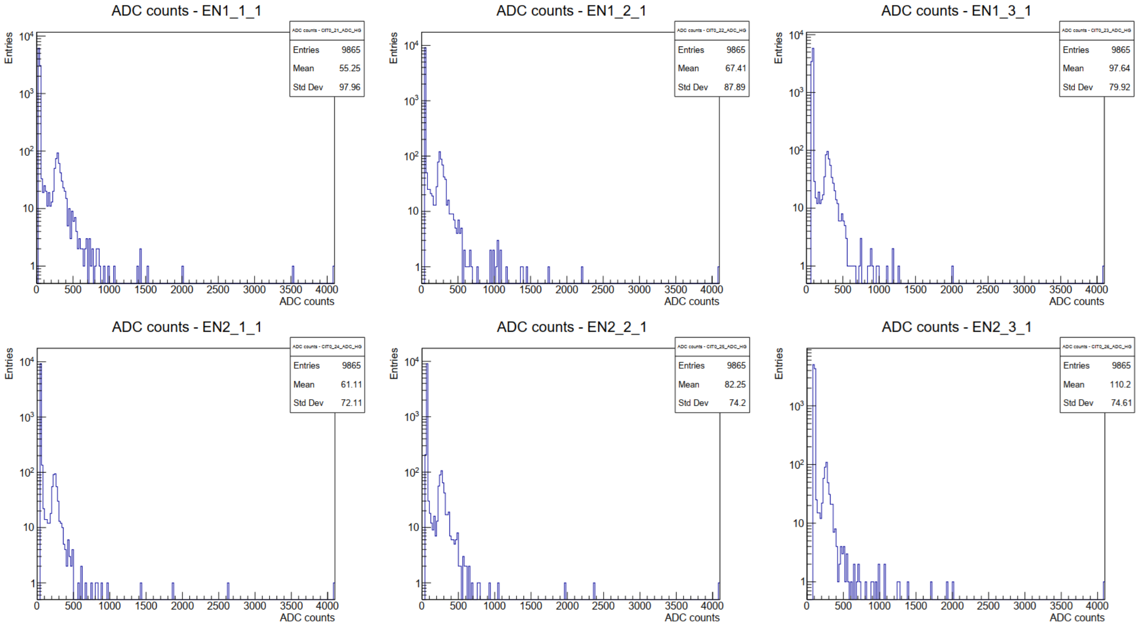

(a) EN1 and EN2 scintillators

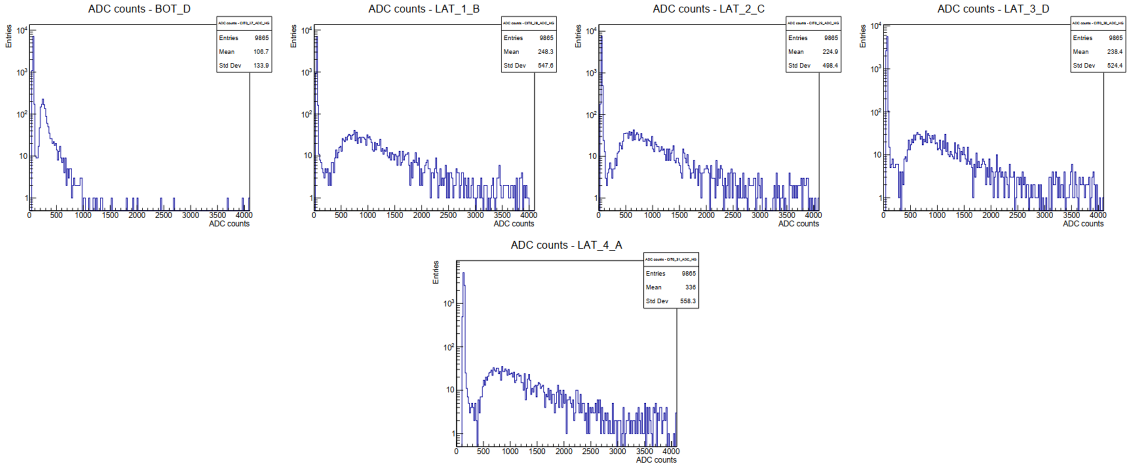

(b) BOT and LAT scintillators

Figure 4.22: ADC distributions of LYSO crystals and VETO for cosmic muons acquisition (courtesy of the CSES-Limadou collaboration): the EN distributions are sharper than the TR1, TR2 and RAN given that the preamplifiers to which they are connected have the lowest gain. The LAT distributions, instead, are the most spread due to the large size of lateral scintillators

5

HEPD-02 qualification and acceptance tests

The HEPD-02 detector has been intensively tested to ensure correct operation in the space environment, where extreme temperature variations can occur and radiation levels are higher. Furthermore, heat transfer can only occur through radiation due to the absence of an atmosphere.

Besides these conditions, during the launch of the satellite, the detector experiences strong mechanical shocks and vibrations that could potentially damage it. To a lesser extent, also its shipping could be a source of mechanical stresses.

For these reasons, the PMT&T board and all the HEPD-02 subsystems are designed with specific measures that include redundancy, passive cooling and the use of radiation-hardened or military-grade components.

Environmental tests are fundamental for detectors designed for space and standard test procedures were followed for the HEPD-02 qualification. Subsequently, the physics performances have been evaluated with beam tests conducted in different facilities and with different particles. Particular attention was dedicated also to testing the functionality of the GRB detection algorithm.

5.1 Environmental tests

The environmental tests campaign included the following investigations, described in detail in the next sections:

- Pyroshock and vibration tests
- Thermal and thermal-vacuum tests
- Electromagnetic Compatibility (EMC) tests

All of them have been carried out on both the Qualification Model and the Flight Model of the detector.

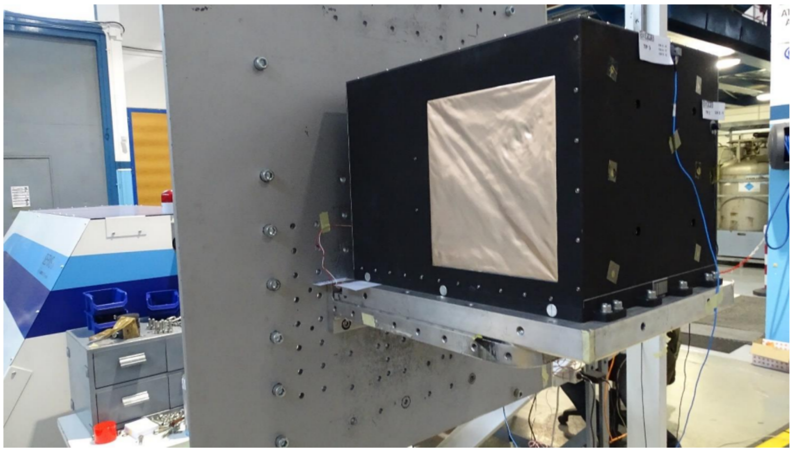

Figure 5.1: Experimental setup used for pyroshock tests (courtesy of the CSES-Limadou collaboration)

5.1.1 Pyroshock tests

The detector has been tested to ensure its resistance to damages that could be caused by pyrotechnical devices present on the satellite. These devices can be employed for various reasons: to separate structural subsystems (such as payloads from launch vehicles), deploy solar panels or activate propellant valves.

These tests took place from 12 to 14 December 2022 at the SERMS facility in Terni.

A preliminary sinusoidal vibration test, with frequencies from 100 to 500 Hz, has been made with a shaker system (made by TIRA), aimed to obtain the resonance frequencies of HEPD-02 before the pyrotechnic shock.

Then the detector was mounted on a ringing plate facing an impulse hammer and subject to an impact with shock frequencies from 600 to 4000 Hz and maximum accelerations over 1200 g.

After this, an additional vibration test has been made to check that no new resonance frequencies are presented after the shock.

The acceleration data was acquired using accelerometers placed both on the HEPD-02 and the ringing plate.

This procedure has been repeated for all the three axes of the detector.

The experimental setup is depicted in figure 5.1. As an example, the shock response spectrum (SRS), for the test along the Y axis, is shown in figure 5.2 besides the acceleration time history (that is the SRS plot but in the time domain).

The comparison of resonance frequency before and after the pyroshock test is shown in figure 5.3. It is possible to see that no anomalous resonance peaks were observed.

5.1.2 Vibration tests

During the launch of the satellite, the payloads are subject to intense vibrations that sweep a wide range of frequencies. Vibration tests allow us to check that the detector will not be damaged during this phase.

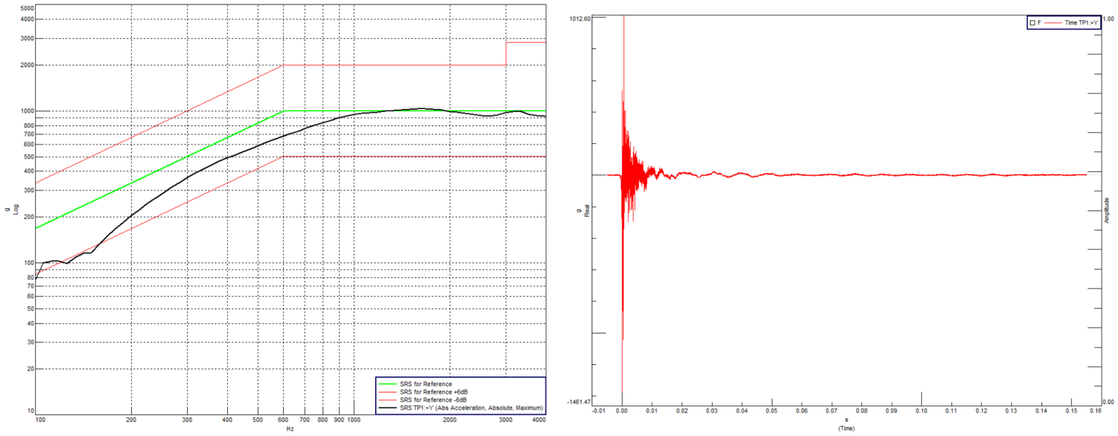

(a) Shock response spectrum

(b) Acceleration time history

Figure 5.2: SRS curve and acceleration time history obtained from the pyroshock test along the Y axis (courtesy of the CSES-Limadou collaboration)

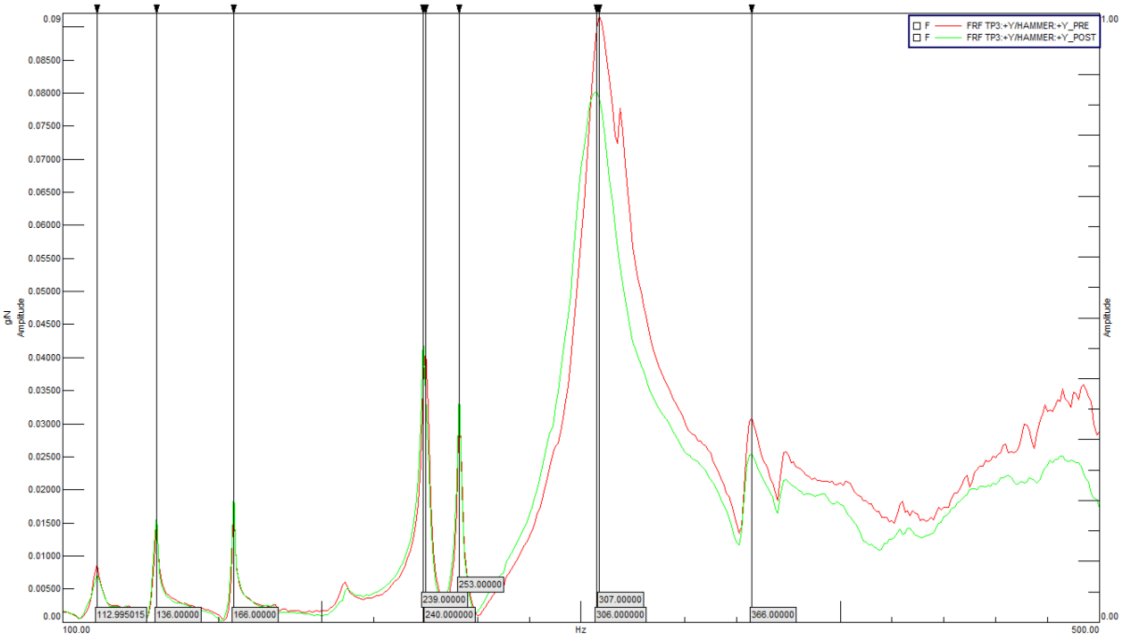

Figure 5.3: Resonance search comparison from pyroshock test along the Y axis. The red line represents the acceleration measurements before the test, while the green line represents the values acquired after (courtesy of the CSES-Limadou collaboration)

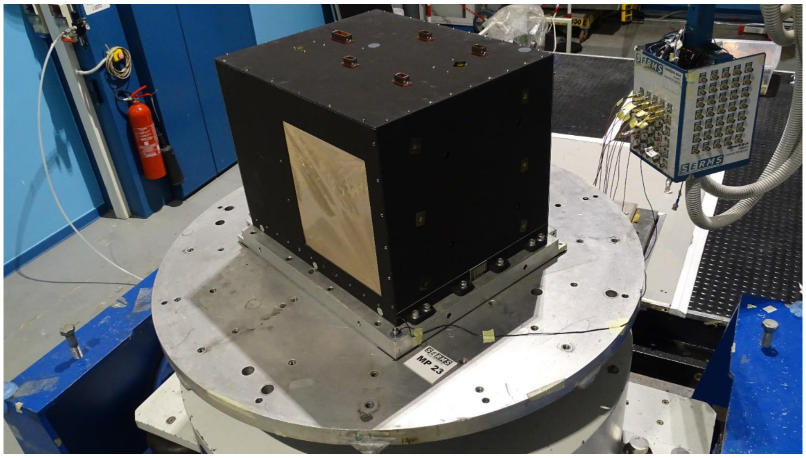

Figure 5.4: HEPD-02 placed on the shaker for the vibration tests along the X-axis (courtesy of the CSES-Limadou collaboration)

The vibration tests on HEPD-02 were performed from 22 to 23 February 2023 at the Terni SERMS facility, using TIRA shaker systems.

The procedure used for these tests involved a first resonance-frequency search, followed by a sinusoidal and then a random vibration and, after these, another resonance-frequency search. Comparing the two resonance spectra, it is possible to check for anomalous peaks and to evaluate the amplitude shift between each peak.

For the QM the sinusoidal vibration reached accelerations up to 12 g with frequencies from 10 to 100 Hz and a sweep rate of 2 octaves/min. The random vibration had an overall acceleration of 11.3 g(RMS) and a spectrum from 10 to 2000 Hz. The FM was tested with more conservative values: 8 g for the sinusoidal vibration and 7.55 g(RMS) for the random vibration.

During these tests, the HEPD-02 was in the acquisition state and configured to detect cosmic muons to check its normal functioning. The same procedures were repeated for all the axes of HEPD-02.

Figure 5.4 shows the experimental setup while figure 5.5 shows the results of the vibration tests along the X-axis of the FM, using the detector's internal accelerometer readings (three for each axis). It is possible to observe that no anomalies or resonance peaks were found.

5.1.3 Thermal tests

The compatibility of the detector with extreme temperature variations has been evaluated with thermal tests, performed at the SERMS facility from 24 February to 14 March 2023.

In figure 5.6 the HEPD-02 is shown inside the climatic chamber (made by Angelantoni). The temperature cycle used is shown in figure 5.7a: during the QM tests, the temperature of the chamber was alternated from −30 to 50 °C for a total of 25.5 cycles and with a temperature change rate of 4 °C/min. The FM was tested under less extreme conditions,

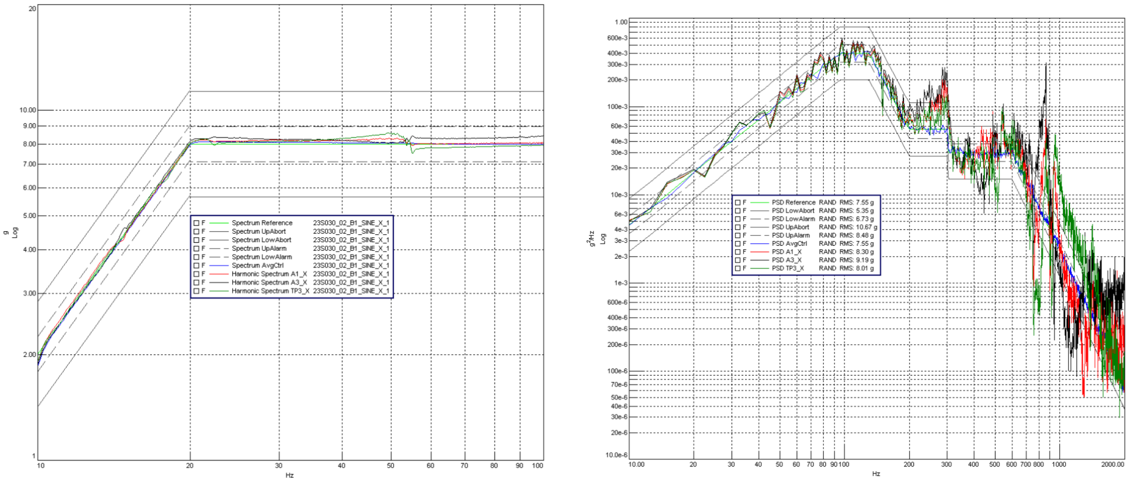

(a) Response spectrum of the sinusoidal vibration test along the X-axis

(b) Response spectrum of the sinusoidal vibration test along the X-axis

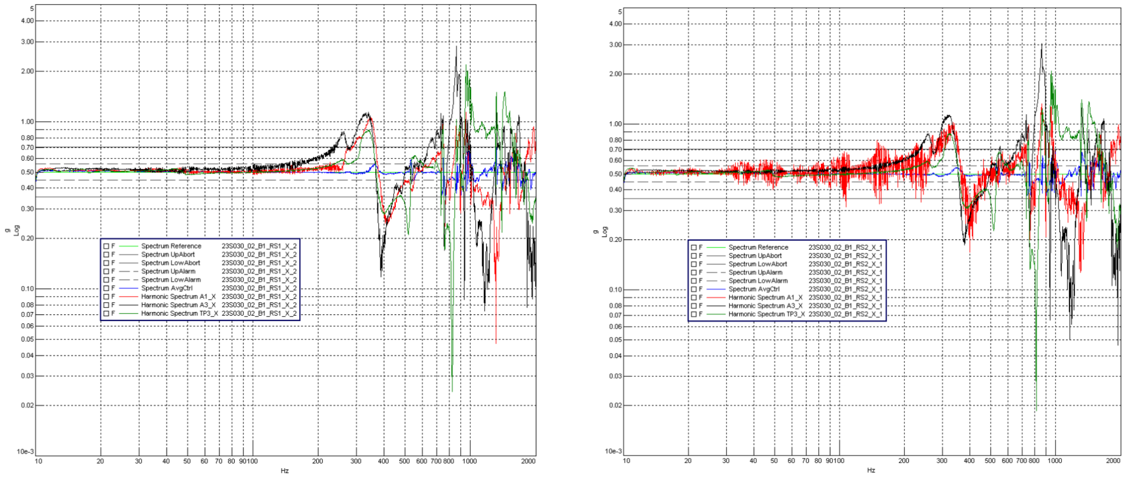

(c) Resonance search before the sinusoidal and random tests

(d) Resonance search after the sinusoidal and random tests

Figure 5.5: Plots obtained during the vibration test along the X-axis of the FM are shown (courtesy of the CSES-Limadou collaboration)

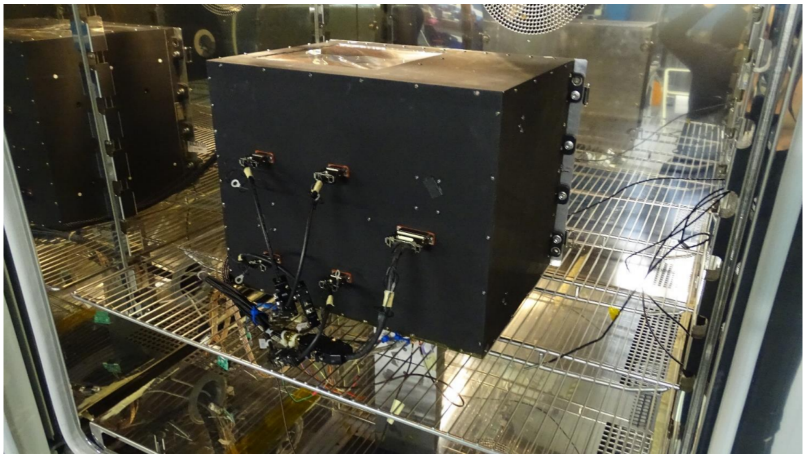

Figure 5.6: HEPD-02 inside the climatic chamber during thermal tests (courtesy of the CSES-Limadou collaboration)

limiting the temperature range to -20 to $45\,^{\circ}\mathrm{C}$ and the number of cycles to 14.5.

At each cycle, the detector has been powered on, calibrated with the internal calibration trigger, put in acquisition mode to detect cosmic muons and then powered off. This allows us to check the correct functioning of HEPD-02 during in-flight procedures.

The detector successfully passed the thermal tests without anomalies.

5.1.4 Thermal-vacuum tests

Besides extreme temperature variations, the space environment is characterized by the absence of an atmosphere and thermal conduction is mainly due to irradiation and conduction.

Thermal-vacuum tests allow us to simulate this environment and test the ability of the detector to withstand these conditions.

The HEPD-02 was subjected to these tests from 8 to 14 May 2023 at SERMS using an Angelantoni vacuum chamber.

The thermal cycles were the same as the thermal tests but with only 3.5 cycles and the pressure was kept below $6.65 \cdot 10^{-3}$ Pa. Figure 5.8 shows the HEPD-02 on the vacuum chamber's plate.

5.1.5 EMC tests

The last environmental test was the Electromagnetic Compatibility (EMC), aimed at studying the emission and susceptibility of the detector to ensure the immunity to electromagnetic emissions and the mutual EM compatibility of the satellite's subsystems. These tests were carried out at the IFAC facility (Sesto Fiorentino) from 11 April to 19 July 2023.

The emission tests have the purpose of studying the conducted and radiated electromagnetic **emissions** of the HEPD-02. During all the tests the detector was configured to acquire cosmic muons.

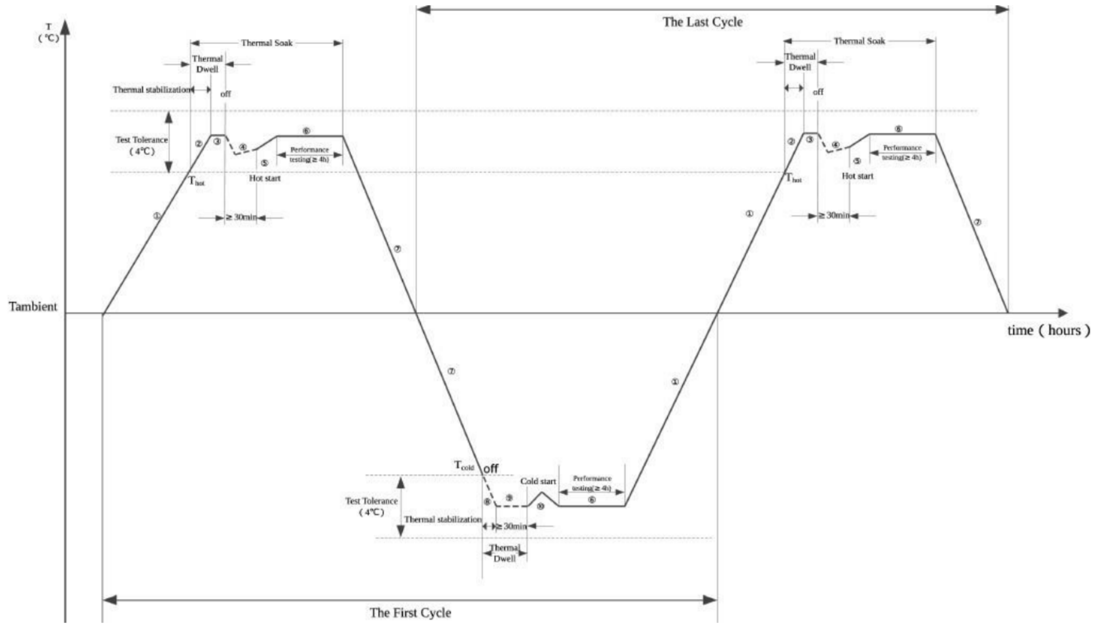

(a) Thermal cycle plot

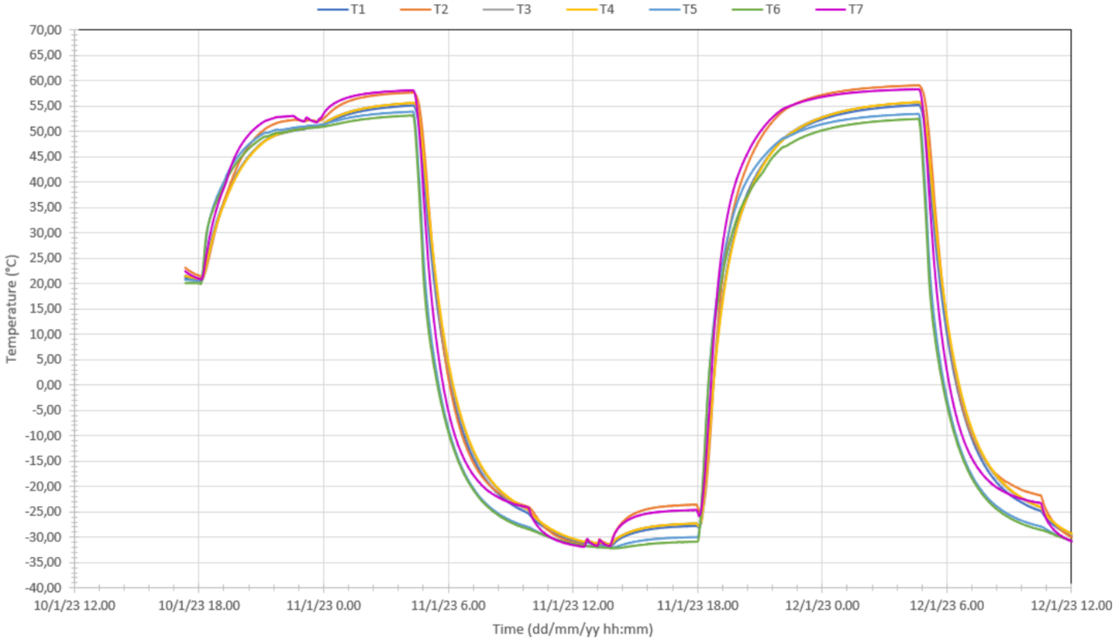

(b) Actual temperatures acquired by sensors placed in different positions on HEPD-02

Figure 5.7: Plot of the first two cycles used in the thermal test (courtesy of the CSES-Limadou collaboration)

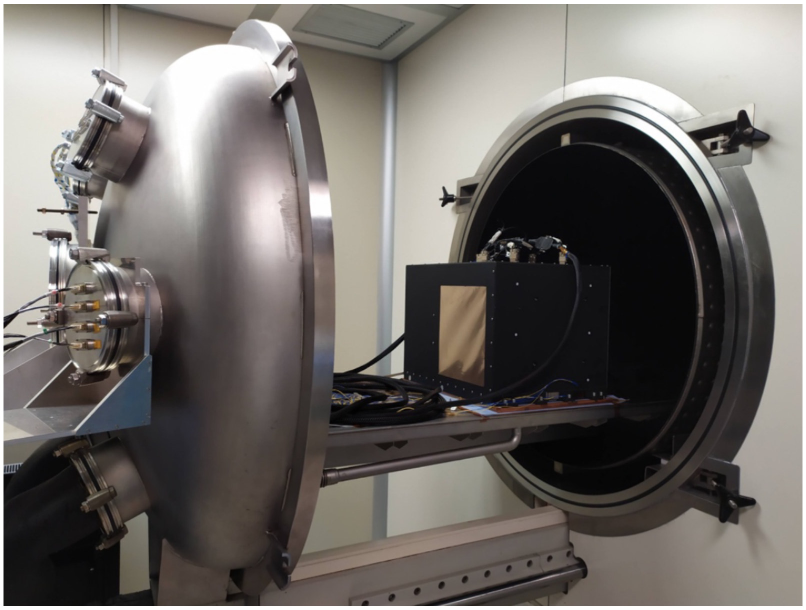

Figure 5.8: HEPD-02 and the vacuum chamber (courtesy of the CSES-Limadou collaboration)

Emission tests

To investigate the **conducted emissions** the setup shown in figure 5.9a was used: the power and return lines of the detector are connected to two "line impedance stabilization network" (LISN) that are connected to the EGSE (Electrical Ground Support Equipment[1]) power output. The LISNs are needed to remove the contribution of the EGSE to the emissions.

A spectrum analyzer is connected to the LISN control output and performs a frequency scan between 150 kHz and 10 MHz.

The **radiated emission** test setup is described in figure 5.9b and differs from the preceding test by using an antenna connected to the spectrum analyzer instead of a cable. In this case, the investigated frequency range spans from 200 MHz to 2 GHz.

Susceptibility tests

The susceptibility tests are meant to study the ability of the detector to continue to work as expected in the presence of electromagnetic disturbances.

Figure 5.10a schematizes the experimental setup for **conducted susceptibility** test: the power line of the detector is connected to the secondary coil of a coupling transformer while the primary coil to a signal generator. An oscilloscope is used to evaluate the injected voltage, produced with frequencies in the range from 30 Hz to 150 kHz.

The **radiated susceptibility** test is schematized in figure 5.10b, where the disturbance is produced by an antenna connected to the signal generator. To evaluate the produced

---

[1] The EGSE is the interface to the detector, allowing the communication and the acquisition of data via software. It also hosts the power supply.

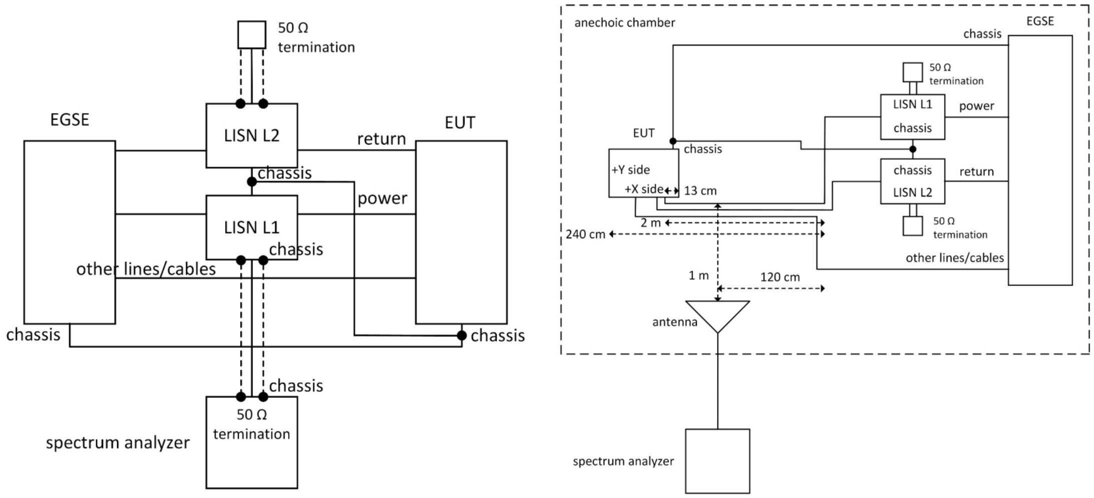

(a) Conducted emission test **(b)** Radiated emission test

Figure 5.9: Conducted and radiated emissions tests for HEPD-02, named EUT as "Equipment Under Test" (courtesy of the CSES-Limadou collaboration)

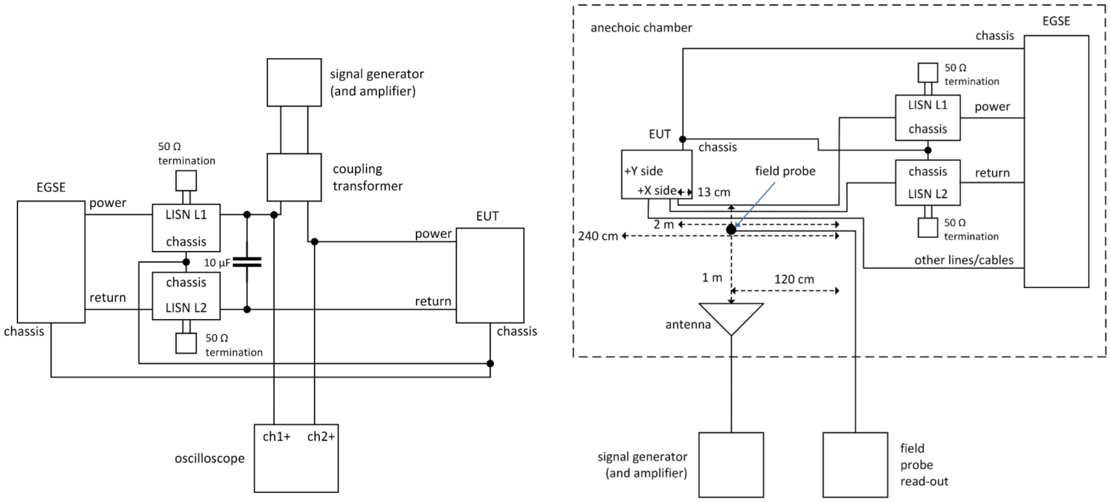

(a) Conducted susceptibility test **(b)** Radiated susceptibility test

Figure 5.10: Conducted and radiated susceptibility tests for HEPD-02, named EUT as "Equipment Under Test" (courtesy of the CSES-Limadou collaboration)

signal, a field probe is placed near the detector. The frequency range for this test is from 10 kHz to 40 GHz.

5.2 Physics performances

The HEPD-02 successfully passed all the environmental tests and its physics performances were subsequently evaluated [48]. For this purpose, a series of beam tests have been conducted at the following facilities:

- Beam Test Facility (BTF) in Frascati, with an **electrons** beam with energies from 30 to 120 MeV. This campaign took place from 3 to 7 April and from 22 to 25 June 2023.
- Proton Therapy Center facility in Trento, using **protons** with energies from 30 to 200 MeV, from 6 to 21 June.
- LINAC facility in Trento, during the same period of the previous beam test, with **electrons** of 6 MeV, 9 MeV and 12 MeV and **photons** in a continuum energy spectrum from 1 to 10 MeV
- CNAO facility in Padova, with **protons** and **carbons nuclei** with energies from 115 to 398 MeV/amu, that took place from 7 to 8 July

In figure 5.11, the experimental setup used in the different tests is shown.

All the tests consisted of a first calibration procedure, during which the PMT&T board constantly acquire PMT data with a frequency determined by the internal calibration trigger, which can be configured using bits 31 to 15 of `CMD_REG` register (see section 3.2.2). This procedure allows obtaining the ADC values of pedestals, used during the analysis for channels normalization. Then the detector was configured in acquisition mode, where the trigger is produced only by the selected trigger masks, powered on.

All ten possible trigger masks were used during the beam tests and different configurations of concurrency were used in order to check both the correct functioning of the firmware and to evaluate the best configurations to be adopted during the flight.

Charged particles

In this section, results from the beam test with charged particles are reported.

Figure 5.12 shows, as an example, the ADC counts of the PMTs connected to the calorimeter's scintillators during the beam test at the Proton Therapy facility, with 70 MeV protons. Only a subset of the PMTs are reported for readability.

The ADC acquired from the five segments of TR1 and TR2 are shown in figure 5.12a and 5.12b. From these plots, it is possible to evaluate the region where the beam was aimed: in TR1 most of the particles passed in the fourth segment (TR1_4_1) while the

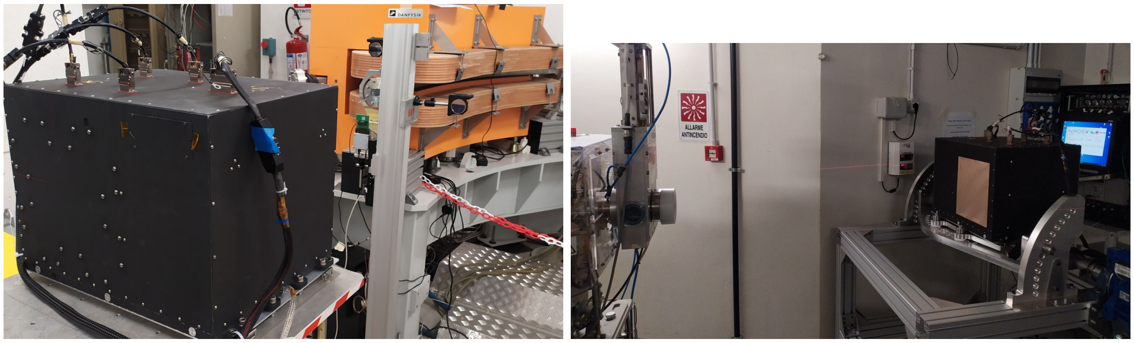

(a) BTF facility **(b)** Proton Therapy Center

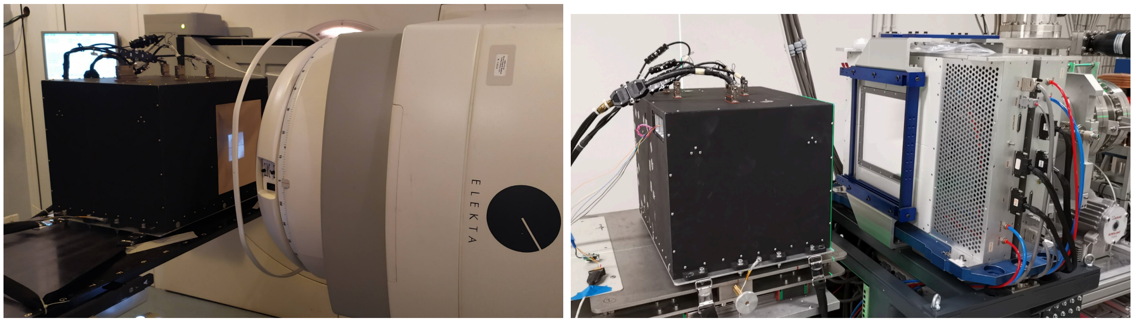

(c) LINAC **(d)** CNAO

Figure 5.11: HEPD-02 beam tests (courtesy of the CSES-Limadou collaboration)

peaks in nearby scintillators (TR1_3_1 and TR1_5_1) are less pronounced, almost no signal is produced in TR1_1_1 and TR1_2_1.

In TR2 the lateral slabs are mainly affected by the beam particles as can be seen by the peak distribution of TR2_1_2 and TR2_2_2.

The presence of the peaks only in RAN_1_B and RAN_2_A indicates that the energy of the particles was only sufficient to pass through the first two planes of the calorimeter.

The absence of signal in the distributions from the last two segmented planes of LYSO crystal shows that the particles are fully contained inside the detector.

Correlation plots between the two coupled PMTs for each scintillator are shown in figure 5.13. It is possible to see that the ADC counts from the couples of PMTs are displaced along the bisector of the plots, showing a good correlation.

The data obtained from all the beam tests have been analyzed by the CSES-Limadou collaboration's analysis group and the calibration plots in figure 5.14 have been obtained.

In figure 5.14a, the energy reconstructed by HEPD-02 data is plotted as a function of the beam energies and it is possible to see an overall good linearity. Figure 5.14b shows the deposited energies for protons, acquired at the LINAC facility, as a function of the calorimeter's scintillators and it is possible to recognize the typical Braggs curves.

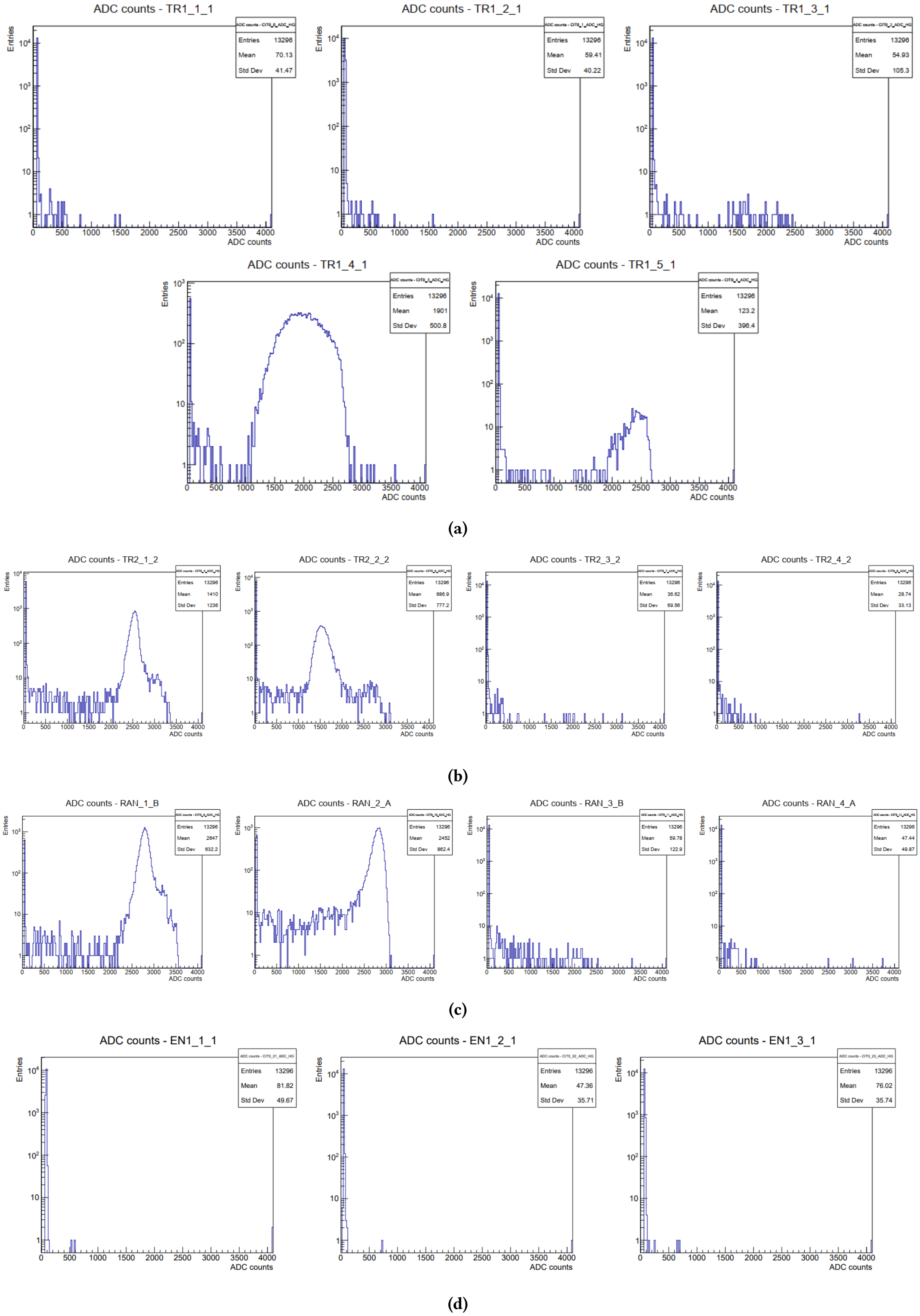

Figure 5.12: ADC counts acquired by HEPD-02 for 70 MeV protons at Proton Therapy facility (courtesy of the CSES-Limadou collaboration)

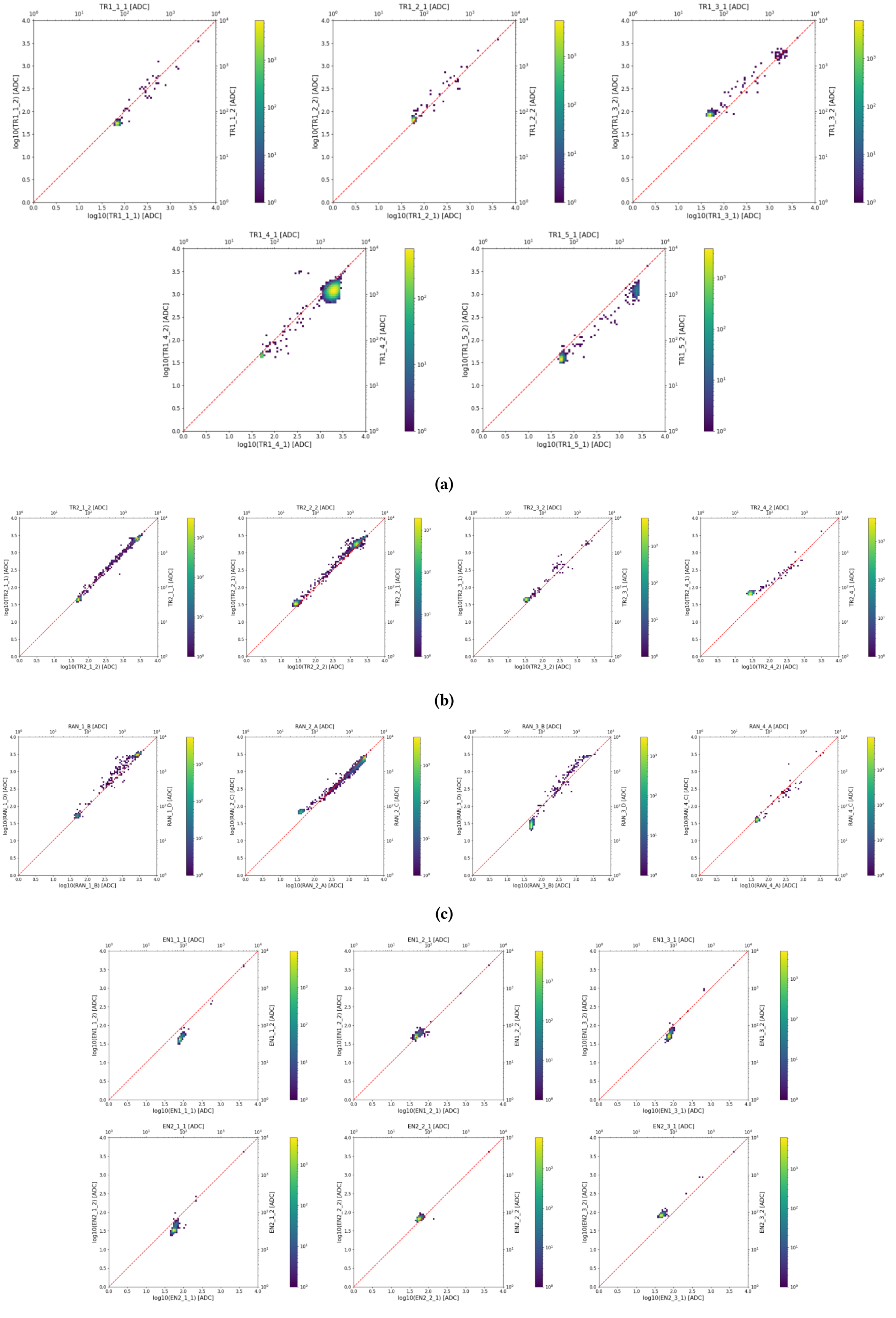

(a)

(b)

(c)

(d)

Figure 5.13: Correlation plots for 70 MeV protons acquired at Proton Therapy facility (courtesy of the CSES-Limadou collaboration)

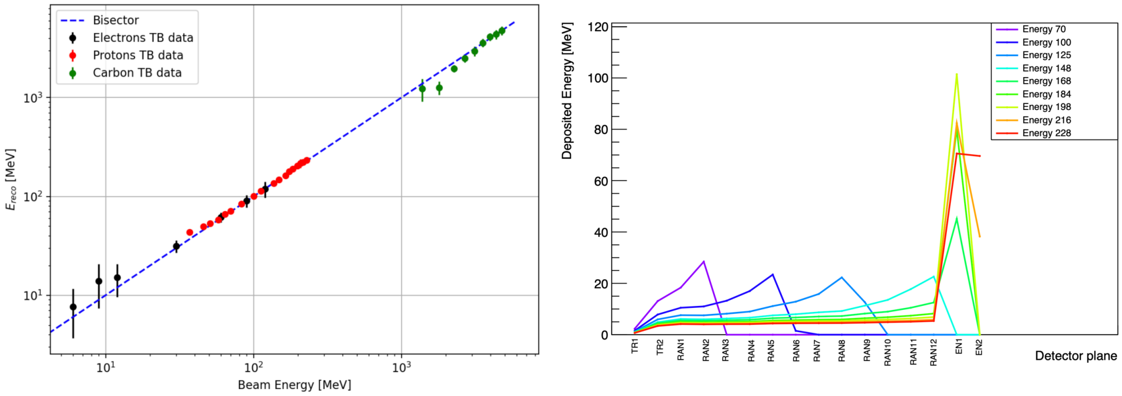

(a) Energy calibration curve

(b) Braggs curves for protons

Figure 5.14: Analysis of the beam tests data acquired at LINAC facility (courtesy of the CSES-Limadou collaboration)

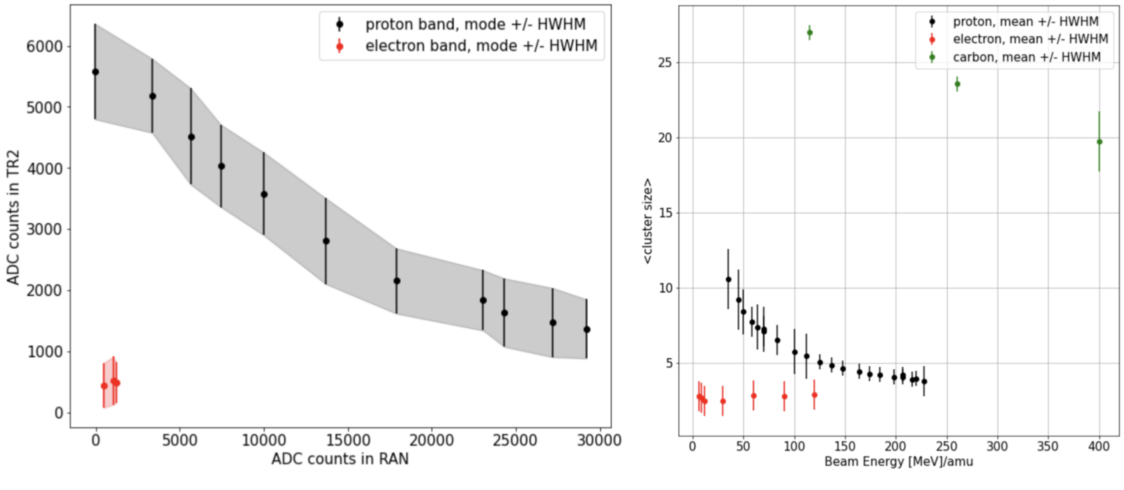

(a)

(b)

Figure 5.15: Particle identification: (a) using T2 ADC counts as a function of the total ADC counts in the detector, (b) evaluating the tracker's cluster size [48]

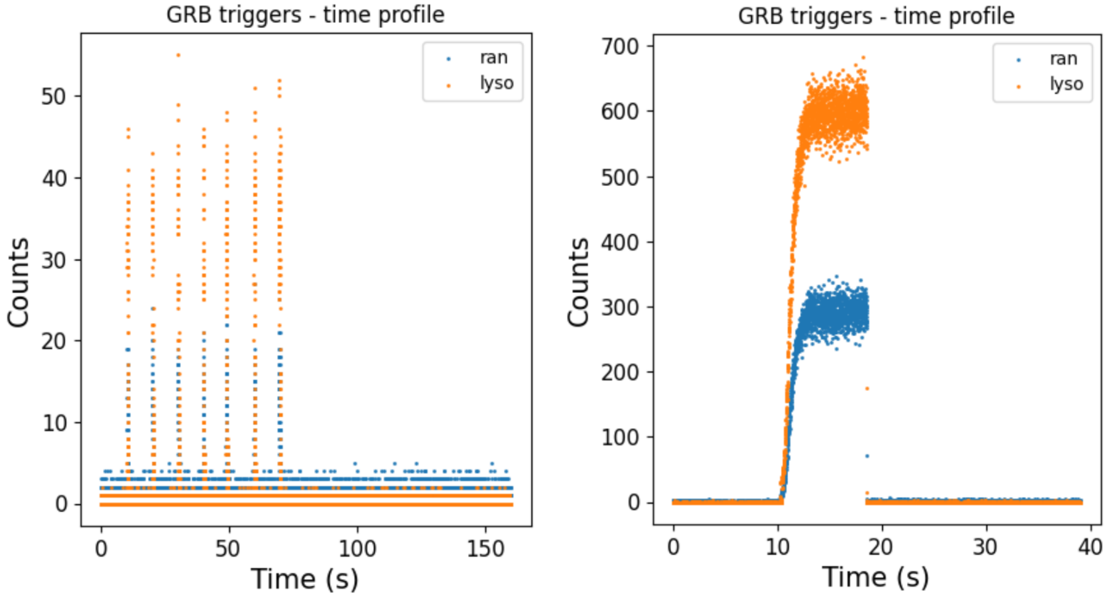

(a) Multiple photon bursts **(b)** Single photon burst of ~ 10 s

Figure 5.16: GRB counters acquired during beam tests at the LINAC facility using X-ray pulses (courtesy of the CSES-Limadou collaboration)

Particle identification

The discrimination between electrons, protons and heavier particles is an important part of HEPD-02 data analysis and can be achieved using two different techniques: the dE/dx vs E_{total} method or evaluating the pixel's cluster size of the direction detector [49].

Figure 5.15a shows the first method applied to beam test data where the separation between the proton curves and the electrons is clear.

The cluster size method is shown in figure 5.15b and also shows a good separation between particles.

Photons

At the LINAC facility, it was possible to produce X-rays by electrons bremsstrahlung, accelerating them with potential differences of 4 MV, 6 MV and 10 MV.

This allowed us to test the GRB detection algorithm with the two different trigger masks for short and long photon bursts.

As an example, figure 5.16a shows the GRB counters acquired producing seven short bursts, while figure 5.16b shows the capability of detecting also long bursts (in this case with a duration of ~ 10 s.

This test showed that this new functionality works as expected and that the GRB detection with HEPD-02 will be possible.

6
Conclusions

My activity as a PhD student focused on the development of the PMT&T system and related functional tests and calibrations. A significant part of the system development was writing the PMT&T board firmware. The version I developed provides new functionalities that will improve the HEPD-02 capabilities with respect to the previous mission.

The added functionalities include new trigger masks and rate meters for GRB detection, which take advantage of the high density of LYSO crystals for detecting photons.

Moreover, I redesigned the trigger system to provide six programmable trigger masks working in concurrency, of which four can be prescaled to reduce the trigger rate in regions of the satellite's orbit, such as the SAA and the poles, where the particle rate can reach tens of megahertz.

I carried out a campaign of tests and measurements to obtain the power consumption per channel, the calibration curves of CITIROCs' preamplifiers and shapers and the threshold curves. These curves helped to reconstruct the particle energies during the beam tests. The concurrent and prescaled triggers have been tested as well and worked as expected.

After the finalization of the board, I participated in the integration of all the subsystems, followed by the first successful acquisition of cosmic muons using the Qualification Model of the detector.

The QM and FM models of HEPD-02 were subjected to environmental tests to ensure their correct operations in a space environment.

Finally, I also joined some of the beam tests that allowed us to evaluate the detector's scientific performances, test the GRB detection algorithm and obtain energy calibration curves for different particles and energy ranges.

Thanks to the work carried out, HEPD-02 can be considered a substantial upgrade to HEPD-01, providing improved energy resolution and range, new trigger techniques and the sensibility to GRBs, which will allow joining the international network of GRB detectors.

The Flight Model of HEPD-02 successfully passed environmental tests and showed excellent performances during beam tests, confirming the quality of the overall design and the functional and calibration tests made during the detector's integration.

Bibliography

[1] https://cses.web.roma2.infn.it/. 2023.

[2] Thibery Cussac et al. "The Demeter microsatellite and ground segment". In: *Planetary and Space Science* 54.5 (2006). First Results of the DEMETER Micro-Satellite, pp. 413–427. ISSN: 0032-0633. DOI: `https://doi.org/10.1016/j.pss.2005.10.013`. URL: `https://www.sciencedirect.com/science/article/pii/S0032063305002047`.

[3] J.H. Seinfeld and S.N. Pandis. *Atmospheric Chemistry and Physics: From Air Pollution to Climate Change*. Wiley, 2016. ISBN: 9781118947401. URL: `https://books.google.it/books?id=n_RmCgAAQBAJ`.

[4] K Mohanakumar. *Stratosphere troposphere interactions: An introduction*. Jan. 2008. ISBN: 1402082169. DOI: `10.1007/978-1-4020-8217-7`.

[5] R.J. Goldston. *Introduction to Plasma Physics*. CRC Press, 2020. ISBN: 9781439822074. URL: `https://books.google.it/books?id=TZHzDwAAQBAJ`.

[6] M.C. Kelley. *The Earth's Ionosphere: Plasma Physics and Electrodynamics*. ISSN. Elsevier Science, 2009. ISBN: 9780080916576.

[7] K. Davies. *Ionospheric Radio*. Electromagnetics and Radar Series. Institution of Engineering & Technology, 1990. ISBN: 9780863411861. URL: `https://books.google.it/books?id=qdWUKSj5PCcC`.

[8] K. Maeda and S. Kato. "Electrodynamics of the Ionosphere". In: *Space Science Reviews* 5.1 (1966), pp. 57–79. DOI: `10.1007/BF00179215`.

[9] M.G. Kivelson and C.T. Russell. *Introduction to Space Physics*. Cambridge University Press, 1995. ISBN: 9781316264669. URL: `https://books.google.it/books?id=DIybBQAAQBAJ`.

[10] Martin Walt. *Introduction to Geomagnetically Trapped Radiation*. Cambridge Atmospheric and Space Science Series. Cambridge University Press, 1994. DOI: `10.1017/CBO9780511524981`.

[11] Piersanti M. et al. "Magnetospheric–Ionospheric–Lithospheric Coupling Model. 1: Observations during the 5 August 2018 Bayan Earthquake". In: *Remote Sensing* 12.20 (2020). ISSN: 2072-4292. DOI: `10.3390/rs12203299`. URL: `https://www.mdpi.com/2072-4292/12/20/3299`.

[12] S. Pulinets and D. Ouzounov. "Lithosphere–Atmosphere–Ionosphere Coupling (LAIC) model – An unified concept for earthquake precursors validation". In: *Journal of Asian Earth Sciences* 41.4 (2011). Validation of Earthquake Precursors-VESTO, pp. 371–382. ISSN: 1367-9120. DOI: `https://doi.org/10.1016/j.jseaes.2010.03.005`. URL: `https://www.sciencedirect.com/science/article/pii/S1367912010000830`.

[13] S. Pulinets and K. Boyarchuk. *Ionospheric Precursors of Earthquakes*. Springer, 2004. ISBN: 9783540208396.

[14] S.A. Pulinets, A.D. Legen'ka, T.V. Gaivoronskaya, and V.Kh. Depuev. "Main phenomenological features of ionospheric precursors of strong earthquakes". In: *Journal of Atmospheric and Solar-Terrestrial Physics* 65.16 (2003), pp. 1337–1347. ISSN: 1364-6826. DOI: `https://doi.org/10.1016/j.jastp.2003.07.011`. URL: `https://www.sciencedirect.com/science/article/pii/S136468260300172X`.

[15] Sergey Pulinets and Kirill Boyarchuk. *The Basic Components of Seismo-Ionospheric Coupling*. Jan. 2004. ISBN: 3-540-20839-9. DOI: `10.1007/3-540-26468-X_1`.

[16] Piergiorgio Picozza et al. "Scientific Goals and In-orbit Performance of the High-energy Particle Detector on Board the CSES". In: *The Astrophysical Journal Supplement Series* 243 (July 2019), p. 16. DOI: `10.3847/1538-4365/ab276c`.

[17] M. Piersanti et al. "Adaptive Local Iterative Filtering: A Promising Technique for the Analysis of Nonstationary Signals". In: *Journal of Geophysical Research: Space Physics* 123.1 (2018), pp. 1031–1046. DOI: `https://doi.org/10.1002/2017JA024153`. eprint: `https://agupubs.onlinelibrary.wiley.com/doi/pdf/10.1002/2017JA024153`. URL: `https://agupubs.onlinelibrary.wiley.com/doi/abs/10.1002/2017JA024153`.

[18] Piersanti M. et al. "A mathematical model of lithosphere–atmosphere coupling for seismic events". In: *Scientific Reports* 11 (2021). DOI: `https://doi.org/10.1038/s41598-021-88125-7`.

[19] Palma et al. "The August 2018 Geomagnetic Storm Observed by the High-Energy Particle Detector on Board the CSES-01 Satellite". In: *Applied Sciences* 11.12 (2021). ISSN: 2076-3417. DOI: `10.3390/app11125680`. URL: `https://www.mdpi.com/2076-3417/11/12/5680`.

[20] S. Bartocci et al. "Galactic Cosmic-Ray Hydrogen Spectra in the 40–250 MeV Range Measured by the High-energy Particle Detector (HEPD) on board the CSES-01 Satellite between 2018 and 2020". In: *The Astrophysical Journal* 901.1 (Sept. 2020), p. 8. DOI: `10.3847/1538-4357/abad3e`. URL: `https://dx.doi.org/10.3847/1538-4357/abad3e`.

[21] Martucci et al. "New results on protons inside the South Atlantic Anomaly, at energies between 40 and 250 MeV in the period 2018–2020, from the CSES-01 satellite mission". In: *Phys. Rev. D* 105 (6 Mar. 2022), p. 062001. DOI: `10.1103/PhysRevD.105.062001`. URL: `https://link.aps.org/doi/10.1103/PhysRevD.105.062001`.

[22] Matteo Martucci et al. "Trapped Proton Fluxes Estimation Inside the South Atlantic Anomaly Using the NASA AE9/AP9/SPM Radiation Models along the China Seismo-Electromagnetic Satellite Orbit". In: *Applied Sciences* 11.8 (2021). ISSN: 2076-3417. DOI: `10.3390/app11083465`. URL: `https://www.mdpi.com/2076-3417/11/8/3465`.

[23] F. Palma et al. "Gamma-Ray Burst Observations by the High-Energy Particle Detector on board the China Seismo-Electromagnetic Satellite between 2019 and 2021". In: *The Astrophysical Journal* 960.1 (Dec. 2023), p. 21. DOI: `10.3847/1538-4357/ad06ae`. URL: `https://dx.doi.org/10.3847/1538-4357/ad06ae`.

[24] Cristian De Santis and Sergio Ricciarini. "The High Energy Particle Detector (HEPD-02) for the second China Seismo-Electromagnetic Satellite (CSES-02)". In: *PoS* ICRC2021 (2021), p. 058. DOI: `10.22323/1.395.0058`.

[25] Mese et al. "The HEPD-02 trigger and PMT readout system for the CSES-02 mission". In: *PoS* ICRC2021 (2021), p. 063. DOI: `10.22323/1.395.0063`.

[26] Marco Mese et al. "The PMT Acquisition and Trigger Generation System of the HEPD-02 Calorimeter for the CSES-02 Satellite". In: *Instruments* 7.4 (2023). ISSN: 2410-390X. DOI: `10.3390/instruments7040053`. URL: `https://www.mdpi.com/2410-390X/7/4/53`.

[27] R. Nicolaidis et al. "The TDAQ system of the HEPD-02 on the CSES-02 mission". In: *PoS* ICRC2023 (2023), p. 1321. DOI: `10.22323/1.444.1321`.

[28] Ester Ricci. "A pixel based tracker for the HEPD-02 detector". In: *PoS* ICRC2023 (2023), p. 164. DOI: `10.22323/1.444.0164`.

[29] Sergio B. Ricciarini et al. "Enabling low-power MAPS-based space trackers: a sparsified readout based on smart clock gating for the High Energy Particle Detector HEPD-02". In: *PoS* ICRC2021 (2021), p. 071. DOI: `10.22323/1.395.0071`.

[30] Roberto Iuppa et al. "The innovative particle tracker for the HEPD space experiment onboard the CSES-02 satellite". In: *PoS* ICRC2021 (2021), p. 070. DOI: `10.22323/1.395.0070`.

[31] *General Purpose Plastic Scintillator EJ-200, EJ-204, EJ-208, EJ-212*. Eljen Technology.

[32] *Metal package Photomultiplier Tube R9880U Series*. Hamamatsu. Mar. 2019.

[33] *Photomultiplier Tubes Basics and Applications*. Rev. 4. Hamamatsu. Apr. 2017.

[34] *ProASIC3E Flash Family FPGAs with Optional Soft ARM Support*. Rev. 15. Microsemi. June 2015.

[35] https://www.weeroc.com/products/sipm-read-out/citiroc-1a. 2021.

[36] *3 MSPS 1-/12-Bit ADCs in 8-Lead TSOT AD7273/AD7274*. Rev. 0. Analog Devices. Sept. 2005.

[37] *2.7 V to 5.5 V, 250 uA, Rail-to-Rail Output 16-Bit nanoDACTM in a SOT-23*. Rev. A. Analog Devices. Dec. 2010.

[38] B. P. Abbott et al. “Gravitational Waves and Gamma-Rays from a Binary Neutron Star Merger: GW170817 and GRB 170817A”. In: *The Astrophysical Journal Letters* 848.2 (Oct. 2017), p. L13. ISSN: 2041-8213. DOI: `10.3847/2041-8213/aa920c`. URL: `http://dx.doi.org/10.3847/2041-8213/aa920c`.

[39] Alessandro Lega et al. “Exploring the Efficiency of HEPD-02 LYSO:Ce Scintillators in the CSES-02 Satellite Mission for Detecting Gamma-Ray Bursts”. In: *PoS* ICRC2023 (2023), p. 758. DOI: `10.22323/1.444.0758`.

[40] *Keysight N6705 DC Power Analyzer User’s Guide*. Rev. 11. Keysight. Jan. 2015.

[41] *Programming Manual - Arbitrary Waveform Generator - Function Generator Operating Mode - High Definition AWG T3AWG3K Series*. Rev. 1.4. Teledyne LeCroy.

[42] https://www.caen.it/. 2023.

[43] *Supervisory Circuits with Watchdog and Manual Reset in 5-Lead SOT-23*. Rev. C. Analog Devices.

[44] *Keysight Infiniium 9000 Series Oscilloscopes User’s Guide*. Rev. 7. Keysight. Aug. 2019.

[45] *Keysight Infiniium 9000 Series Oscilloscopes Programmer’s Guide*. Rev. 6.40.00904. Keysight. June 2019.

[46] S.S. Kapoor and V.S. Ramamurthy. *Nuclear Radiation Detectors*. B M Udgaonkar. New Age International Publishers, 1986. ISBN: 9780852264966. URL: `https://books.google.it/books?id=RX5Xdo030X0C`.

[47] Xu Hong et al. “Peak tailing cancellation techniques for digital CR-(RC)n filter”. In: *Applied Radiation and Isotopes* 167 (2021), p. 109471. ISSN: 0969-8043. DOI: `https://doi.org/10.1016/j.apradiso.2020.109471`. URL: `https://www.sciencedirect.com/science/article/pii/S096980432030614X`.

[48] Francesco Maria Follega. “The performance of the High Energy Particle Detector HEPD-02 on board CSES-02 satellite: from simulation to test beam data.” In: *PoS* ICRC2023 (2023), p. 116. DOI: `10.22323/1.444.0116`.

[49] Claus Grupen and Boris Shwartz. *Particle Detectors*. 2nd ed. Cambridge Monographs on Particle Physics, Nuclear Physics and Cosmology. Cambridge University Press, 2008.

List of Figures

List of Tables